



TECHNISCHE  
UNIVERSITÄT  
WIEN  
Vienna University of Technology

Dissertation

---

# Non-Equilibrium Computer Experiments of Soft Matter Systems

---

Ausgeführt zum Zwecke der Erlangung des akademischen Grades eines Doktors der  
Naturwissenschaften unter der Leitung von

Univ. Prof. Dr. Gerhard Kahl  
Institut für Theoretische Physik (E136)  
Technische Universität Wien

und

Univ. Prof. Dr. Christos N. Likos  
Fakultät für Physik  
Universität Wien

eingereicht an der Technischen Universität Wien  
Fakultät für Physik

von

Arash Nikoubashman, M. Sc.  
Matrikelnummer 1028184  
Ahornergasse 9/13, 1070 Wien

Wien, im Juni 2012

---

(Arash Nikoubashman)



## Kurzfassung

Die Weiche Materie hat sich in den letzten Jahrzehnten zu einem überaus aktiven Forschungsfeld entwickelt, das durch einen hohen Grad an Interdisziplinarität gekennzeichnet ist: Physiker, Chemiker, Werkstoffkundler, Biologen und Mediziner arbeiten auf diesem Gebiet eng zusammen. Im Gegensatz zu Systemen der harten kondensierten Materie, deren physikalische Eigenschaften ausschließlich durch die Elektronenstruktur der atomaren Bestandteile gegeben sind, werden die Eigenschaften der Weichen Materie von einer Vielzahl von Faktoren beeinflusst, die durch sehr unterschiedliche Längen- und Zeitskalen charakterisiert sind: Dazu zählen etwa das mikroskopische Lösungsmittel (mit seinen physikalisch/chemischen Eigenschaften) oder die darin gelösten mesoskopischen Teilchen, deren innere Struktur im Rahmen geeigneter Syntheseprozesse gezielt beeinflusst werden kann. Während die Gleichgewichtseigenschaften vieler Systeme der weichen Materie mittlerweile sehr intensiv und ausführlich erforscht worden sind, so ist nur sehr wenig über ihr Verhalten außerhalb des Gleichgewichts bekannt. Ziel dieser Arbeit ist es, mit Hilfe von Computersimulationen die Nichtgleichgewichtseigenschaften einiger dieser komplexer Systeme – teilweise unter dem Einfluss äußerer Begrenzungen – zu untersuchen und somit zu einem tieferen Verständnis dieser Eigenschaften beizutragen. Die im Rahmen dieser Arbeit behandelten Problemstellungen reichen von stark verdünnten Systemen mit rigiden und flexiblen Tracer-Partikeln unter Einschluss in Kavitäten bis hin zu dichten Cluster-Kristallen unter dem Einfluss des strömenden Lösungsmittels. Im Rahmen unserer Arbeiten haben wir eine Vielzahl neuartiger und überraschender Eigenschaften entdeckt, wie zum Beispiel stark verlangsamte Diffusionsprozesse und Scherverzähung, und erwarten ein weites Spektrum an interessanten, technologisch relevanten Anwendungsmöglichkeiten für diese komplexen Materialien.



## **Abstract**

During the last decades, soft matter science developed into a highly active research field, attracting the interest of a vast number of different disciplines, such as chemistry, material science, biology and medicine. In striking contrast to hard matter systems, whose properties are essentially fixed by the electronic structure of the atoms, the situation in soft matter systems, also known as “complex fluids”, is distinctly more involved, since many different length and time scales are relevant. While the equilibrium properties of many soft materials have been studied in depth by now, only little is known about their behavior out of equilibrium. Therefore we have conducted extensive computer simulations to study the transport and flow properties of selected soft matter systems, in an effort to understand the non-equilibrium characteristics of these complex systems in a more profound way. The investigated problems range from dilute systems containing rigid and flexible tracer particles under confinement to dense cluster crystals under flow. We have discovered a variety of novel properties such as highly slowed-down, confinement-induced diffusion processes and shear thickening, and we anticipate a wide spectrum of future applications for these complex materials.



# Contents

<b>1. Introduction</b>	<b>3</b>
<b>2. Simulation Techniques</b>	<b>7</b>
2.1. Molecular Dynamics . . . . .	7
2.2. Brownian Dynamics . . . . .	8
2.3. Multi-Particle Collision Dynamics . . . . .	9
2.3.1. Simulation of Poiseuille Flow . . . . .	13
2.3.2. Simulation of Shear Flow . . . . .	15
2.3.3. Coupling between Solvent and Solute Particles . . . . .	16
<b>3. Investigated Systems</b>	<b>21</b>
3.1. Inverse Opals . . . . .	21
3.2. Linear and Branched Polymers . . . . .	24
3.3. Cluster Crystals . . . . .	29
<b>4. Diffusion and Translocation in Porous Materials</b>	<b>35</b>
4.1. Confined Diffusion in Periodic Porous Nanostructures . . . . .	36
4.2. Flow Induced Polymer Translocation through Narrow and Patterned Channels	43
4.2.1. Theory of Injection Thresholds . . . . .	43
4.2.2. Comparison between Theory and Simulation . . . . .	48
<b>5. Flow Properties of Cluster Crystals</b>	<b>57</b>
5.1. Cluster Crystals under Shear . . . . .	58
5.1.1. Shear-Induced String Formation . . . . .	58
5.1.2. Shear-Induced Crystallization . . . . .	65
5.2. Cluster Crystals under Poiseuille Flow . . . . .	68
5.2.1. Flow Profiles and Crystal Transport . . . . .	68
5.2.2. Flow Quantization . . . . .	72
<b>6. Conclusions</b>	<b>77</b>
<b>A. Parameters</b>	<b>83</b>
<b>B. Data Analysis</b>	<b>87</b>
B.1. Local Bond Order Parameters . . . . .	87
B.2. Cluster Analysis . . . . .	88
<b>C. Experimental Methods</b>	<b>91</b>
C.1. Tracer Particles . . . . .	91
C.2. Preparation of the Inverse Opals . . . . .	91
C.3. Fluorescence Correlation Spectroscopy . . . . .	92
<b>Bibliography</b>	<b>97</b>





# 1. Introduction

Soft matter physics has gained considerable interest in the past twenty years, and it is among the fastest expanding branches of the physical sciences. Soft matter systems, also often referred to as *colloidal dispersions* or *complex fluids*, are composed of *mesoscopic* particles, *i.e.* particles with typical sizes between 1 nm and 1  $\mu\text{m}$ , dispersed into a microscopic solvent. These colloidal particles, in turn, are usually complex aggregates built up from a large number of atoms or molecules, and can be of various shapes and nature: *rigid* spherical particles made of silica or polystyrene, platelets and ellipsoids classify as colloids, as well as *flexible* fractal objects such as linear and dendritic polymers.

The concentrated interest this field receives in physics, but also in chemistry and biology, is mainly due to two reasons: first of all, many substances belong to this class of materials whose common characteristic is, as the nomenclature suggests, that their rigidity against mechanical deformation is dramatically smaller than of atomic materials. Everyday examples range from naturally occurring systems, such as protein solutions, DNA molecules or blood, over comestibles, like milk, mayonnaise or ice cream, to all kind of industrial products, *e.g.* paint, pharmaceuticals or liquid crystals [1, 2]. Therefore, soft matter plays a key role in many technological applications and processes. Second, soft matter systems are of utmost importance in academic research, as their special properties make them valuable model systems: by suitably changing relevant properties of the suspension, such as the solvent quality, salt concentration and temperature, or by varying the chemical and physical architecture of the dispersed particles, it is possible to tune the effective interactions in a well controlled way, leading to precisely tailored interaction potentials.

Another intriguing characteristic of soft matter systems is that the comparatively large size of the dispersed particles (compared to their atomic counterparts) facilitates experimental investigations considerably: in addition to conventional indirect measurement techniques, *e.g.* small-angle neutron scattering (SANS) or X-ray scattering [3], the particles' motions and behavior can also be observed in real-time *via* light or video microscopy [4, 5]. This is usually achieved by labeling the particles with an appropriate photosensitive dye [4, 6]. Furthermore, the advent of optical tweezers enabled experimentalists to easily trap, move and arrange single particles, and to measure the forces acting between colloids [7–9].

While the overwhelming part of the scientific effort carried out for colloidal systems so far has been dedicated to the *equilibrium* properties, much less is known about the behavior of these system in *non-equilibrium* scenarios. Therefore, the focus of this work lies on confined

and driven complex fluids, in order to contribute to a more profound understanding of the transport and flow properties of soft matter systems.

Colloidal dispersions and polymer solutions confront fundamental research with a formidable challenge due to the fact that they are *non-Newtonian* fluids. Consequently, they offer a wide spectrum of possibilities in rheological applications. Contrary to simple liquids, their viscosity depends on the applied external stresses, such as shear, pressure gradients or other external fields. A key role in their rheology is played by the presence of at least two components, the solvent and the suspended particles, with vastly disparate length- and time-scales. In the case of polymer solutions, entanglements between the chains are an additional feature with very important dynamical consequences. The flow properties of complex fluids become even more relevant in the modern fields of micro- and nanofluidics, where the narrow geometrical constrictions of the confining channels bring forward novel properties and highlight the effects of the coupling to the surrounding walls [10, 11]. Some of the most prominent and widely-discussed rheological properties of non-Newtonian liquids include shear-banding [12], thixotropy [13], shear-thinning [14, 15] as well as shear-thickening [14]. Such complex fluids are also relevant for a wide variety of applications in nanotechnology and micropatterning [16, 17], in microfluidics [18], shock absorption [19], and protective clothing [20]. In addition, they are also encountered in many biological systems, *e.g.* in cytoplasm and blood [21].

From the theoretical point of view, the large number of constituent entities poses one of the key problems, since it is infeasible to employ concepts based on classical statistical mechanics that take all the degrees of freedom explicitly into account. Instead, the complex colloidal particles have to be reduced to their most essential features by applying suitable coarse graining procedures [22–24], that average over the degrees of freedom at the atomic level. Recently, effective potentials have been derived for selected colloids, *e.g.* for neutral and charged star polymers [25–27], microgels [26, 27] and amphiphilic dendrimers [28, 29].

In this work, we employ extensive computer simulations to study the transport and flow properties of selected soft matter systems. We have chosen these systems motivated in particular with respect to their realizability in experiments and their relevance as model systems.

The rest of this work is organized as follows:

**Chapter 2** is dedicated to the various simulation techniques employed in this work. First, we give an introduction to the general concepts, and then we present the specific implementations necessary for the problems at hand.

**Chapter 3** introduces the investigated systems and the respective interparticle potentials. In this chapter we also discuss their relevance as model systems and their realizations in experiments.

---

**Chapter 4** presents the results concerning the diffusion and translocation in porous materials. We first study the diffusion of rigid tracer particles in a confined, periodic environment, and then extend our studies onto the flow induced translocation of polymers through narrow channels.

**Chapter 5** is dedicated to the flow behavior of cluster crystals. We first study the response to shear flow, and then go over to analyze the behavior under pressure driven flow.

**Chapter 6** contains a brief summary of the results and provides the conclusions drawn from this work. Furthermore, we present a short outlook on future work.



## 2. Simulation Techniques

Since it is in general impossible to determine the properties of complex molecular systems analytically, computer simulations are often the mean of choice to evaluate the physical properties. Such computational experiments are very similar to their real-life counterparts, since their cycle of work includes also preparation, equilibration and measurement steps. In fact, some of the most common mistakes that can be made when performing a computer experiment are very similar to the mistakes that can be made in real experiments, *e.g.* an inadequate preparation of a sample or an accidental manipulation of an observable.

The key quantity of a numerical simulation is the Hamiltonian function  $\mathcal{H}(\{\mathbf{r}_i\}, \{\mathbf{v}_i\})$ , which describes the total energy of the system:

$$\mathcal{H}(\{\mathbf{r}_i\}, \{\mathbf{v}_i\}) = \sum_{i=1}^N \frac{m\mathbf{v}_i^2}{2} + U(\{\mathbf{r}_i\}). \quad (2.1)$$

Here, the  $\{\mathbf{r}_i\}$  and the  $\{\mathbf{v}_i\}$  represent (in general) the positions and velocities of the  $N$  particles of our system. The first term in Eq. (2.1) is the kinetic energy, whilst the second term represents the potential energy of the system. For dilute and weakly interacting systems, many body effects are usually negligible, and it is therefore sufficient to express  $U$  by pairwise interaction potentials (see Chapter 3 for the system-specific details). In the vast majority of cases, the solvent molecules are not explicitly treated but are instead included as a continuous effective medium in the formulation. However, in this work, the cases of both implicit and explicit solvents have been studied, and the reader is referred to Section 2.3 for a more detailed description of the solvent dynamics.

### 2.1. Molecular Dynamics

*Molecular dynamics* simulations (MD) are a widely employed technique to compute the equilibrium and transport properties of classical many-body systems. This is an excellent approximation for a wide range of materials, since quantum effects can be neglected for heavier atoms and molecules. Thus in this context “classical” means that the motion of the constituent particles obeys the laws of *classical mechanics*. In what follows, we choose the *micro-canonical ensemble* for convenience. Hence, the total energy  $E$ , the volume  $V$  and the particle number  $N$  are strictly preserved. In molecular dynamics, the trajectory of each

individual particle can then be obtained by solving Newton's second law:

$$\frac{d^2 \mathbf{r}_i}{dt^2} = \frac{\mathbf{F}_i}{m} = -\frac{1}{m} \sum_{j \neq i}^N \nabla U(|\mathbf{r}_i - \mathbf{r}_j|), \quad (2.2)$$

where  $t$  denotes the time and  $\mathbf{F}_i$  the force acting on particle  $i$ . However, since computers cannot solve differential equations analytically *per se*, a suitable numerical algorithm has to be chosen from the wide repertoire of existing methods. In this work, we opted for the so-called *Velocity-Verlet* algorithm which, in contrast to the much simpler Euler method, offers greater numerical stability as well as time-reversibility and phase space preserving properties. The basic idea of this algorithm is to discretize the time  $t$  by first writing down the two first-order Taylor expansions for the positions  $\mathbf{r}_i(t)$  and velocities  $\mathbf{v}_i(t)$ , both each at time  $t + \Delta t/2$  and  $t + \Delta t$ . Then these expressions are merged, yielding the following equations:

$$\mathbf{r}_i(t + \Delta t) = \mathbf{r}_i(t) + \Delta t \mathbf{v}_i(t) + \frac{\Delta t^2}{2} \mathbf{a}_i(t) + \mathcal{O}(\Delta t^4), \quad (2.3)$$

$$\mathbf{v}_i(t + \Delta t/2) = \mathbf{v}_i(t) + \frac{\Delta t}{2} \mathbf{a}_i(t) + \mathcal{O}(\Delta t^4), \quad (2.4)$$

$$\mathbf{v}_i(t + \Delta t) = \mathbf{v}_i(t + \Delta t/2) + \frac{\Delta t}{2} \mathbf{a}_i(t) + \mathcal{O}(\Delta t^4), \quad (2.5)$$

where  $\mathbf{a}_i$  denotes the acceleration of the  $i$ -th particle. Observables are calculated in MD simulations *via* time averages. If the correctness of the ergodic theory is assumed, then the time averages obtained in a conventional molecular dynamics simulation are equivalent to ensemble averages. However, it is often more appropriate to perform simulations in other ensembles such as the *canonical ensemble*, since real life experiments are performed rather at constant temperature  $T$  than at constant energy.

## 2.2. Brownian Dynamics

The *Brownian dynamics* (BD) simulation technique describes inherently a system in the canonical ensemble and addresses the problem of timescale separation that arises when one species of particles in the system is much faster than another. This is for instance the case when the solvent is no longer treated as a continuous medium but rather as a bulk of discrete particles. This can be a serious problem in pure MD simulations, since the short time-steps needed to handle the fast motion of the solvent particles are not compatible with the very long runs needed to allow the evolution of the slower modes. Given that the fast motions are often not of any interest, an approximate approach may be adopted. Hence, the solvent particles are not taken into account explicitly in simulation, but instead their effects upon

the solute are represented by a combination of random forces and frictional terms. Newton's equations of motion are thus replaced by the so-called *Langevin equation*:

$$\frac{d\mathbf{r}_i}{dt} = \frac{1}{m\xi} \sum_{j \neq i}^N \mathbf{H}_{ij} [-\nabla U(|\mathbf{r}_i - \mathbf{r}_j|) - m\mathbf{a}_i(t) + \mathbf{w}_i(t)], \quad (2.6)$$

with the frictional coefficient  $\xi$ . In this equation,  $\mathbf{H}_{ij}$  is the so-called hydrodynamic interaction tensor between solute particles  $i$  and  $j$ , and is set equal to the identity matrix ( $\mathbf{H}_{ij} = \mathbf{I}$ ) when hydrodynamic interactions are ignored [30]. Moreover, the total force acting on each colloid is supplemented by a Gaussian noise field  $\mathbf{w}_i(t)$  that mimics the random collisions with the solvent molecules. The statistical properties of the noise are given through its average  $\langle \mathbf{w}_i(t) \rangle = 0$  and variance  $\langle \mathbf{w}_i(t) \mathbf{w}_j(t') \rangle = 2k_B T \mathbf{H}_{ij}^{-1} \delta(t - t')$ .

A straightforward method of conducting such Brownian dynamics simulations based on Eq. (2.6) has been proposed by Ermak *et al.* [31–33], where the equations of motion are integrated over a time interval  $\Delta t$  under the assumption that the stochastic forces  $\mathbf{w}_i(t)$  remain approximately constant:

$$\mathbf{r}_i(t + \Delta t) = \mathbf{r}_i(t) + c_1 \Delta t \mathbf{v}_i(t) + c_2 \Delta t^2 \mathbf{a}_i(t) + \mathbf{r}_G, \quad (2.7)$$

$$\mathbf{v}_i(t + \Delta t) = c_0 \mathbf{v}_i(t) + c_1 \Delta t \mathbf{a}_i(t) + \mathbf{v}_G. \quad (2.8)$$

The coefficients read  $c_0 = e^{-\xi \Delta t}$ ,  $c_1 = (1 - c_0)/(\xi \Delta t)$  and  $c_2 = (1 - c_1)/(\xi \Delta t)$  while  $\mathbf{r}_G$  and  $\mathbf{v}_G$  denote random variables drawn from a bivariate Gaussian distribution with zero mean values and variances given by:

$$\sigma_r^2 = \Delta t \frac{k_B T}{m\xi} \left( 2 - \frac{3 - 4e^{-\xi \Delta t} + e^{-2\xi \Delta t}}{\xi \Delta t} \right), \quad (2.9)$$

$$\sigma_v^2 = \frac{k_B T}{m} (1 - e^{-2\xi \Delta t}). \quad (2.10)$$

It is worthwhile noting that for smaller values of the friction coefficient  $\xi \rightarrow 0$  the dynamical aspects dominate and Newtonian mechanics is recovered since Eqs. (2.7) and (2.8) then turn into a simple Taylor series.

## 2.3. Multi-Particle Collision Dynamics

The theoretical analysis of hydrodynamic interactions (HI) can be of outstanding importance and an interesting task, as these interactions build the foundation of many physical phenomena. Yet their study is also highly challenging, due to the large length- and time-

scale separation between the solvent and the embedded solute particles. In such mesoscopic systems, hydrodynamic interactions often play a substantial role, *e.g.* for the conformational dynamics of biopolymers [34], the rheological properties of colloidal suspensions [35–37] or polymers in solution [38–44]. However, a simple continuum description based on the Navier-Stokes equation is not sufficient in many situations, since molecular-level details, like thermal fluctuations, play a central role in determining the dynamic behavior. On the other hand, atomistic MD simulations retain too many (unnecessary) microscopic degrees of freedom, consequently requiring very small time steps in order to resolve the high frequency modes.

Thus, the difficult task is to find a mesoscopic model that balances the aforementioned shortcomings by incorporating the essential dynamical properties, and yet being simple enough to be simulated over long time ranges and on long distance scales. Considerable effort has been devoted to the development of such mesoscale simulation methods, and *Dissipative Particle Dynamics* (DPD) [45–47], *Lattice-Boltzmann* (LB) [48–50], and *Multi-Particle Collision Dynamics* (MPCD) [51, 52] became the most prominent techniques. Essentially, all these approaches are alternative ways of solving the Navier-Stokes equation and its generalizations.

In this work, we have opted to employ a hybrid simulation approach, in which standard molecular dynamics simulations for the solute are combined with the MPCD technique for the solvent. One important feature of the MPCD algorithm is that the dynamics is well-defined at any arbitrary time step. In contrast to pure MD or DPD simulations, which approximate the continuous-time dynamics of a system, the time step does not have to be small. Another crucial advantage of this approach is, that macroscopic transport properties can easily be extracted in an analytic way, and that the simulation technique is meanwhile well-documented (for an extensive overview, see for instance Ref. [53]).

MPCD is a mesoscopic, particle-based simulation method, consisting of alternating *streaming* and *collision* steps, where the  $N_s$  solvent particles are assumed to be non-interacting. Instead, the coupling between the solvent and solute particles is realized through momentum exchange. During the streaming step, the solvent particles of unit mass  $m'$  propagate ballistically over a period of  $\Delta t$ :

$$\mathbf{r}'_i(t + \Delta t) = \mathbf{r}'_i(t) + \Delta t \mathbf{v}'_i(t), \quad (2.11)$$

where  $\mathbf{r}'_i(t)$  is the position and  $\mathbf{v}'_i(t)$  the velocity of the  $i$ -th solvent particle at time  $t$ . In the collision step, the solvent particles are first grouped into collision cells and then undergo stochastic collisions with particles within the same cell:

$$\mathbf{v}'_i(t + \Delta t) = \mathbf{u}_j(t) + \mathbf{\Omega}(\alpha)[\mathbf{v}'_i(t) - \mathbf{u}_j(t)]. \quad (2.12)$$



Here,  $\mathbf{u}_j$  denotes the center of mass velocity of the  $j$ -th collision cell, and  $\mathbf{\Omega}$  is a norm-conserving rotation matrix around a fixed angle  $\alpha$ , which reads:

$$\Omega(\alpha) = \begin{bmatrix} \cos \alpha + \zeta_x^2(1 - \cos \alpha) & \zeta_x \zeta_y(1 - \cos \alpha) - \zeta_z \sin \alpha & \zeta_x \zeta_z(1 - \cos \alpha) + \zeta_y \sin \alpha \\ \zeta_y \zeta_x(1 - \cos \alpha) + \zeta_z \sin \alpha & \cos \alpha + \zeta_y^2(1 - \cos \alpha) & \zeta_y \zeta_z(1 - \cos \alpha) - \zeta_x \sin \alpha \\ \zeta_z \zeta_x(1 - \cos \alpha) - \zeta_y \sin \alpha & \zeta_z \zeta_y(1 - \cos \alpha) + \zeta_x \sin \alpha & \cos \alpha + \zeta_z^2(1 - \cos \alpha) \end{bmatrix}, \quad (2.13)$$

with  $\zeta_x$ ,  $\zeta_y$  and  $\zeta_z$  being the components of the unit vector  $\hat{\zeta}$  along the rotation axis. Ihle *et al.* have demonstrated in Ref. [54] that it is advisable to choose the direction of the rotation axis randomly. In our implementation, we determine the components of  $\hat{\zeta}$  by picking random numbers from a uniform distribution on a spherical surface  $\mathbb{S}^2$  *via* [55]:

$$\begin{aligned} \zeta_x &= 2x_1 \sqrt{1 - x_1^2 - x_2^2}, \\ \zeta_y &= 2x_2 \sqrt{1 - x_1^2 - x_2^2}, \\ \zeta_z &= 1 - 2(x_1^2 + x_2^2), \end{aligned} \quad (2.14)$$

with  $x_1, x_2 \in [-1, 1]$  and  $x_1^2 + x_2^2 < 1$ . The size of the MPCD collision cells,  $a$ , determines the spatial resolution of the HI, and must be set appropriately for each problem. The mean free path of a solvent particle is then given by  $\lambda \sim \Delta t \sqrt{T}$ , and it has been shown in Ref. [56] that Galilean invariance is violated for  $\lambda < a/2$ . Therefore, all lattice cells are shifted by a randomly chosen vector, drawn from a cube with an edge length in the interval  $[-a/2, +a/2]$  before each collision step.

The flow properties of liquids are essentially determined by their transport coefficients. Among these are, for example, the dynamic viscosity  $\eta$  and the diffusion coefficient  $D$ . Furthermore, in many situations we are concerned with the ratio of the inertial force to the viscous force, the former characterized by the fluid density  $\rho_s$ . This ratio is characterized by the kinematic viscosity  $\nu = \eta/\rho_s$ . In MPCD, the relation between these *macroscopic* rheological properties and the *microscopic* evolution described by Eqs. (2.11) and (2.12) is well-defined, and can be expressed in an analytic fashion.

The total dynamic viscosity  $\eta$  of the pure liquid is the sum of two contributions, namely the kinetic viscosity  $\eta_{\text{kin}}$  and the collisional viscosity  $\eta_{\text{col}}$ . The kinetic transport has its origin in the movement of the particles, as they always carry a certain fraction of momentum and energy with themselves. For this reason  $\eta_{\text{kin}}$  is the dominant part in  $\eta$  for small rotational angles  $\alpha$  and long mean free paths  $\lambda$ . On the other hand, the particles can also exchange momentum and energy during the collision steps, and hence  $\eta_{\text{col}}$  plays an important role for large  $\alpha$  and small  $\lambda$ . For the dynamics of liquids, the latter contribution bears particular relevance, whereas for gaseous media the kinetic transport is the dominant factor. Analytic

expressions have been derived for these two contributions by means of a gas kinetic approach in Ref. [51] and they read:

$$\eta_{\text{kin}} = \frac{k_{\text{B}}T\Delta t\rho_s}{a^3} \left( \frac{5\rho_s}{(4 - 2\cos\alpha - 2\cos(2\alpha))(\rho_s - 1)} - \frac{1}{2} \right), \quad (2.15)$$

$$\eta_{\text{col}} = \frac{(1 - \cos\alpha)}{18a\Delta t}(\rho_s - 1), \quad (2.16)$$

where  $\rho_s$  denotes the number density of the solvent particles. In order to verify these identities, simulations under Poiseuille flow have been carried out and  $\eta$  has been calculated from the resulting velocity-field profile (the reader is referred to Section 2.3.1 for a more detailed discussion). In Figure 2.1, both the theoretical values and the corresponding simulation results for  $\eta$  are depicted and very good agreement between them can be seen. Here, the blue curve corresponds to Eq. (2.15), while the red curve represents Eq. (2.16); it immediately stands out that the ratio between the kinetic and the collisional contribution depends considerably on the model parameters  $\alpha$  and  $\lambda$ .

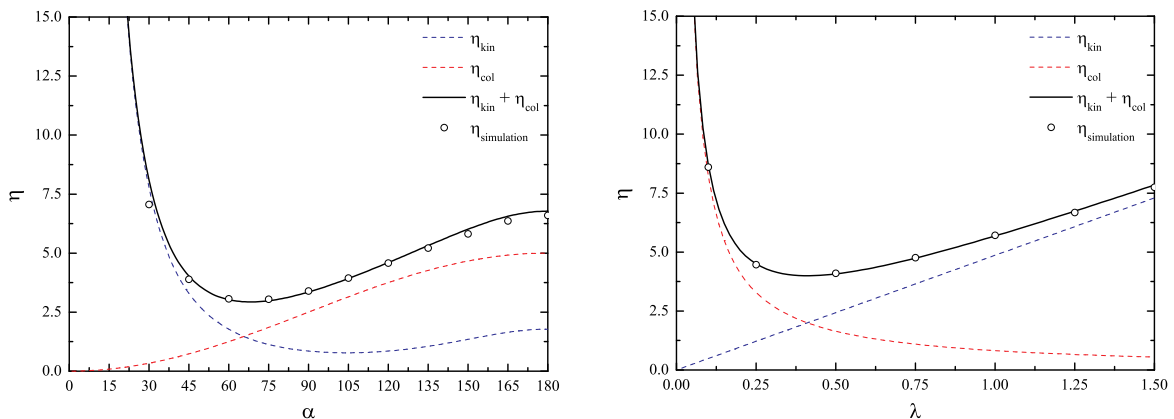


Figure 2.1.: Contributions to the dynamic viscosity  $\eta$  for a MPCD-liquid. Left panel:  $\alpha$  dependence of  $\eta$  at  $\lambda = 0.2$  and  $\rho_s = 5$ . Right panel:  $\lambda$  dependence of  $\eta$  at  $\alpha = 130$  and  $\rho_s = 10$ .

Whereas the above-described rules governing the solvent dynamics are general, the simulation of specific flow profiles requires special care and will be discussed in the ensuing subsections. For such driven flows, one important measure is the so-called *Reynolds number*,  $\text{Re}$ , which is a measure of the ratio of the inertial forces to the viscous forces. In general,  $\text{Re}$  can be written down as:

$$\text{Re} = \frac{vL}{\nu} \quad (2.17)$$

where  $v$  and  $L$  are characteristic velocities and length scales of the system, that depend on the precise problem. The Reynolds number is also often used to characterize different

flow regimes, such as laminar flow, where viscous forces are dominant and the solvent layers smoothly propagate well separated from each other, or turbulent flow, which is dominated by inertial forces resulting in chaotic eddies, vortices and other flow instabilities.

### 2.3.1. Simulation of Poiseuille Flow

Poiseuille flow, enclosed by two parallel plates positioned at  $x = 0$  and  $x = L_x$ , is driven by a pressure gradient parallel to the flow direction, and is slowed down by viscous drag along both plates, so that these forces are in balance. Under such conditions, a parabolic velocity profile builds up:

$$v_z^{(0)}(x) = \frac{\rho_s g}{2\eta}(L_x - x)x, \quad (2.18)$$

where the superscript denotes the velocity profile of the *pure* solvent, as opposed to the one when solute particles are present. The strength of the gravitational field can be varied by tuning  $g$ . The parabolic velocity profile vanishes at  $x = 0$  and at  $x = L_x$ , and attains its maximum value,  $v_0$ , at the middle of the channel ( $x = L_x/2$ ), *viz.*:

$$v_0 = \frac{\rho_s g L_x^2}{8\eta}. \quad (2.19)$$

Figure 2.2 shows a schematic representation of such a setup, and several methods exist for creating such a flow, for instance forced, gravitational, and surface-induced approaches. The

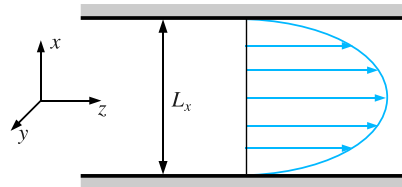


Figure 2.2.: Schematic representation of the simulation setup for Poiseuille flow, indicating the flow ( $z$ ) and gradient ( $x$ ) directions.

forced flow has been considered in Refs. [51], [52], and [57], where the pressure gradient is mimicked by hanging a virtual pump to the inlet of the channel. However, it has been shown in Ref. [58] that this approach has several drawbacks: first of all, a considerable deformation of the velocity-field and density profiles can occur at the inlet and outlet of the channel. In addition, a gradual density drop of particles along the channel length can be noticed. Hence these perturbations lead to a severe reduction of usable space in the simulation box.

The use of gravitationally driven flow, which is adopted in this contribution, does not distort the velocity-field and density profiles, and therefore no artificial tricks are needed to suppress the above mentioned inhomogeneities. The external force acting on the unit volume of the fluid is given by  $\mathcal{F} = \varrho_s g \hat{\mathbf{z}}$ , where  $g$  is the acceleration constant, controlling the magnitude of the pressure drop. The effect of  $\mathcal{F}$  can easily be incorporated into the streaming step as follows:

$$\mathbf{r}'_i(t + \Delta t) = \mathbf{r}'_i(t) + \Delta t \mathbf{v}'_i(t) + \frac{\Delta t^2}{2} g \hat{\mathbf{z}}, \quad (2.20)$$

$$\mathbf{v}'_i(t + \Delta t) = \mathbf{v}'_i(t) + \Delta t g \hat{\mathbf{z}}, \quad (2.21)$$

and a steady Poiseuille flow builds up self-consistently after a short time when no-slip boundary conditions are applied at the surface layers. For planar walls coinciding with the boundaries, such conditions are conveniently simulated by employing a bounce-back rule, *i.e.*, the velocities of particles that hit the walls are inverted after the collision. However, for a more general setup the walls will not coincide with, or even be parallel to the cell boundaries. Furthermore, partially occupied cells can also emerge from the cell-shifting, which is unavoidable for small mean free paths  $\lambda$ . In Ref. [57] it has been demonstrated that the bounce-back rule has to be modified in such a case. Indeed, it is well visible from Figure 2.3 that the velocity profile does not extrapolate to zero at the walls under conventional bounce-back conditions.

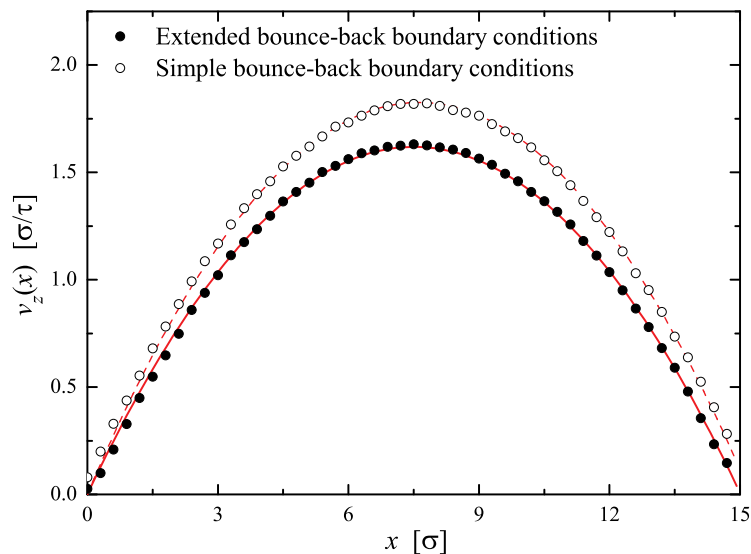


Figure 2.3.: Velocity-field profile in  $z$ -direction along the  $x$ -axis for a channel of volume  $V = 15 \times 15 \times 25$  and solvent density  $\rho_s = 5$ . The open circles represent the results for simple bounce-back boundary conditions, while the full circles show the modified boundary conditions, see the text and Eq. (2.22).

One possible solution is to refill all those cells that are cut by the walls and therefore obtain a number of particles  $n_j$  smaller than the average number  $n_{\text{avg}}$  of the bulk cells. The velocities of these virtual particles are then drawn from a Maxwell-Boltzmann distribution of zero average velocity and the same temperature  $T$  as the fluid. But since the sum of random vectors drawn from a Gaussian distribution is again Gaussian-distributed, the individual velocities never have to be determined explicitly. Instead, the average velocity  $\mathbf{u}_j$  appearing in Eq. (2.12) can be modified as follows:

$$\mathbf{u}_j = \frac{\sum_i \mathbf{v}'_i + \mathbf{v}_G}{n_{\text{avg}}}, \quad (2.22)$$

where the components of  $\mathbf{v}_G$  are normally-distributed with variance  $(n_{\text{avg}} - n_j)k_B T$  and zero average. This additional term successfully addresses the spurious wall-slip, as can be seen by the very good agreement between the theoretical predictions and the simulation results shown in Figure 2.3. Moreover, we can now utilize the corrected velocity profile to determine the dynamic viscosity  $\eta$ :

$$\eta = \frac{\rho_s g L_x^2}{8\nu_0}. \quad (2.23)$$

Finally it should be noted that the computation of  $\eta$  in these non-equilibrium conditions is much more precise than by means of the Green-Kubo relation in equilibrium [59], since time correlation functions represent the average response to the naturally occurring (and hence fairly small) fluctuations in the system properties. The signal-to-noise ratio is particularly unfavorable at long times, where there may be a significant contribution to the integral defining a transport coefficient. Moreover, the finite system size imposes a limit on the maximum time for which reliable correlations can be calculated. The idea behind non-equilibrium methods is that a much larger fluctuation may be induced artificially, and the signal-to-noise level of the measured response are improved dramatically. Thus, by measuring the steady state response to such a perturbation, problems with the long-time behavior of correlation functions are avoided.

### 2.3.2. Simulation of Shear Flow

In fluid dynamics, shear flow refers to the laminar flow of a viscous fluid in the space between two parallel plates, which are moving relative to each other with a constant velocity (see Figure 2.4). The flow is driven by virtue of viscous drag force acting on the fluid and the applied pressure gradient parallel to the plates. This type of fluid flow is also referred to as *Couette flow*. In experiments, Couette flow is usually realized inside a small gap between two counter rotating concentric cylinders. However, such co-axial cylinder devices have both

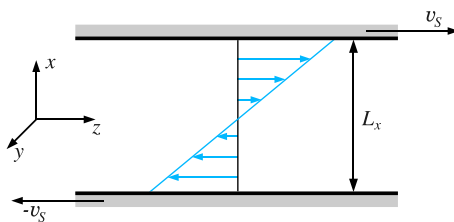


Figure 2.4.: Schematic representation of the simulation setup for shear flow, indicating the flow ( $z$ ), gradient ( $x$ ) and vorticity ( $y$ ) direction.

curvature and finite geometry, where the latter gives rise to an increased drag in the wall region. Thus, the execution of such experiments is generally nontrivial.

In our simulations, shear flow with shear-rate  $\dot{\gamma} = 2v_S/L_x$  was incorporated into the system by rescaling the center of mass velocities of the collision cells close by the shear plane to  $\pm v_S$  [35]. The force needed to accelerate these boundary particles to the desired velocity  $v_S$  is called the mean shear force  $\mathbf{F}_S$ , and it can be determined by summing over all necessary momentum transfers:

$$\mathbf{F}_S = \frac{1}{\Delta t} \left\langle \sum_{i=1}^{N_s} m'_i \Delta \mathbf{v}'_i + \sum_{i=1}^N m_i \Delta \mathbf{v}_i \right\rangle. \quad (2.24)$$

From this quantity we can then compute the shear stress  $\sigma_{xz}$  of the system, *i.e.* the component of the stress coplanar with the system cross section, as  $\sigma_{xz} = \hat{\mathbf{z}} \cdot \mathbf{F}_S / (L_x L_y)$ .

We have favored this approach over other methods, such as the Lees-Edwards boundary conditions [60], because the employed boundary conditions resemble more the actual experiment and lead to a spontaneous development of the desired linear velocity profile. Since in our approach the velocity profile is *not* externally imposed, but completely self-emerging, we can also observe phenomena such as wall-slip, nonlinear velocity-, or density-profiles. In addition, shearing only the fluid and not the colloidal dispersion as a whole works as well for dilute dispersions [42, 44], but for dense systems, this approach is not suitable since the resulting viscosity is much too small [36]. In fact, what one measures in this case is the flow of the fluid streaming around the solute particles like a flow through a porous medium.

### 2.3.3. Coupling between Solvent and Solute Particles

In MPCD simulations, many different approaches exist for coupling a suspended solute particle to the surrounding solvent, and for an extensive overview we refer the reader to Refs. [41] and [53]. A commonly used method is to sort the solute particles into the collision cells, and include their velocities in the rotation step [38]. Although this approach seems oversimplified

at first glance, it has been shown in Ref. [39], that the dynamics of polymer chains are correctly reproduced. This technique has been employed for the simulation of, amongst others, star polymers [42], dendrimers [44], and cluster crystals [61]. However, the disadvantage of this method is that only the fluid particles within the same cell are taken into account for the coupling. This in turn implies, that in order to affect the same area of the flow field like in reality, one has to choose the cells to be of the same size as the colloidal particles. Thus the flow field around the colloidal particle cannot be resolved in detail, and neither the fact that colloidal particles push away the solvent nor depletion and lubrication forces can be reproduced at any level. A second possibility is to couple the solvent and solute particles through repulsive central forces [52]. However, such a force has to be rather strong to prohibit the solvent particles of penetrating the colloids. Therefore, when implementing this procedure, a small time step  $\Delta t$  is required in order to resolve these interactions correctly, and a large number of MD time steps are needed during the streaming step. Another drawback of this approach is that only slip boundary conditions can be modeled with central forces. This deficiency can be easily understood on the basis of the following example: first, assume a buoyant colloidal particle that is surrounded by resting solvent particles, and then spin the colloid without moving it from its original position. If the solvent particles are now coupled to the colloid only by a central force, they will not react to this rotation, since the mutual distances remain unchanged. In reality however, the surface of a colloid is never perfectly smooth, and therefore the solvent close to the colloid will be dragged along. The detailed molecular origins of these boundary conditions are subtle problems, and for a recent review of the extensive literature on this subject see Ref. [62].

In this work, we have coupled the colloids to the solvent particles through the exchange of both *linear* and *angular* momentum during the streaming step, following the procedure put forward by Inoue *et al.* [63]. First we check after each streaming step whether the new position of the  $i$ -th solvent particle lies within a colloidal particle. If this is the case, we stochastically deflect the solvent particle from the colloid and transfer the momentum. In what follows, we will discuss this procedure in more detail.

Figure 2.5(a) depicts the collision process between a point-like solvent particle and an impenetrable colloid, located at  $\mathbf{r}_j$ . At start time  $t$ , the solvent particle is located at  $\mathbf{r}'_i(t)$  and propagates ballistically over a period of  $\Delta t$ . Along its trajectory, it crosses the surface of the colloid at the point  $\tilde{\mathbf{r}}'_i$ . In order to calculate the exact time and position of the collision, we first write down the equation of a sphere, centered at  $\mathbf{r}_j$ :

$$|\mathbf{r} - \mathbf{r}_j|^2 = \frac{\sigma^2}{4}, \quad (2.25)$$

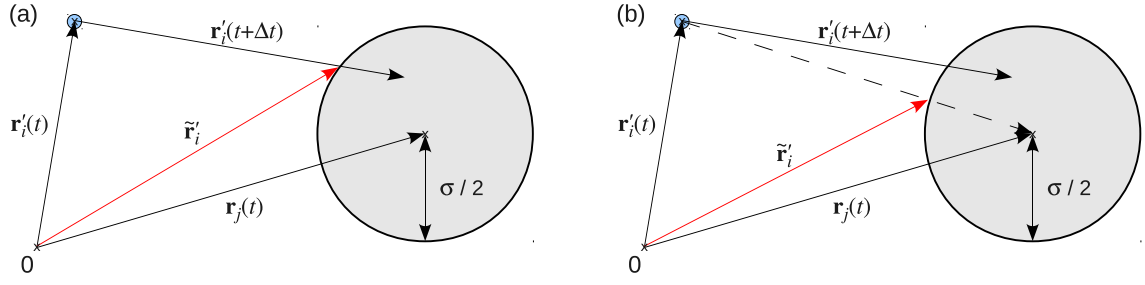


Figure 2.5.: Schematic representation of the collision process between a solvent particle with index  $i$  and an impenetrable colloid  $j$  with diameter  $\sigma$ . The vector  $\mathbf{r}'_i(t)$  denotes the position of the solvent particle at time  $t$ , while  $\mathbf{r}_j(t)$  denotes the position of the colloid. The vector  $\tilde{\mathbf{r}}'_i$  (red arrow) shows the point of impact in the case of the (a) exact and (b) approximate calculation (see text).

and then of a linear trajectory in space, starting at  $\mathbf{r}'_i$ :

$$\mathbf{r} = \mathbf{r}'_i + \Delta t \hat{\mathbf{v}}'_i, \quad (2.26)$$

where  $\sigma$  is the diameter of the colloid and  $\hat{\mathbf{v}}'_i$  denotes the normalized velocity of the solvent particle. Merging equations (2.25) and (2.26) yields:

$$\Delta \tilde{t}_{1,2} = -(\mathbf{r}'_i \cdot \hat{\mathbf{v}}'_i - \mathbf{r}'_i \cdot \mathbf{r}_j - \hat{\mathbf{v}}'_i \cdot \mathbf{r}_j) \pm \sqrt{(\mathbf{r}'_i \cdot \hat{\mathbf{v}}'_i - \mathbf{r}'_i \cdot \mathbf{r}_j - \hat{\mathbf{v}}'_i \cdot \mathbf{r}_j)^2 - \mathbf{r}'_i{}^2 - \mathbf{r}_j{}^2 + \sigma^2/4}. \quad (2.27)$$

If we now take the smaller value of the  $\Delta \tilde{t}$ 's and insert it back into Eq. (2.26), we get the exact point of impact  $\tilde{\mathbf{r}}'_i = \mathbf{r}'_i + \Delta \tilde{t} \hat{\mathbf{v}}'_i$ . However, this procedure is computationally quite expensive, and it has been shown in Refs. [35, 40] that such a detailed description is not necessary. Instead, it is sufficient to place the solvent particle on the line to the colloidal center and move it with its new velocity half of a time step. This approximation is schematically shown in Figure 2.5(b), and  $\tilde{\mathbf{r}}'_i$  is then simply given by:

$$\tilde{\mathbf{r}}'_i = \mathbf{r}_j + \frac{\sigma}{2} \frac{\mathbf{r}'_i - \mathbf{r}_j}{|\mathbf{r}'_i - \mathbf{r}_j|} = \mathbf{r}_j + \frac{\sigma}{2} \hat{\mathbf{e}}_n, \quad (2.28)$$

Next, the momentum between the two particles has to be exchanged. This can be achieved by applying the extended bounce-back collision rule (see preceding subsection). However, Padding *et al.* have shown that these boundary conditions result in rotational frictions that turned out to be too large [40]. This discrepancy might stem from the fact, that the colloidal particles can move, and therefore have a local temperature, in contrast to the immobile walls considered in Ref. [57].



Alternatively, the solvent particles can be scattered from the colloidal target in a stochastic way, where upon collision, the particles are assigned random normal and tangential velocities  $v_{i,n}^*$  and  $v_{i,t}^*$  respectively (relative to the velocity of the colloid) [35, 40, 63]. These velocities have to be chosen in the following way: since there are no solvent particles within the colloidal particle, and the velocity distribution next to a colloidal particle should be independent of any neighboring particles, the velocity distribution for the deflected solvent particle has to be the same as if the space inside the suspended particle was filled with the solvent. Then, one could evaluate the velocity distribution of the scattered solvent particles by taking the distribution of the imaginary solvent particles passing through the colloid surface. Unfortunately it is a nontrivial task to determine this distribution analytically for a curved surface. However, if the mean free path of the solvent particles is small compared to the diameter of the suspended colloids, then we can safely assume the colloid surface to be an infinitely extended plane. Within this approximation, the probability distributions for the new velocities read:

$$p(v_{i,n}^*) = m' \beta v_{i,n}^* \exp(-m' \beta v_{i,n}^{*2}/2), \quad (2.29)$$

$$p(v_{i,t}^*) = \sqrt{m' \beta / (2\pi)} \exp(-m' \beta v_{i,t}^{*2}/2), \quad (2.30)$$

with inverse temperature  $\beta$ . Then the final velocities of the solvent particle  $i$  and the colloid  $j$  after the collision read:

$$\mathbf{v}'_i(t + \Delta t) = \mathbf{v}_j(t) + \mathbf{L}_j(t) \times [\tilde{\mathbf{r}}'_i - \mathbf{r}_j(t)] + v_{i,n}^* \hat{\mathbf{e}}_n + v_{i,t}^* \hat{\mathbf{e}}_t, \quad (2.31)$$

$$\mathbf{v}_j(t + \Delta t) = \mathbf{v}_j(t) + \frac{m'}{m} [\mathbf{v}'_i(t) - \mathbf{v}'_i(t + \Delta t)], \quad (2.32)$$

$$\mathbf{L}_j(t + \Delta t) = \mathbf{L}_j(t) + \frac{m'}{I} [\tilde{\mathbf{r}}'_i - \mathbf{r}_j(t)] \times [\mathbf{v}'_i(t) - \mathbf{v}'_i(t + \Delta t)], \quad (2.33)$$

with the normal and tangential unit vectors  $\hat{\mathbf{e}}_n$  and  $\hat{\mathbf{e}}_t$ , the colloid's angular velocity  $\mathbf{L}_j$  and moment of inertia  $I = 2m(\sigma/2)^2/5$ .



# 3. Investigated Systems

## 3.1. Inverse Opals

A *porous material* consists of at least two immiscible phases of which one is usually a continuous solid material, the matrix, which surrounds the second phase of finely dispersed voids, containing a liquid, gas, or vacuum. Generally, two different classes of porous materials can be classified: if the void phase is comprised of disconnected and individually separated cavities, the material represents a *foam* structure. On the other hand, if the voids are connected to each other, the material represents a sponge structure or a so-called *porous network*.

In this work, we focus on nanometric porous networks, which offer, due to their highly accessible surfaces, specific properties concerning adsorption, mass and heat transport, and spatial confinement. Such a well-ordered structure can be fabricated by employing a colloidal dispersion as a template material (see Appendix C.2 for a more detailed description of the fabrication process). The most common type of colloidal crystals formed by self-assembly of monodisperse particles has a face-centered cubic lattice symmetry with the highest crystalline packing density of 74% volume filling. In this packing geometry, one sphere is in direct contact with 12 surrounding spheres. After the subsequent removal of the template, these contact points lead to orifices between the spherical voids (removed particles) in the resulting replica and consequently ensures an open, fully continuous three-dimensional network. Such porous systems are often referred to as *inverse opals* (abbreviated as i-opals in what follows), and can be characterized by the cavity radius  $R$  and pore diameter  $L$ . The angle of aperture is then defined as  $\vartheta_0 = \arcsin\left(\frac{L}{2R}\right)$ , and the distance of the opening as  $h = \sqrt{R^2 - L^2/4}$ .

Samples / Sizes	iO180-12/15	iO180-10/15	iO130-9/11
Thickness $d$ [ $\mu\text{m}$ ]	7.4	4.6	5.0
$R$ [nm]	75	75	55
$L$ [nm]	60	50	45
$L/R$	12/15	10/15	9/11

Table 3.1.: Geometrical characteristic dimensions (cavity radius  $R$ , pore diameter  $L$ ) for the inverse opals with thickness  $d$ .

Three different inverse colloidal crystals (*i-opals*) were fabricated. Table 3.1 summarizes the characteristic dimensions, cavity radius  $R$  and hole diameter  $L$ , obtained from the *scanning*

electron microscopy (SEM) images (see Figure C.1 in the Appendix C.2) of the i-opals along with their thickness  $d$ .

The three systems are characterized by different constraining geometries, expressed in the ratio  $L/R$  whose values can be varied by changing either the hole diameter at constant void radius (in the case of iO180-12/15 and iO180-10/15) or both in the case of iO130-9/11 membrane. For better comprehension, we provide a schematic representation of such a system in Figure 3.1.

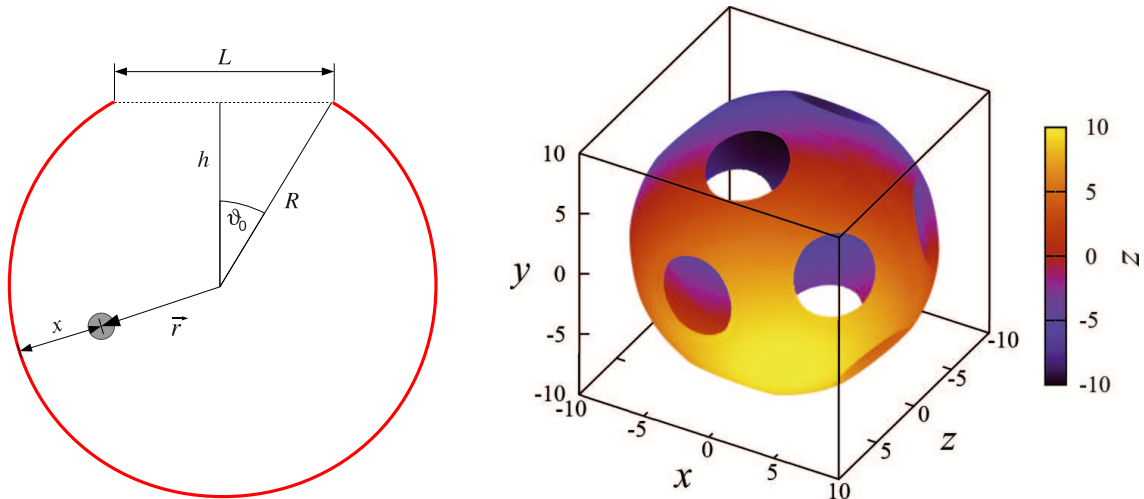


Figure 3.1.: Left panel: schematic representation of a tracer particle within a confining capped sphere with one opening. Right panel: actual inverse opal cavity employed in the simulations.

It is immediately apparent, that the confinement can induce restricted motion of diffusing molecules or particles in solutions inside an inverse opal. Depending on the size and the type of the mobile species even the entire diffusion mechanism may change. In this work, we model the particle-wall interactions via a shifted Yukawa-like potential:

$$U(r) = U(x) = \epsilon \frac{e^{-\kappa x/a}}{(x-a)^2}, \quad (3.1)$$

where  $\epsilon$  is the energy factor,  $\kappa$  is the inverse screening length,  $a$  is the radius of the tracer particle, and  $x$  denotes the shortest distance between the particle's center and the inverse opal, as shown in the left panel of Figure 3.1.

Let us briefly discuss the choice of the functional form and the values of the numerical parameters involved in the particle-wall interaction employed in Eq. (3.1) above. The main requirement for this potential is that it has to capture the effects of confinement. In this sense, and in the absence of any microscopic information on the form of the interaction,

the simplest choice would have been the hard-wall potential, which would diverge at  $x = a$  and vanish for all values  $x > a$ . However, such a choice is on the one hand impractical for BD simulations, since it would require the performance of costly, event-driven simulations, and on the other hand rather unrealistic, since it is expected that residual forces (dispersion, electrostatic *etc.*) are indeed present between the tracer and the confining walls. At the same time, we wish to keep the modeling as simple as possible. We therefore resort to capture with the interaction potential only the salient, key characteristics, namely:

1. The divergence at  $x = a$  which is guaranteed by the denominator,  $(x - a)^2$ , in Eq. (3.1).
2. A screened “electrostatic” nature, which is captured by the exponentially damped numerator,  $e^{-\kappa x/a}$ .
3. The independence of the interaction on the particle size  $a$ , which is guaranteed by Eq. (3.1) since, when the particle-wall distance  $x$  is expressed in units of  $a$ , the interaction takes a universal,  $a$ -independent form. In this way, we minimize the number of fit parameters and the effects of confinement are all captured in the ratio  $a/R$ , which does not explicitly enter the form of the interaction for distances  $x > a$ .

There are two parameters that have to be fixed, the strength  $\epsilon$  and the dimensionless inverse decay length  $\kappa$ . For the former, we choose a value  $\epsilon = 5$ , which corresponds to interaction energies of the order  $k_B T$  when the particle center lies a few particle radii away from the wall. On the other hand,  $\kappa$  is employed as the only fit parameter, under the assumption that the interaction becomes vanishingly small when  $x$  exceeds several particle radii. Comparison with experimental results (see Section 4.1) led us to fixing  $\kappa = 0.35$ , which corresponds to a decay length of about three particle radii, consistent with the underlying idea of putting focus onto confinement, as was mentioned above.

In our modeling, we have not taken hydrodynamic interactions *explicitly* into account, and focused instead on a combination of overdamped dynamics with the effects of the confining cavities. Nevertheless, the influence of hydrodynamics are *implicitly* included in the simulations through the fitting of  $\kappa$ . Indeed, the fact that  $\beta U(r)$  decays over roughly three particle radii, which is typical for the HI between a sphere and a plane, indicates that, additionally to the short-ranged steric and electrostatic interactions, hydrodynamics *do* play an important role. However, this simplified approach is clearly justified in two distinct limits. For  $a/R \ll 1$ , the physical size of the particle is so small that explicit hydrodynamic interactions are indeed negligible. For  $a \rightarrow L/2$ , the dominant effect bringing about the delay in the particle diffusion is the bottleneck caused by the hindrance of the tracer to pass through the connecting pores between two spherical cavities of the inverse opal. To keep the modeling

as simple as possible and to bring forward the effects of the confining walls, we have thus chosen not to model HI explicitly for all intermediate sizes of the tracer particle as well. The remarkable agreement between experimental and simulation results offers *a posteriori* justification for our approximations. We emphasize that the *same* interaction and numerical parameters were used to model *all* experimental results.

## 3.2. Linear and Branched Polymers

A polymer is a macromolecule, which consists of many branched and linked molecules, where the single components of this construct are called *monomers*. A well known example is *polyethene* typically consisting of  $10^2$  to  $10^4$  ethene groups, which after polymerization form single C-C bonds around which the polymer can freely rotate (see Figure 3.2). Another

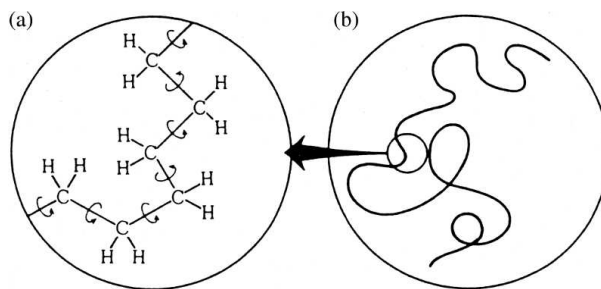


Figure 3.2.: The atomic structure of a polyethene molecule, where the rotational freedom around each C-C bond is illustrated by the circular arrows (a). Schematic representation of the entire, flexible polymer chain (b).

example is DNA with its double-helix structure, in which two strands are connected through hydrogen bonds. DNA molecules can consist of up to  $10^{10}$  monomers, and would span over 1 m in an unfolded state. The persistence length of such polymers, *i.e.* the length over which correlations in the direction of the tangent are lost, is very short (on a length scale of 1 nm). Therefore, such flexible polymers are not elongated in solution but rather form randomly curled coils.

Semi-synthetic polymers entered the scene on the verge of the 19th century with viscose, a chemically modified variant of cellulose. Entirely synthetic polymers were developed in particular after the acceptance of Staudinger's hypothesis that polymers consist of covalently bonded, linear chains of monomers [64, 65]. A very peculiar type of synthetic polymers are the so-called *dendrimers*, which are macromolecules with defined architectures that are synthesized by iterative controlled reaction steps [66]. The conformation of subsequent generations on a trifunctional monomer core results in a treelike structure. Hence, these polymers

have been termed *dendrimers* - from the Greek word “*δένδρον*” for tree. A typical example of a fourth-generation dendritic structure is shown in Figure 3.3.

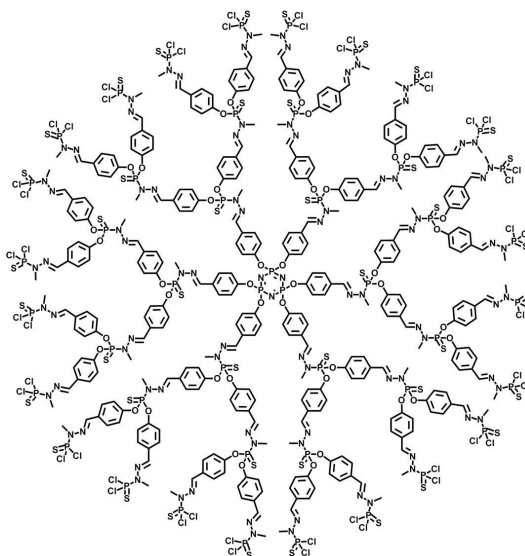


Figure 3.3.: Structure of a fourth-generation dendrimer (courtesy of Ed de Jong).

Even though the first dendrimers have been prepared as early as 1978 by Vögtle *et al.* [67], this field received only little attention until 1990 when Tomalia *et al.* indicated a large number of possible applications of such molecules [68]. Ever since, the research on dendrimers has been a highly active field. First, their peculiar architecture establishes them as hybrid model systems between polymer chains and hard colloids in terms of both the sphericity and compactness of their conformations. Furthermore, it has been shown in Ref. [24] that dendrimers exhibit a similar softness in their effective interactions.

In order to analyze the behavior of dendrimers from a theoretical point of view, it is necessary to design a proper model system. The simplest case is that of *ideal dendrimers*, namely, dendrimers that consist of non-interacting and point-like monomers. At a first glance this model seems unrealistic as it does not bear much resemblance with a real dendrimer. Nonetheless, this model still represents a useful reference system in which many interesting quantities, such as the radius of gyration [69, 70] and the form factor [71], can be calculated analytically.

In good or athermal solvent conditions however, the steric excluded-volume interactions between the monomers have to be taken into account, since it is expected that these will lead to significant swelling and alterations in the configuration of the polymer. The first studies on this subject were performed by de Gennes and Hervet [72]. They considered flexible trifunctional monomers with very long spacers in an athermal solvent and obtained a density profile with a global minimum at the center and a monotonic increase towards

the outer regions (shell) of the polymer. Such a density distribution is known as the *dense-shell* or *hollow-center* model. However, their force-balance calculations assumed implicitly that each successive generation of monomers occupies a concentric shell of its own, which lies at a farther radial distance from the dendrimer center than the preceding one. Hence, the finding of the hollow-center does not come as a surprise. These authors also discovered that the radius of gyration scales with  $R_g \sim N^{1/5}$ , yielding an effective fractal dimension of  $d_f = 5$  for dendritic structures. Since this value exceeds the spatial dimension, it follows that a limiting generation number exists, beyond which no perfect dendrimers can be grown anymore. Although these results caused some initial excitement, more recent simulations and experiments demonstrated that the dense shell model is *not* valid [73]: due to thermal fluctuations of the monomer groups, a considerable degree of backfolding occurs, causing an increase in the monomer density at the center of the macromolecule (*dense-core*). Thus, the apparent dense shell picture seen in Figure 3.3 is misleading if it is interpreted literally: the chemical endgroups do *not* lie in the outer region of the dendrimer, but rather fluctuate and are allowed to explore the inner parts of the molecule as well.

The issue of dendrimer conformations becomes even more complex when charged or polyelectrolyte dendrimers are considered. Such charges on the building blocks of, *e.g.* PAMAM (polyamidoamine) dendrimers can be manipulated by changing the pH of the solution or by the addition of salt. Theoretical and experimental research has already been done in this area [74, 75] with the finding that in the case of monovalent monomers, the size and the conformation of a dendrimer is almost completely insensitive to changes of the pH value. Yet, a considerable stiffening and stretching of the bonds occurs when the dendrimer carries divalent chargeable groups, which release two monovalent counterions per site [76]. Thus, dendrimers are of enormous practical interest since this possibility to switch from dense-shell to dense-core configurations and *vice versa* establishes them as promising candidate carrier molecules for drug delivery [44, 77, 78].

A common approach for physically modeling the configuration of polymers is to treat the individual monomers (Kuhn segments) as spherical beads interacting by potentials that depend on their mutual spatial separation. Such a bead-spring model reduces the complex chemical structure of polymers to an extremely simple representation. Although such a model seems oversimplified at first, it is still able to capture the essential physical properties of the original systems, but at significantly reduced computational costs.

In this work, we consider two different types of pair interactions between the individual monomers. The first contribution models the short-range excluded-volume interactions between the monomers. This purely repulsive interaction can be parameterized, for instance,



by a simple, shifted and truncated *Lennard-Jones* potential, which reads:

$$U_{\text{mm}}(r) = \begin{cases} 4\epsilon \left[ \left(\frac{\sigma}{r}\right)^{12} - \left(\frac{\sigma}{r}\right)^6 \right] + \epsilon, & r \leq r_{\text{cut}} \\ 0, & r > r_{\text{cut}} \end{cases} \quad (3.2)$$

with  $r = |\mathbf{r}_i - \mathbf{r}_j|$  denoting the separation between the monomers  $i$  and  $j$ , whose position vectors are  $\mathbf{r}_i$  and  $\mathbf{r}_j$ , respectively. In this equation, the parameter  $\sigma$  relates to the diameter of a monomer, and  $\epsilon$  specifies the strength of the interaction. Furthermore, we have chosen the cutoff distance in Eq. (3.2) as  $r_{\text{cut}} = 2^{1/6}\sigma$ , rendering the monomer-monomer interaction purely repulsive and thus suitable for an effective description of athermal solvents.

The second interaction potential models the chemical links between bonded monomers. In this work we opted for the so-called *finitely extensible nonlinear elastic* (FENE) potential,  $U_{\text{FENE}}(r)$ , which is given by [79]:

$$U_{\text{FENE}}(r) = \begin{cases} -U_0 \left(\frac{r_0}{\sigma}\right)^2 \ln \left[ 1 - \left(\frac{r}{r_0}\right)^2 \right], & r \leq r_0, \\ \infty, & r > r_0 \end{cases} \quad (3.3)$$

where the location of divergence at  $r_0$  determines the maximum bond length between two monomers; it can be used along with  $U_0$  to tune the stiffness of bonds between the monomeric units. In our simulations we have chosen  $U_0 = 5.0$  and  $r_0 = 4.0$ , leading to rather soft and elastic connections. This is the same model used for dendrimers under shear in Ref. [44]. The effective potential between two adjacent polymer beads,  $U_{\text{eff}}(r) = U_{\text{mm}}(r) + U_{\text{FENE}}(r)$ , is shown in the left panel of Figure 3.4.

In addition to these intramolecular forces, the polymer interacts with the system boundaries (*i.e.* the channel walls) *via* the potential  $U_{\text{wall}}(x)$ , which is given by:

$$U_{\text{wall}}(x) = \begin{cases} \frac{2}{3}\pi\epsilon \left[ \frac{2}{15} \left(\frac{\sigma}{x}\right)^9 - \left(\frac{\sigma}{x}\right)^3 + (1 - \lambda_w) \frac{\sqrt{10}}{3} \right], & 0 \leq x \leq (2/5)^{1/6}\sigma \\ \frac{2}{3}\pi\epsilon\lambda_w \left[ \frac{2}{15} \left(\frac{\sigma}{x}\right)^9 - \left(\frac{\sigma}{x}\right)^3 \right], & x > (2/5)^{1/6}\sigma, \end{cases} \quad (3.4)$$

for a wall lying in the  $(y, z)$ -plane at  $x = 0$ . The total external potential, caused by two walls separated by  $D$  is thus given by  $U_{\text{ext}}(x) = U_{\text{wall}}(x) + U_{\text{wall}}(D - x)$ . The attractiveness of the potential can be adjusted by the parameter  $\lambda_w$ . In the right panel of Figure 3.4, we show plots for the extreme cases  $\lambda_w = 0.0$  (purely repulsive) and  $\lambda_w = 1.0$  (attractive wall) for a slit-like channel of width  $D = 4.0$ .

The linear polymers are then created by a three-dimensional self avoiding random walk. For dendrimers, we use the same approach but start with a central pair of joined monomers,

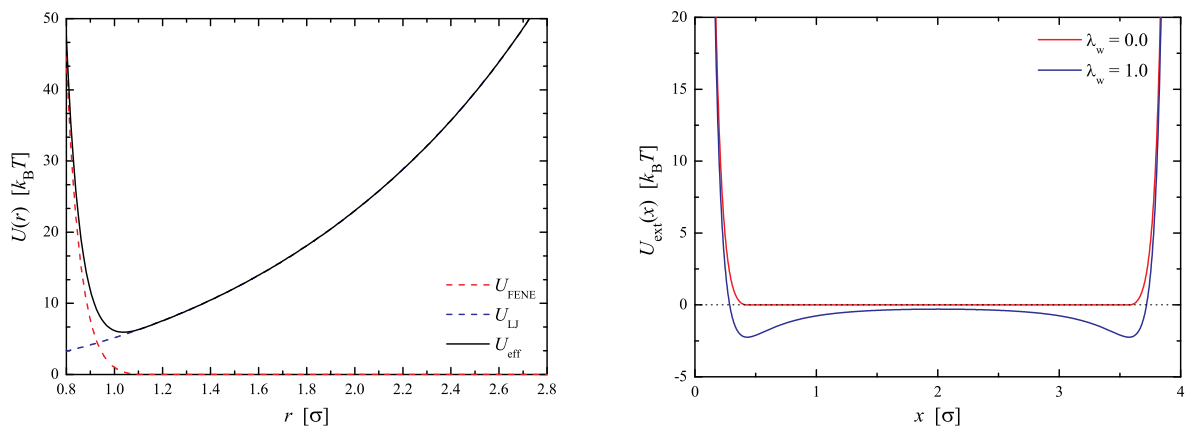


Figure 3.4.: Left panel: effective interaction potential  $U_{\text{eff}}(r)$  between two adjacent polymer beads. Right panel: the external wall potential acting on a monomer of the polymer, for a channel with width  $D = 4.0$ , see Eq. (3.4). The choice  $\lambda_w = 0.0$  mimics purely repulsive walls, while  $\lambda_w = 1.0$  adds a long-ranged attractive tail to the potential.

the so-called zeroth generation  $G = 0$ . A successive layer of monomers is then formed by connecting two additional beads to each outer monomer of generation  $G$ . Thus, the functionality of the dendritic structure is  $f = 3$ , and the number of monomers  $N(G)$  taking part to a given generation  $G$  follows a simple power law, *i.e.*  $N(G) = 2^{G+2} - 2$ .

The analysis of the shape and size of isolated dendrimers plays a key role in understanding not only the properties of the molecules themselves but also the thermodynamics of concentrated dendrimer solutions in a coarse-grained approach [24]. A convenient measure for the *overall size* of polymers is given by the so-called *radius of gyration*  $R_G$ , defined as:

$$R_G^2 = \frac{1}{N} \left\langle \sum_{i=1}^N (\mathbf{r}_i - \mathbf{r}_c)^2 \right\rangle, \quad (3.5)$$

where  $\mathbf{r}_c$  denotes the center of mass position and  $\langle \dots \rangle$  the statistical average over all conformations. In order to quantify the structural properties and the alignment of polymers in flow, we consider the average gyration tensor of the molecule,  $G_{\alpha\beta}$ , defined as:

$$G_{\alpha\beta} = \frac{1}{N} \sum_{i=1}^N \langle r_{i,\alpha} r_{i,\beta} \rangle, \quad (3.6)$$

where  $r_{i,\alpha}$  is the  $\alpha$ -component of the position vector of the  $i$ -th monomer relative to the center of mass, and  $\alpha, \beta \in \{x, y, z\}$  denote Cartesian coordinates. This quantity is directly accessible in scattering experiments, and it is obvious that its diagonal components,  $G_{\alpha\alpha}$ , are

the squared radii of gyration in  $\alpha$  direction. The bulk values of the gyration radii for the systems simulated in this work are summarized in Table 3.2.

Polymer architecture	$N$	$R_G [\sigma]$
Linear	32	$3.85 \pm 0.65$
Linear	62	$5.63 \pm 0.94$
Linear	92	$7.19 \pm 1.24$
Dendritic (G2)	14	$1.62 \pm 0.03$
Dendritic (G3)	30	$2.18 \pm 0.04$
Dendritic (G4)	62	$2.78 \pm 0.04$

Table 3.2.: The radii of gyration for linear and dendritic polymers considered in this thesis.

### 3.3. Cluster Crystals

Statistical-mechanical studies of freezing have traditionally relied on model systems with very simple *unbounded* repulsive forces. Frequently occurring examples are the hard sphere model and inverse-power pair potentials. These elementary cases have led to valuable insights into the freezing behavior of monatomic substances. Yet, much less is known about interaction potentials that are *bounded*, thus allowing full and multiple particle overlap. Though surprising and unphysical at first glance, this condition is fully legitimate and natural for fractal, polymer-based colloids.

Many different realizations exist for such bounded potentials, but the arguably best known representatives are the *Gaussian core model* (GCM):

$$U_{\text{GCM}}(r) = \epsilon \exp \left[ - (r/\sigma)^2 \right], \quad (3.7)$$

and the *penetrable sphere model* (PSM):

$$U_{\text{PSM}}(r) = \begin{cases} \epsilon, & r < \sigma \\ 0, & \text{else} \end{cases}. \quad (3.8)$$

In his seminal work from 1976, Stillinger studied the phase diagram of the former [80], and observed a first order phase transition from the fluid to a crystalline cubic phase with a singly occupied lattice, when the GCM-system was compressed at constant  $T$ . Upon further increase of the density, and depending on the temperature, the system might undergo a structural phase transition, but eventually, the solid will melt again. Therefore, this behavior is called

“re-entrant melting” (see left panel of Figure 3.5). Surprisingly, the PSM-system exhibits a completely different phase behavior, as illustrated in the right panel of Figure 3.5: upon increasing the density at fixed temperature, homogeneously sized clusters of overlapping particles begin to form which arrange themselves in an ordered phase.

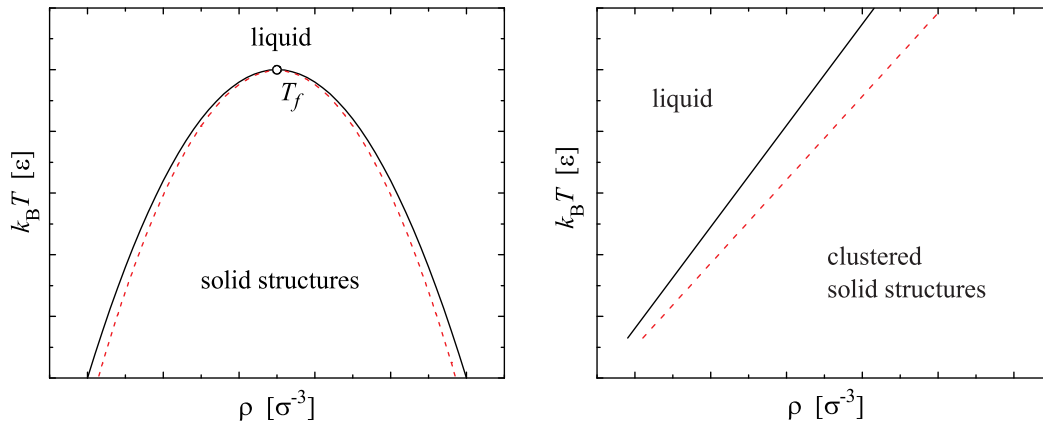


Figure 3.5.: Schematic representation of the topology of the phase diagrams of the Gaussian core model (left panel) and the penetrable sphere model (right panel). Lines show the phase boundaries for the liquid (solid black) and the solid phase (dashed red). The gap in-between denotes the coexistence region. While the GCM shows re-entrant melting below an upper freezing temperature  $T_f$ , the PSM freezes at all temperatures into crystals with multiply occupied lattices sites.

The fact that the GCM and the PSM belong to the same class of bounded, purely repulsive interactions, yet react in such a contrary fashion to an increase in density, immediately asks for an explanation. In order to elucidate this discrepancy, we first reformulate both Eq. (3.7) and Eq. (3.8) within the framework of the so-called *generalized exponential model* with index  $n$  (GEM- $n$ ):

$$U_{\text{GEM-}n}(r) = \epsilon \exp[-(r/\sigma)^n]. \quad (3.9)$$

As can be seen in Figure 3.6, the potential interpolates smoothly, *via* the index  $n$ , between the Gaussian core model ( $n = 2$ ) and the penetrable sphere model ( $n \rightarrow \infty$ ). Obviously, the main difference between both model potentials is the value of  $n$ , *i.e.* the steepness of the interaction, which should therefore play a crucial role.

Indeed, Likos *et al.* established a criterion to decide whether clustering or re-entrant melting will be observed in a system where particles interact *via* ultrasoft, purely repulsive potentials [81]. Based on the analysis of the behavior of the structure factor within the *mean field approximation* (MFA), the criterion applies to all bounded pair interactions  $U(r)$  which decay sufficiently fast to zero, such that they are integrable and their Fourier transforms

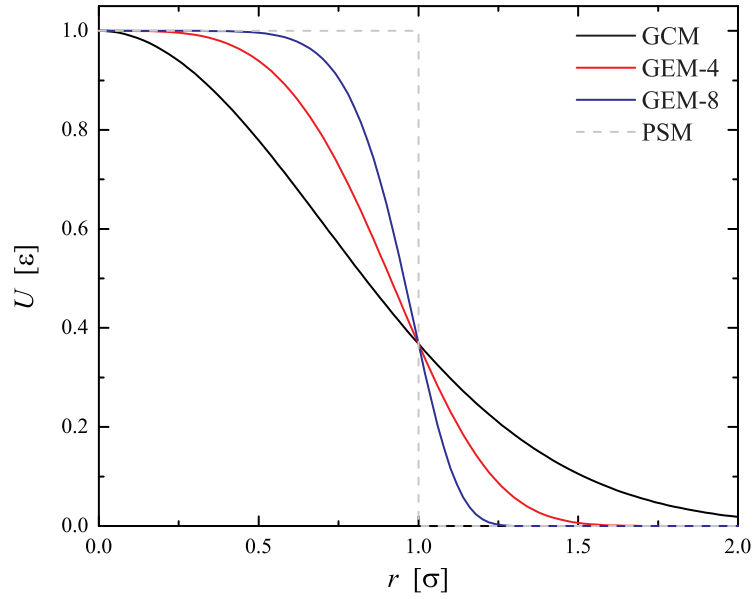


Figure 3.6.: Four members of the GEM- $n$  family: the GCM ( $n = 2$ ), the GEM-4, GEM-8 and the PSM ( $n = \infty$ ).

exist. Under these conditions, there are two possibilities for the functional form of the Fourier transform  $\tilde{U}(k)$ , where  $k$  is the wave number:

- $\tilde{U}(k)$  is a non-negative and monotonically decaying function, *i.e.*  $\tilde{U}(k) \geq 0$  for all  $k$ . In what follows, we will refer to such potentials as  $Q^+$ -potentials, and a system of such particles will show re-entrant melting. The fact that the Gaussian function is an eigenfunction of the continuous Fourier transform induces that the GCM belongs to this class of potentials.
- $\tilde{U}(k)$  oscillates, and attains negative values for certain ranges of the wave number  $k$ . Such potentials are called  $Q^\pm$ -potentials in what follows, and are expected to lead to a clustering behavior. The PSM is a representative of this interaction class.

Now, in order to determine to which class a potential belong, an explicit evaluation of  $\tilde{U}(k)$  is not required. Instead a sufficient condition can be deduced along the following lines [82]: we start from the inverse Fourier transform of a (bounded) pair potential  $U(r)$ :

$$U(r) = \frac{1}{2\pi^2} \int_0^\infty \frac{\sin(kr)}{kr} \tilde{U}(k) k^2 dk. \quad (3.10)$$

Then, the second derivative of  $U(r)$  at  $r = 0$  is given by:

$$\frac{d^2U(r=0)}{dr^2} = -\frac{1}{6\pi^2} \int_0^\infty \tilde{U}(k)k^4 dk. \quad (3.11)$$

Thus, if the left hand side of Eq. (3.11) is larger than zero, then  $\tilde{U}(k)$  *must* necessarily have negative parts and  $U(r)$  is a  $Q^\pm$ -potential.

Returning to the GEM- $n$  interaction class at hand, the second derivative of  $U_{\text{GEM-}n}(r)$  reads:

$$\frac{d^2U_{\text{GEM-}n}(r)}{dr^2} = \frac{\epsilon n}{\sigma^2} \exp[-(r/\sigma)^2] \left[ n \left(\frac{r}{\sigma}\right)^{2(n-1)} - (n-1) \left(\frac{r}{\sigma}\right)^{n-2} \right]. \quad (3.12)$$

This expression reveals that the transition from the  $Q^+$  to the  $Q^\pm$  class precisely occurs at  $n = 2$ . Hence, for sufficiently high densities, all systems interacting *via* a GEM- $n$  (with  $n > 2$ ) potential will form cluster crystals. One peculiar property of these cluster crystals is, that their lattice constant is entirely *independent* of the particle density  $\rho$ . Instead, the occupancy per lattice cite,  $N_C$ , scales linearly with  $\rho$ . A rigorous theoretical explanation of this effect has been provided in Ref. [82] and confirmed by Monte Carlo simulations in Ref. [83]. At the freezing transition, a clustering system adapts its lattice constant  $a$  in such a way that the modulus of its shortest reciprocal lattice vector coincides with the wave number  $k_{\min}$ , where  $k_{\min}$  denotes the position of the first negative minimum of  $\tilde{U}(k)$ . This value depends neither on the density  $\rho$  nor on the temperature  $T$ , but solely on the functional form of the pair potential  $U(r)$ . Thus  $a \sim k_{\min}$  holds for the lattice constant, and for the occupation number  $N_C \sim \rho$ , respectively.

Cluster crystals can be realized by using, *e.g.*, suitably synthesized amphiphilic dendrimers of the second generation (G2) as penetrable, soft colloids [28]. The ability of such molecules to spontaneously cluster in the fluid phase has recently been demonstrated by monomer-resolved computer simulations [29].

Hence, the interior of the clusters locally resembles a semi-dilute polymer solution and features a *local* viscosity,  $\eta_C$ , which exceeds that of the surrounding solvent,  $\eta$ . This viscosity mismatch  $\Delta\eta = \eta_C - \eta$  is not explicitly taken into account in the simulation model, in which the dendrimers are coarse-grained by means of their effective interaction potential and are thus modeled as point particles. This simplification does not affect the validity of the physical results (see Chapter 5), as will be demonstrated in what follows.

To begin with, we show that the viscosity difference  $\Delta\eta$  is minimal. Huge viscosity mismatches are commonly encountered in concentrated solutions of long linear polymers, and they are predominantly caused by *entanglements* between these molecules. In contrast, the dendrimer models relevant to this work are free of entanglements. Indeed, the G2-dendrimers

at hand have a very small number of total monomers,  $N = 14$ , and furthermore, the number of monomers along any linear strand of the same,  $N_s$ , is even smaller,  $N_s = 6$  [28]. As such, the entanglement length  $N_e$  is always of the same order as  $N_s$ , and hence, even in the absence of shear, entanglement does not play a role in setting a distinct, slow time scale for the dynamics. The rapid disentanglement of neighboring strands is further facilitated by the fact that the arms of the G2-dendrimers are fully flexible.

Since the polymer dynamics is disentangled, we are able to employ now standard results from the theory of semi-dilute, disentangled polymer solutions, to estimate the above mentioned viscosity difference  $\Delta\eta$ . We take arguments from the results for linear chains, and we assume as an estimate Rouse dynamics, though the Zimm model leads to very similar results. Standard analysis of polymer dynamics leads to [84]:

$$\Delta\eta \cong N\phi\eta, \quad (3.13)$$

where  $\phi = (\pi/6)\rho\sigma^3$  is the monomer volume fraction. Typical values of monomer fractions at clustering are  $\phi \cong 0.1$  or less [29]. With  $N \cong 10$  for the G2-dendrimers, we obtain:

$$\Delta\eta \cong \eta. \quad (3.14)$$

The small  $N$ -value for the cluster-forming dendrimers, that bring about an experimental realization of our system, is the key in (a) avoiding entanglements and (b) making the internal viscosity of the dendrimers of the same order as that of the solvent. Thus, there is minimal mismatch between the two quantities, as readily seen in Eq. (3.14) above, and therefore the dynamics are *not* significantly slowed down when one particle moves through another.

Finally, if any discrepancy exists between the two viscosities, it will only lead to a delay of the transient dynamics, *i.e.* to a prolongation of the time needed to break the clusters under the application of *steady* shear (see Chapter 5). Whichever internal time scale  $\tau_{\text{int}}$  is associated with the dissociation of the soft colloids from the cluster they populate at equilibrium, the time scale of action of the flow,  $\tau_{\text{shear}} \sim 1/\omega$ , is infinite for the case of steady external shear (oscillatory shear frequency  $\omega = 0$ ).





# 4. Diffusion and Translocation in Porous Materials

Mass transport has attracted strong interest since the first observation of Brownian motion in the 19th century. Diffusive and driven particle transport are ubiquitous in nature and are at work in many processes and applications including bio-related fields [85, 86], energy conversion and storage (fuel and solar cells) [87], separation membranes [88] and microfluidics [89, 90]. With increasing complexity of such novel devices it becomes evident that mass transport has to be understood on a variety of time and length scales. Alongside with the elucidation of the diffusion law [91–93] comes the increase in interface and geometrical constraints of the motion [94]. Constrained macromolecular transport underlies many separation methods [95, 96], plays an important role in intracellular and extracellular particle transportation [97] and, in addition, it has important ramifications of fundamental scientific interest [78]. Therefore, extensive research across different disciplines [30, 97] and diverse materials [91, 92, 98] was devoted in establishing diffusion laws and relationships to geometrical and topological characteristics of the diffusing species and medium.

The advent of powerful experimental techniques allowing single molecule detection, the fabrication of patterned nanostructures with build-in spatial constraints, and the development of computational tools conveyed the exploration of transport dynamics in complex environments [89, 91, 93, 99, 100]. The earlier experiments [90, 94] on large DNA molecules for direct visualization indicate that switching from disordered to patterned media hold promise for a better understanding of the diffusion fundamentals and improved performance of devices for the different applications. The strategy to use patterned systems to obstruct particle transportation has been implemented through micro-fabrication of fluidic devices [89, 90] and colloidal templates [94], respectively, for size dependent trapping and diffusion through molecular size obstructions. Extension to nanoporous systems was exemplified in surfactant-templated mesoporous silica for diffusion and interaction-controlled mass transport [98] and drug-delivery [85, 100].

However, unique assignment of the role of geometrical and topological characteristics of periodic nanostructures on the basic diffusion mechanisms is more suitably performed on simple rigid probes rather than on long biopolymers with configurational freedom and complex interactions with the walls of the patterned media. Therefore, we studied the tracer diffusion of spherical *quantum dot particles* (abbreviated as QDs) confined in a three-dimensional inverse

opal with well-defined highly ordered structure and different geometrical constraints using the single molecule technique of *fluorescence correlation spectroscopy* (FCS) [98, 101–104]. Additionally, we have performed Brownian dynamics simulations and compared our results to the experimental findings to better understand the diffusion process in the confined environment.

In the second part of our studies, we extended this problem to flexible polymers flowing through narrow channels. This subject has recently attracted considerable attention due to its relevance concerning, for example, biological applications of microfluidics [105], sequencing DNA by passing it through nanopores [106, 107] and the passage of biomolecules through membrane channels [108]. Accordingly, a great deal of experimental, theoretical and simulation effort has been devoted to it, and we refer to Ref. [109] for a list of relevant references. In most cases, a flat membrane with a single opening is considered, with a linear polymer chain translocating from one side to the other. The driving forces behind this phenomenon can have a multitude of physical origins, including a chemical potential gradient across the partition [110–112], external fields, such as voltage [113], or preferential adsorption of the chain on one side of the membrane [109, 114].

The process by which a polymer moves through a narrow channel can be divided into three stages. First of all, the polymer must find the opening, second it must squeeze into the constriction, and only then can it move through the micro-channel. Here, the issue of interest is whether the external current is strong enough to cause insertion, and then how the polymer propagates within the constriction. We first derive an analytic expression for the threshold flux, needed to push a dendrimer into a narrowing in Section 4.2.1. Then we present the results from our computer simulations in Section 4.2.2, and compare them to the predictions from theory.

### 4.1. Confined Diffusion in Periodic Porous Nanostructures

The diffusion of several fluorescent probes (see Table C.1 in the Appendix C.1) in inverse opals was studied experimentally by FCS. The method is based on measurement of the fluctuations of the fluorescent light intensity caused by the excursion of fluorescent probes through an extremely small observation volume ( $< 1 \mu\text{m}^3$ ) defined by the focus of a confocal microscope. This technique has been recently utilized to probe one-dimensional diffusion of molecular and macromolecular tracers in nanoporous alumina membranes [115, 116] and three-dimensional diffusion of molecular tracers in silica inverse opals [117]. The former has simply shown the feasibility of the technique to measure the retarded mobility inside the nanopores, while the very recent study in large void opals reported on complex non-Fickian

diffusion. The autocorrelation function  $G(t)$  was measured in the free solution and for the different confinements, and the key finding was that the restricted environment exerted a clear slowdown effect on the center of mass motion of the tracer particles. These experiments have been carried out by the group of Prof. George Fytas at the *Max Planck Institute for Polymer Research* in Mainz, and at the *Foundation for Research and Technology* in Heraklion, and for a more detailed description of the experiment, the reader is referred to the Appendix C. In what follows, we will discuss and theoretically rationalize the experimental observations.

We make use of the Einstein-Stokes equation to relate the short-time diffusion coefficient  $D_S$  to the drag coefficient  $\xi = 6\pi\eta a$ , which leads to the relation:

$$D_S = \frac{k_B T}{\xi}. \quad (4.1)$$

We verified the correct implementation of our BD algorithms by measuring the mean-square-displacement of a free particle (vanishing deterministic force on the particle,  $\mathbf{F}(r) = 0$ ), calculating the long-time diffusion coefficient  $D_{\text{free}}$  via the relation  $\langle \Delta \mathbf{r}^2(t) \rangle \equiv \langle [\mathbf{r}(t) - \mathbf{r}(0)]^2 \rangle = 6D_{\text{free}}t$ , and checking that  $D_{\text{free}} = D_S$ . In other words, for free particles long- and short-time diffusion coefficients coincide.

The coincidence of the long- and short-time diffusion coefficients is no longer valid anymore in the confined case. Instead, the long-time diffusion coefficient  $D$  strongly depends on the ratio  $L/R$ , which together with the number of openings per void (twelve for our i-opals) determines the size of the permeable surface. In addition, the tracer-to-cavity size ratio,  $a/R$ , is expected to have a clear influence on diffusivity as well, so that we end up with a long-time diffusion coefficient  $D = D(L/R, a/L)$ . This coefficient is highly correlated to the escape probability, and we can distinguish between two extreme cases: if the penetrable area approaches the surface area of the void (that is the theoretical limit in which no solid surface would exist anymore), then we would end up with  $D = D_S$ . The opposite extreme case would be an escape volume that is vanishingly small, *i.e.* if there were no openings in the cavity. In such a situation, the diffusing particle would never be able to escape its confining volume. Additionally, the tracer size plays also a significant role concerning the diffusion process: first, it directly influences the short time diffusion coefficient in Eq. (4.1) and thus the velocity of the diffusing tracer; second, the larger  $a$  is chosen, the smaller one can consider the escape area to become at fixed  $L$  and  $R$ , until it vanishes completely at  $a = L/2$ . A sketch of the diffusion process for two different tracer sizes is shown in Figure 4.1.

Following the present information from the experiments, we have chosen values of the particle radius belonging in the interval  $a/R \in [0.01, 0.30]$ , which approach the aforementioned case  $a \rightarrow L/2$  at the upper limit. In order to analyze this transitional regime, we mea-

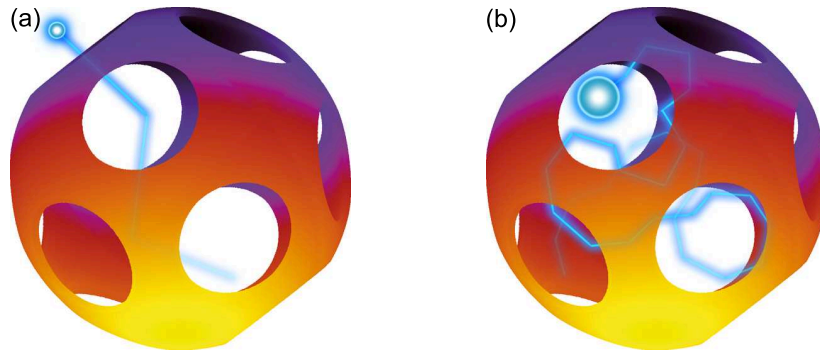


Figure 4.1.: A sketch of the process of multiple collisions that a tracer particle undergoes against the cavity walls before it escapes to the neighboring cavity. For small ratios  $a/L$  between particle size and cavity openings, panel (a), a small number of bounces suffices but for large ones, panel (b), a large number of collisions with the walls takes place before the particle escapes.

sured the mean escape time  $\langle \tau_{\text{esc}} \rangle$  of the embedded particle from the cavity of the inverse opal, where the brackets  $\langle \dots \rangle$  denote an ensemble average over different realizations of the thermal fluctuations. The diffusion through the inverse opal can then be seen in a coarse-grained fashion in time, as a random walk on a lattice of step  $\sim R$  and waiting time  $\langle \tau_{\text{esc}} \rangle$  on each lattice site, leading to an expression for the long-time diffusion coefficient  $D$ , which is well-known from the theory of random walks, namely,  $6D = R^2 / \langle \tau_{\text{esc}} \rangle$ .

In the case of a free particle of radius  $a$ , the expected escape time from a cavity of radius  $R$  can be written as  $\langle \tau_{\text{esc}} \rangle = \tau_{\text{free}}$ , where:

$$\tau_{\text{free}} = \frac{R^2 \pi \eta a}{k_B T}. \quad (4.2)$$

Eq. (4.2) immediately leads to  $D_{\text{free}} \sim a^{-1}$ , as experimentally found for the tracer diffusivities in the free solution (note that the sphere of radius  $R$  in Eq. (4.2) is fictitious). Moreover, we define a timescale  $\tau_0$ , which is independent of the particle size and it corresponds to the time needed for a free particle of radius  $R$  to escape from a “cavity” of the same size, *viz.*:

$$\tau_0 = \frac{R^3 \pi \eta}{k_B T}. \quad (4.3)$$

The advantage of setting  $\tau_0$  as the unit of time in our simulations is that we can directly compare the expectation values of the escape times  $\langle \tau_{\text{esc}} \rangle$  for arbitrary combinations of the parameters  $a/L$  and  $L/R$  and immediately translate ratios of the same into the slowdown factor, which is the quantity measured in the experiments. Note also that in this way, we can

rewrite Eq. (4.2) as  $\tau_{\text{free}} = a\tau_0/R$ , which is exact for a free particle. To gain a feeling about orders of magnitude, we quote a typical value of  $\tau_0 \approx 1$  ms for a setup in which  $R \approx 100$  nm in aqueous solvent and at room temperature. Finally, we note that the above considerations hold only if the long-time motion of the particle is indeed diffusive, *i.e.*, if the mean-square displacement scales linearly with time, an assumption that will be shown to hold in what follows.

The comparison between the experimental diffusion times is visualized in Figure 4.2. Here, the slowdown factor  $\zeta$  is plotted against the ratio  $a/R$ , which is a measure of the confinement, and for the three different  $L/R$ -values. The delay factor is calculated as  $\zeta \equiv \langle \tau_{\text{esc}} \rangle / \tau_{\text{free}}$  in the BD simulations and  $\zeta \equiv \tau(\text{in i-opals}) / \tau(\text{in free solution})$  in the FCS experiment. The two main experimental findings are discussed in what follows.

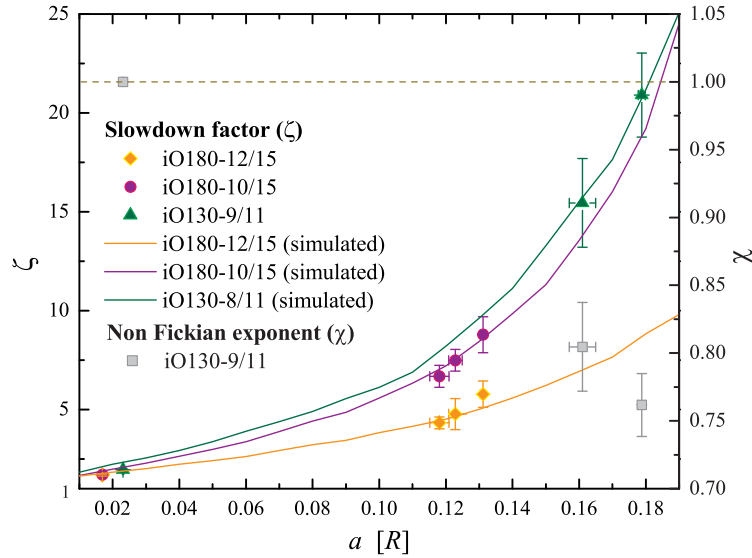


Figure 4.2.: The slowdown factor  $\zeta$  for the i-opals as a function of the reduced radius  $a/R$ : symbols denote experimental data, continuous lines simulation data. The right vertical axis shows the value of the exponent  $\chi$  in the time dependence of the tracer mean square displacement.

First, even in the limiting case  $a \ll R$ , the value  $\zeta_0$  of the slowdown factor remains strictly larger than one, implying that even in the ideal, point-particle case ( $a/R \rightarrow 0$ ), a confined probe is slower than a free one. Though the strict case is problematic from a mathematical point of view, since the particle would formally experience vanishing friction with the solvent [see Eq. (4.1)], the finding is physically intuitive: a free and a confined point particle need the same time to reach a distance  $R$  *via* diffusion but whereas the free particle then immediately “escapes”, the confined one will only do so if it happens to hit the cavity at the opening, otherwise it will remain confined and will attempt to escape with subsequent diffusive motion.

In this respect, we expect the quantity  $\zeta_0$  to become insensitive to the particle size and to depend mainly on the ratio  $L/R$ , albeit in some weak fashion. From the simulation, and if we were indeed in the limit in which the ratio  $a/R$  was so small as to be irrelevant, we would expect  $\zeta \approx \zeta_0$  to drop monotonically with the ratio  $L/R$ , which is not yet the case for the smallest values,  $a/R = 0.01$  considered there. Therefore, the particle size is still relevant and so we can conclude by extrapolation that the limiting value  $\zeta_0$  should depend rather weakly on the opening-to-cavity ratio  $L/R$ . In fact, the simulated  $\zeta_0 = 1.7$  (iO180-12/15) and  $\zeta_0 = 1.9$  (iO180-10/15) follow this anticipated trend.

These values capture well the experimental  $\zeta_0 = 1.80 \pm 0.06$ , for the smallest tracer, T1.3. In the case of the third i-opal (iO130-9/11), for which an anomalous diffusion is observed (see below), the simulations overestimate the experimental value by about 20% (*c.f.* Figure 4.2). This deviation, though still within fairly good limits of agreement, could easily be taken care of by employing slightly different parameters for the diffusant-wall interaction. However, for reasons of consistency and parsimony, we refrained from doing so in the modeling at hand. In this context, we note that the translational motion for all four tracers in i-opals with  $a/R < 0.14$ , realized with the same cavity radius  $R = 75$  nm (Table 3.1), is well described by a normal Fickian diffusion as in the free solution. The simulated results for the structural characteristics of these two i-opals denoted by the continuous solid lines in Figure 4.2 provide a good description of experimental data. For stronger confinement realized with the iO130-9/11 i-opal, the experimental  $G(t)$  for the QD deviates from a single Fickian diffusion which, however, nicely holds for the molecular T1.3 tracer. For this i-opal,  $G(t)$  for the QDs can be best fitted by a single non-Fickian process [118] taking into account the blinking effect (see Appendix C.3). The exponent  $\chi < 1$  in Eq. (C.4) denotes a sub-diffusional behavior for the mean-square displacement, and is plotted in Figure 4.2.

The deviation from the simple Fickian diffusion increases with  $a/R$  and the dynamic frustration is manifested in the enhanced reduction of the particle diffusivity as seen in Figure 4.2. The simulations can capture this strong slowing down using the same particle-wall interactions but adjusting the geometrical confinement, *i.e.* decreasing the ratio  $L/R$  by about 10% from 9/11 to 8/11. As a matter of fact, the simulations can also capture this strong slowing down at the experimentally assessed value of  $L/R = 9/11$ , but allowing for a stronger repulsion with the wall of T9.8 than for the other two i-opals.

The nature of the diffusive process is, as mentioned above, characterized by the exponent  $\chi$  in  $\langle \Delta \mathbf{r}^2(t) \rangle \sim t^\chi$ ; whereas  $\chi = 1$  characterizes the usual, Fickian diffusion, the cases  $\chi < 1$  ( $\chi > 1$ ) correspond to subdiffusive (superdiffusive) behavior [119, 120]. The key in determining the value of the exponent  $\chi$  above lies in the form of the probability distribution function  $p(\tau_{\text{esc}})$  of the escape time  $\tau_{\text{esc}}$  from a cavity of size  $R$ . Indeed, the total time  $t$

is the sum of a large number of independent and identically distributed random variables  $\tau_{\text{esc}}$ ; the asymptotic behavior of  $p(\tau_{\text{esc}})$  for large values of its argument determines then the stable distribution of their sum. In particular, subdiffusive behavior will result if  $p(\tau_{\text{esc}})$  has a power-law tail of the form [121, 122]:

$$p(\tau_{\text{esc}}) = \frac{t_0^\alpha}{\tau_{\text{esc}}^{1-\alpha}}, \quad (4.4)$$

with an arbitrary time constant  $t_0$  and  $\alpha \in (0, 1)$ . On the contrary, any probability distribution that decays to zero faster than that of Eq. (4.4) above as  $\tau_{\text{esc}} \rightarrow \infty$ , will lead to normal diffusion, *i.e.*  $\chi = 1$ .

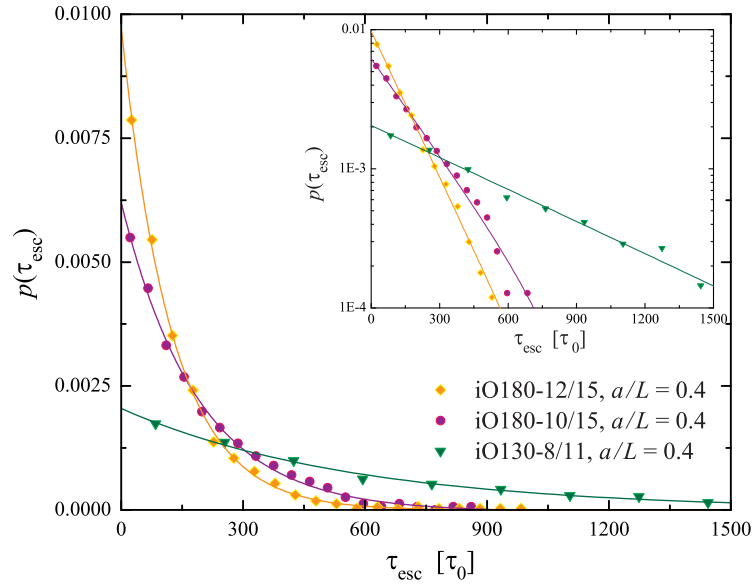


Figure 4.3.: The probability distribution  $p(\tau_{\text{esc}})$  of the escape times  $\tau_{\text{esc}}$  as obtained in the Brownian dynamics simulations for three different combinations of system parameters (points). Also shown are the fits by decaying, single exponentials, Eq. (4.5) (lines). Inset: semi-logarithmic plot, emphasizing the quality of the fit for large values of the abscissa.

Computer simulations offer the possibility to measure the probability distribution  $p(\tau_{\text{esc}})$  by performing statistics on the escape time from the cavity. We have done so for all parameter combinations studied in our system and we show representative results in Figure 4.3. As can be seen there, the distribution is *exponentially decaying* and can be very well fitted with the functional form:

$$p(\tau_{\text{esc}}) = \frac{1}{\tau_c} \exp\left(-\frac{\tau_{\text{esc}}}{\tau_c}\right), \quad (4.5)$$

with a characteristic time constant  $\tau_c$  that depends on the parameters  $L/R$  and  $a/L$ , and thus



sets the characteristic escape time from the cavity. This functional form can be understood when the escape processes are considered as a sequence of independent yes/no (*i.e.* escape/no escape) random trials, each of which yields success with probability  $p^*$ . Due to the high symmetry of our system, the probability  $p^*$  is approximately proportional to the ratio between the penetrable area and the surface area of the void. In the limiting case of  $a \rightarrow L/2$ ,  $p^*$  becomes very small and the diffusion through the i-opals can be regarded as a *Poisson process*, *i.e.* a stochastic counting process of single, rare, events which occur random in time. The corresponding probability distribution is characterized by an exponential decay [*c.f.* Eq. (4.5)], and describes for instance the decay of radioactive isotopes [123, 124].

i-opals and tracer particles	$\langle \tau_{\text{esc}} \rangle [\tau_0]$	$\tau_c [\tau_0]$
iO130-8/11, $a/L = 0.4$	$573.2 \pm 32.9$	$568.4 \pm 20.7$
iO180-10/15, $a/L = 0.4$	$182.3 \pm 9.0$	$188.0 \pm 5.3$
iO180-12/15, $a/L = 0.4$	$130.2 \pm 7.6$	$124.6 \pm 2.4$

Table 4.1.: The waiting times for a confined tracer particle. The first column shows the characteristic parameters of the i-opal (physical system), the second the expectation value of the escape time  $\tau_{\text{esc}}$  as obtained from the simulation and the third the value of the corresponding time constant  $\tau_c$ , obtained by fitting the distribution  $p(\tau_{\text{esc}})$  with an exponential, Eq. (4.5) of the main text.

In Table 4.1, we summarize the results for three representative systems, and we show in particular the numerical values obtained for the expectation value of the escape time,  $\langle \tau_{\text{esc}} \rangle$  obtained directly from the simulations, and for the time constant  $\tau_c$ , obtained from the representation of the data by Eq. (4.5); due to uncertainties in the numerical experiment, both quantities carry error bars. For a random variable  $\tau_{\text{esc}}$  following the distribution of Eq. (4.5), the equality  $\langle \tau_{\text{esc}} \rangle = \tau_c$  should hold. A comparison between the values in the second and third columns of Table 4.1 shows that, within error bars, this equality is indeed well-satisfied. There is thus overwhelming evidence from simulation that the distribution of escape times is indeed decaying to zero much faster than the family of distributions of Eq. (4.4) (which imply  $\chi < 1$ ), and thus the diffusion process in the regular, periodic i-opal should be normal, Fickian diffusion with an exponent  $\chi = 1$ .

Though this is in agreement with experiment for all other cases of tracer particles and confining structures, there is a discrepancy with the observed anomalous diffusion experiment for the most confined case of QDs in iO130-9/11 i-opal. We believe that the subdiffusive exponent measured in the experiments for the last case is only an apparent one and that the process is strictly diffusive. The reason for the appearance of an exponent  $\chi < 1$  (which, in addition, seems also to depend on the tracer size) probably lies in the presence of at



least two simultaneous diffusion processes, a faster and a slower one, caused by inevitable polydispersity in the opening size  $L$ . Indeed, as long as the particle radius is much smaller than the opening, through which escape from the cavity takes place, polydispersity should not have any measurable effect. However, as the limit  $a \rightarrow L/2$  is approached from below, any polydispersity in the opening size can have drastic effects, since the escape time grows very fast (see Figure 4.2) and eventually diverges at  $a = L/2$ . Tight confinement and tracer-wall interactions realized in mesoporous silica channel systems render the structure of the molecule trajectories very heterogeneous as was recently revealed by wide-field fluorescence microscopy [85]. The assumption, therefore, of the existence of two subprocesses, a fast and a slow one, caused by polydispersity, which gives rise to an apparent subdiffusive behavior at intermediate times, is supported by the fact that the phenomenon becomes visible only for large values of the tracer size. Evidently, normal diffusion should settle-in at sufficiently long observation times. An alternative explanation would be the existence of attractive patches (“trapping sites”) within the cavities of the i-opal, in which tracer particles occasionally reside for long times. However, such an effect should also be visible in the diffusive behavior for small radii, which is not the case. Therefore, the polydispersity scenario is the most realistic assumption for the explanation of the apparent  $\chi < 1$  exponent.

## 4.2. Flow Induced Polymer Translocation through Narrow and Patterned Channels

### 4.2.1. Theory of Injection Thresholds

This part of the thesis is mainly concerned with injection of dendrimers in narrow channels, whereby we will be making systematic comparisons with *linear* polymers as well, to establish the salient similarities and differences between the two. The lateral opening (width  $D$ ) of the channel will be thereby of the order of the dendrimer size, the latter being typically quantified *via* the radius of gyration  $R_G$ . Whereas for widths considerably larger than the dendrimer size its transport through the channel is guaranteed, the same is not true if  $D < R_G$ . Here, we anticipate the existence of a threshold for the current, below which no translocation takes place. In the following, we estimate this value and we establish that it is independent of the dendrimer’s degree of polymerization. We limit ourselves to low-generation dendrimers ( $G = 2 - 4$ ), which can be described as “compact objects”.

We commence with a short summary of known results about the (flow) injection of fractal and deformable objects, such as polymers, into narrow channels: Di Marzio and Mandell showed, within the framework of a simplified model, that a first-order translocation phase

transition occurs for chains when  $N \rightarrow \infty$  [125]. An issue that has been discussed at great lengths within the context of translocation is the scaling of the passage time through the hole, and its dependence on  $N$  and the external fields imposed on the setup. Different theories and approaches have been put forward. Computer simulations by Milchev *et al.* [109] confirm the prediction of Chuang *et al.* [126] that the translocation dynamics of self-avoiding chains is anomalous, with the passage time scaling as  $\sim N^{2\nu+1}$  ( $\nu \cong 0.59$  is the Flory exponent for self-avoiding chains) below the adsorption threshold and as  $\sim N^{1.65}$  above it. The case of unbiased translocation has also been recently studied by simulations [127]. A closely related problem is the escape of a polymer chain through a long channel, for which the driving force can be either a chemical potential imbalance [112, 113] or, as in the present work, solvent flow.

Generally, a flexible linear polymer in a dilute solution enters a pore of diameter  $D < R_G$  only when it is pushed into the narrowing by a solvent flux  $J$  that exceeds a certain threshold value  $J_c$ . Here, the flux  $J$  is the total current, defined as the volume of solvent passing through a cross-section of the channel in the unit of time. The value of the threshold flux,  $J_c$ , has been derived for *linear* and for *randomly branched* polymers in Ref. [128] by using Flory-type scaling arguments, based on the blob model for polymers [129], with the result:

$$J_c \simeq \frac{k_B T}{\eta}. \quad (4.6)$$

This finding is quite surprising, since it is, completely *independent* of the number of monomers  $N$  and the internal polymer structure.

In the following, we employ a similar approach in order to determine the injection threshold in the case of regularly branched polymers, *i.e.* dendrimers, where no simple blob model is applicable, because of their peculiar architecture and the ways their monomers order. In particular, it has been found by extensive simulations [130] that for low-generation dendrimers,  $G = 2 - 4$ , the size  $R_G$  scales with the number of monomers  $N$  as  $R_G \sim N^{1/3}$ . This is reminiscent of a compact object, akin, *e.g.*, to linear chains in a poor solvent, but the situation is more subtle because low-generation dendrimers are nevertheless soft and deformable [73, 131, 132]. At the same time, since there are clear steric limitations in an object for which the number of monomers grows exponentially with the generation number, there is no formal  $N \rightarrow \infty$ -limit for dendrimers, at least not for a spacer length of unity between successive generations. As a result, the gyration radius of low-generation dendrimers is of the same order as the monomer length, see Table 3.2 of this work and Ref. [130].

We aim at employing a Flory-type theory for dendrimers under flow, analogous to that put forward in Ref. [128] for randomly branched polymers, and which modified the original,

slightly flawed arguments presented in Refs. [133] and [134]. The first task thereby is to formulate the form of the theory for dendrimers in the *bulk*. Here, the problem already arises that if one follows the standard route and writes down an elastic term of the form  $\sim k_B T R^2 / R_0^2$ ,  $R_0 \sim \ln N$  being the ideal dendrimer size, the aforementioned correct scaling  $R_G \sim N^{1/3}$  for low-generation dendrimers does *not* come out. Therefore, we follow a heuristic modification: instead of using the ideal dendrimer size,  $R_0$ , in the denominator of the elastic contribution, we introduce an arbitrary length scale  $R_x$ , which scales as  $R_x \sim N^x$ , with an as of yet undetermined exponent  $x$ . Accordingly, we write a Flory-type reduced free energy as the sum of the elastic and excluded-volume terms as:

$$\beta F_{\text{Fl}}(R) = \frac{NR^2}{R_x^2} + \frac{N^2 a^3}{R^3}. \quad (4.7)$$

Notice the additional factor  $N$  in the elastic energy, which arises from the peculiar dendritic architecture and reflects the fact that a typical number of  $N$  chains are deformed when a dendrimer has linear size  $R$ . This  $N$ -factor plays a role analogous to the functionality  $f$  of  $f$ -armed star polymers. Minimization with respect to  $R$  yields  $R_G \sim N^{(1+2x)/5}$  and *requiring* that this relation reproduces the correct simulation result [130],  $R_G \sim N^{1/3}$ , yields  $x = 1/3$ . Alternatively, one could have argued that the first and second term on the right-hand side must have the same  $N$ -exponent when  $R \sim N^{1/3}$ , namely they must be a linear function of the degree of polymerization.

We now turn to the situation in which a dendrimer is pushed by a current  $J$  in front of the opening of a narrow channel of width  $D$ , schematically depicted in Figure 4.4. Note

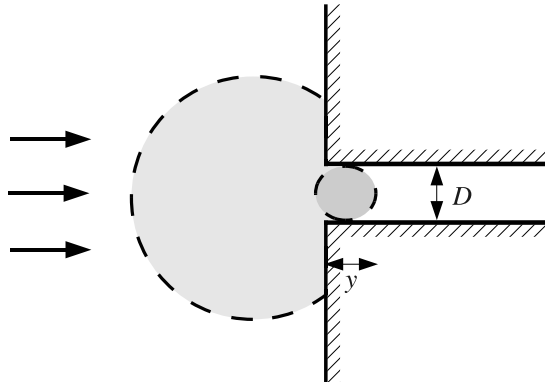


Figure 4.4.: A partly injected dendrimer inside a narrow channel with width  $D$ .

that since dendrimers are small objects, a hierarchy of length scales  $a \ll D \ll R_G$  is not possible and we rather have  $a \sim D < R_G$ . However, we will keep the discussion general in what follows and maintain both length scales,  $a$  and  $D$ , as independent parameters in

the scaling argument to follow. Under the conditions depicted in Figure 4.4, it can happen that the dendrimer only partially penetrates the channel, having a penetration length  $y$  and  $P < N$  of its monomers inside. Similarly to the approach in Ref. [128], we first estimate the dependence of  $y$  on  $P$  by writing down an expression for the free energy of the confined part in analogy with Eq. (4.7), *i.e.*:

$$\beta F(y) = \frac{y^2}{R_x^2(P)} + \frac{P^2 a^3}{y D^2}, \quad (4.8)$$

where  $R_x(P) \sim P^{1/3}$ . In comparing Eq. (4.8) with Eq. (4.7), note the absence of an additional factor  $P$  in the elastic energy of the former, since we anticipate that only a few monomers are confined in the partially injected state and thus there is no reason to believe that  $P$  chains are compressed. Minimizing Eq. (4.8) with respect to  $y$  we obtain the scaling relation:

$$\frac{y}{D} \simeq \left(\frac{a}{D}\right)^{5/3} P^{8/9}. \quad (4.9)$$

The specific volume  $\xi^3(y)$  available to each of the  $P$  confined monomers is given by the space-filling condition:

$$\frac{a^3}{\xi^3(y)} = \frac{P a^3}{y D^2}. \quad (4.10)$$

Using Eqs. (4.9) and (4.10), we readily obtain:

$$\xi(y) = y^{1/3} D^{2/3} P^{-1/3} = a \left(\frac{D}{a}\right)^{3/8} \left(\frac{D}{y}\right)^{1/24}. \quad (4.11)$$

It follows that  $\xi(y)$  has a slow decrease as  $y$  grows. Within the confined part, there exist  $yD^2/\xi^3(y)$  monomer blobs, each of which can be assigned a free energy cost of  $k_B T$ . Counteracting to it there is a hydrodynamic contribution from the drag of the flowing solvent, resulting in the total free energy  $\mathcal{F}(y)$  that has the form:

$$\mathcal{F}(y) = \mathcal{F}_{\text{conf}}(y) + \mathcal{F}_{\text{hyd}}(y) \quad (4.12)$$

$$= k_B T \frac{y D^2}{\xi^3(y)} - \int_0^y f_{\text{hyd}}(y') dy', \quad (4.13)$$

with the hydrodynamic force  $f_{\text{hyd}}$  being expressed as a Stokes drag per monomer, yielding:

$$f_{\text{hyd}}(y) \simeq \eta \xi(y) v(D) \frac{y D^2}{\xi^3(y)}, \quad (4.14)$$

where  $v(D) = J/(\pi D^2)$  is the local solvent velocity. Introducing the expression (4.11) above

and carrying out the algebra, we obtain the scaling laws:

$$\mathcal{F}_{\text{conf}}(y) \cong k_{\text{B}}T a^{-15/8} D^{3/4} y^{9/8}, \quad (4.15)$$

and:

$$\mathcal{F}_{\text{hyd}}(y) \cong -\eta J a^{-5/4} D^{-5/6} y^{25/12}. \quad (4.16)$$

Evidently, the sum of Eqs. (4.15) and (4.16), seen as a function of the confinement length  $y$ , initially grows with  $y$ , since  $\mathcal{F}_{\text{conf}}$  dominates for small  $y$ -values, but eventually drops because  $\mathcal{F}_{\text{hyd}}$  takes over for large  $y$  values. The total curve has a maximum at the position  $y^*$  and the value  $\mathcal{F}(y^*)$  corresponds thereby to a ‘‘suction free energy barrier’’ that must be overcome before the whole of the molecule is inserted into the channel. From Eqs. (4.15) and (4.16) the value  $y^*$  is easily calculated as:

$$y^* \cong \left( \frac{k_{\text{B}}T}{\eta J} \right)^{24/23} D \left( \frac{D}{a} \right)^{15/23}. \quad (4.17)$$

The resulting free energy barrier height reads as:

$$\beta \mathcal{F}(y^*) \cong \left( \frac{k_{\text{B}}T}{\eta J} \right)^{27/23} \left( \frac{D}{a} \right)^{60/23}. \quad (4.18)$$

Suction occurs when the barrier height is of order of the thermal energy  $k_{\text{B}}T$ , thus setting  $\beta \mathcal{F}(y^*) \cong 1$  in Eq. (4.18) above, we obtain the critical suction current  $J_c$  as:

$$J_c \cong \frac{k_{\text{B}}T}{\eta} \left( \frac{D}{a} \right)^{20/9} \cong \frac{k_{\text{B}}T}{\eta}, \quad (4.19)$$

the last equality following from the aforementioned fact that  $D \cong a$ . Thus, similarly to linear and randomly branched polymers, we find that also for dendrimers the critical current is *independent* of the degree of polymerization, a result that has been confirmed in our simulations, see Section 4.2.2 below. However, and in contrast to those two other polymer classes, the penetration length  $y^*$  at  $J = J_c$  is of order  $a$  and, according to Eq. (4.9), the number of sucked monomers there is of order unity. Due to the dendrimer architecture, a state in which a subcritical current causes a significant part of the molecule to be within the channel, whereas the rest remains outside, is not feasible for dendrimers: suction of a few monomers is sufficient to deform the whole molecule accordingly and to bring about injection of the same in the channel.

The small value of the critical penetration length  $y^*$  is a peculiarity of the dendritic architecture and the compact character of the molecule. Indeed, squeezing a few (terminal)

monomers of the dendrimers within the channel has the effect of “flattening” a part of the dendrimer lying outside the channel as well, so that most of the molecule is already deformed and can be pushed into the channel. The same property lies in the heart of the apparent paradox that  $J_c$  grows with  $D$ , see Eq. (4.19) above. To understand this, it must be noted that, according to Eq. (4.17), the critical penetration length  $y^*$  grows with  $D$  as well, so that the *same* penetration for a *wider* channel causes less deformation of the molecule and thus its shape is not suited to suction. A *stronger* current is thus needed to push part of the molecule in the channel and to cause significant deformation to the remaining part outside the channel, so that the latter can get squeezed into the pore as well. However, these findings are only valid for low generation dendrimers with spacer lengths equal to one. For dendrimers of higher generation and/or larger spacer lengths, we do not expect these arguments to hold anymore, and it is possible that  $J_c$  will then depend on details of the molecular architecture.

### 4.2.2. Comparison between Theory and Simulation

We begin with the question regarding the critical current  $J_c$ , with the purpose of checking the main finding of the theoretical approach, Section 4.2.1, stating that  $J_c$  is independent of the molecular weight. For this purpose, we have conducted a series of simulations for a given total time and counted the fraction of instances for which the molecules passed through. We carried out all simulations in a cubic box of volume  $V = 30 \times 30 \times 110$ . Walls were placed in the gradient direction, while periodic boundary conditions were applied in the flow and vorticity direction. Additionally, we separated the system *via* a slit-like channel of length  $L$  and diameter  $D$ . The temperature was set to  $T = 1.0$ , the solvent density to  $\rho_s = 5$ , and the size of the MPCD collision cell to  $a = \sigma$ . In Figure 4.5 we show the system geometry as well as the color-coded velocity-field in the flow-gradient plane. Here, both the no-slip boundary conditions along the channel walls and the parabolic shape of the profile in the center of the channel are clearly visible.

In Figure 4.6 we plot the translocation probability  $p_\ell(g)$  through a slit of width  $D = 2.0$ , as a function of the acceleration constant  $g$ , for linear polymers and dendrimers of various sizes. For each parameter set, we have performed 50 simulations of  $\ell = 10^7$  time steps. The results in Figure 4.6(a) pertain to linear polymers and provide an independent confirmation of similar findings by Markesteijn *et al.* [135], obtained by means of Lattice Boltzmann techniques, whereas results in Figure 4.6(b) refer to dendrimers. We see a smooth transition from  $p_\ell(g) = 0$  to  $p_\ell(g) = 1$  as  $g$  increases. At this point, we would like to emphasize that the continuous nature of  $p_\ell(g)$  is only due to the finite number of time steps in our simulation. Furthermore, we see that in both cases the probability is completely independent of  $N$ , which is in full agreement with previous results [128, 135] as well as our own theoretical

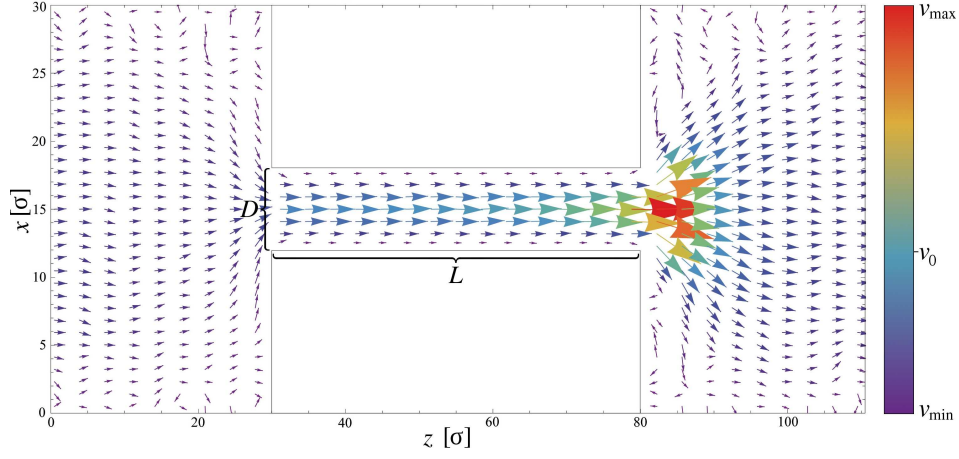


Figure 4.5.: Color-coded velocity-field profile in the flow-gradient plane in a system with  $L = 50.0$ ,  $D = 6.0$  and  $g = 0.05$ . The length of the arrows is proportional to the local speed of the solvent particles.

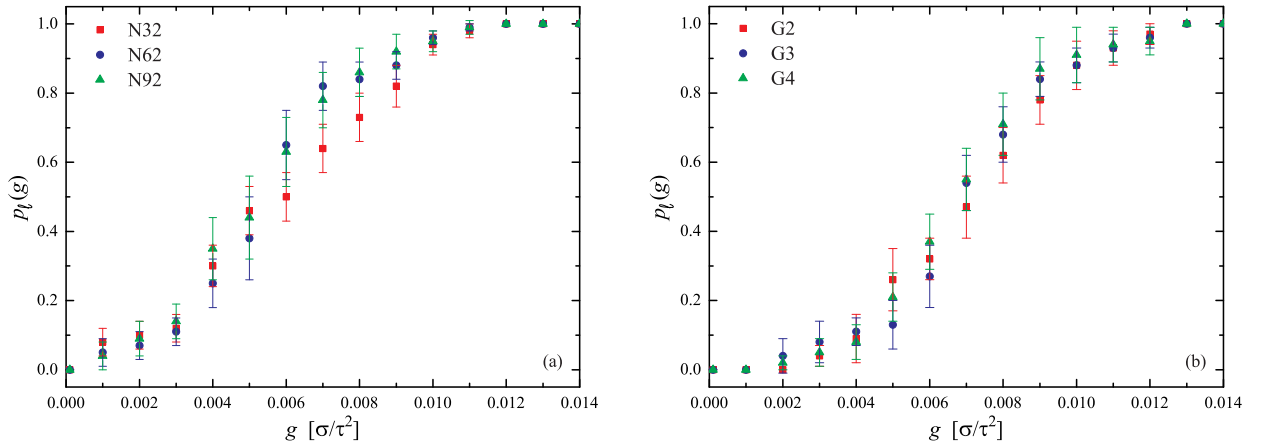


Figure 4.6.: Translocation probability  $p$  through a slit of width  $D = 2.0$  for polymer chains of different length (a) and dendrimers of different generation number (b).

prediction. When the results for linear polymers and dendrimers are compared, it is visible that the threshold flux is slightly higher for dendrimers, which is due to their more compact structure. Furthermore, we suspect that  $J_c$  would become larger if the dendrimer's degrees of freedom were restricted by internal bond and torsion angles. However, once the molecule is sucked into the channel, the increased rigidity of the polymer should accelerate its motion through the channel, thereby shortening the translocation times.

We now generalize the discussion to consider channel widths  $D$  that are both smaller and slightly larger than the dendrimer size. Once the macromolecule has entered the channel, the main quantity of interest is the translocation time  $\tau^*$ , *i.e.* the time needed for the polymer to traverse the channel. In Figure 4.7 we show  $\tau^*$  as a function of the channel width  $D$  for both linear and regularly branched polymers; the simulation has been performed at  $g = 0.05$  and averaged over 50 runs. When the translocation time of the whole molecule is considered, *i.e.*

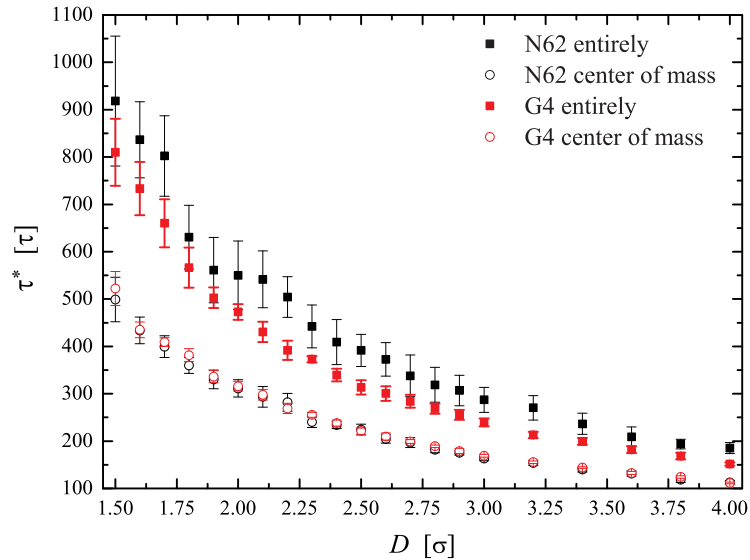


Figure 4.7.: Translocation time  $\tau^*$  of a linear polymer and a G4-dendrimer with each  $N = 62$  beads as a function of the channel width  $D$ . The simulation has been carried out at  $g = 0.05$  for a channel of length  $L = 30.0$ .

the time span between the entry of the first bead and the exit of the last bead, dendrimers have a slightly smaller passage time. This is again due to their rather compact structure, whereas linear polymers can be stretched rather easily in the flow direction, and hence more time is needed until all monomers have passed through the narrowing. However, these differences vanish completely when the center of mass is considered instead of the whole polymer. To better analyze the differences between linear polymers and dendritic structures, it is useful to have a look at their individual flow behavior through the narrowing. In Figure 4.8 we



show the position of the polymer's center of mass in flow direction  $z$  as a function of time  $t$  for channels of length  $L = 30$  and various widths  $D$ . Since we are mainly interested in the impact of the confinement, we only plot the regime between channel start ( $z = 40$ ) and channel end ( $z = 70$ ). The simulations have been performed at  $g = 0.05$  and each curve has been averaged over 25 measurements. Here it is well visible that, although the translocation

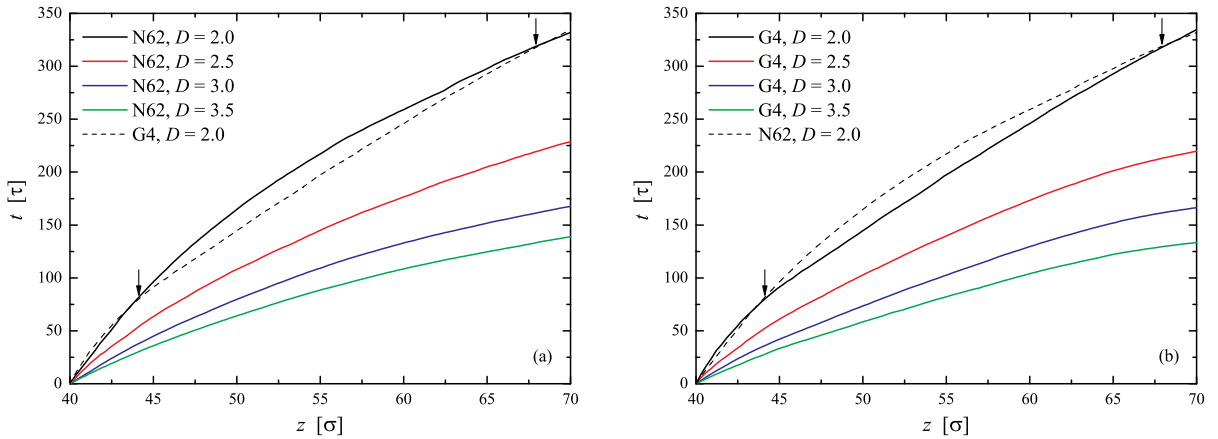


Figure 4.8.: The  $z$ -position of the center of mass inside a channel of length  $L = 30.0$  at  $g = 0.05$  for a polymer chain with 62 beads (a), and a dendrimer of fourth generation (b). For a better comparison, we have also included the  $z$ -position of the other macromolecule in the narrowest channel (dashed line). The arrows indicate the position where these two curves cross.

times  $\tau^*$  of linear and regularly branched polymers are almost identical, their detailed flow behavior is nevertheless quite different. Dendritic structures exhibit a much broader regime of ballistic propagation (translocation with constant speed) than chain polymers with the same monomer number  $N$ . The reason for this behavior is that, although the linear polymer's center of mass has already entered the channel, a significant part of the polymer is still outside the capillary and needs to be sucked in. This leads to an overall hindrance, which manifests itself in the lack of linear part in the curves  $t(z)$  for linear chains.

Turning our attention to the molecular deformations inside the channel, we have measured the diagonal components  $G_{\alpha\alpha}$  of the average gyration tensor, Eq. (3.6), as a function of the channel width  $D$ . In this way, we can quantify the impact of the constriction on the polymer shape. Results of the simulation, with  $g = 0.05$  and  $L = 80.0$ , are shown in Figure 4.9. Surprisingly, even for large channel widths,  $D > 2R_G$ , neither  $G_{zz}$  nor  $G_{xx}$  approach the equilibrium (bulk) radius of gyration ( $R_G = 2.78 \pm 0.04$ ). Instead, the dendrimer becomes elongated along the  $z$ -axis by a factor of approximately 1.5 and subsequently shrinks in  $x$ -direction by about the same factor. This deformation is due to the two-dimensional parabolic

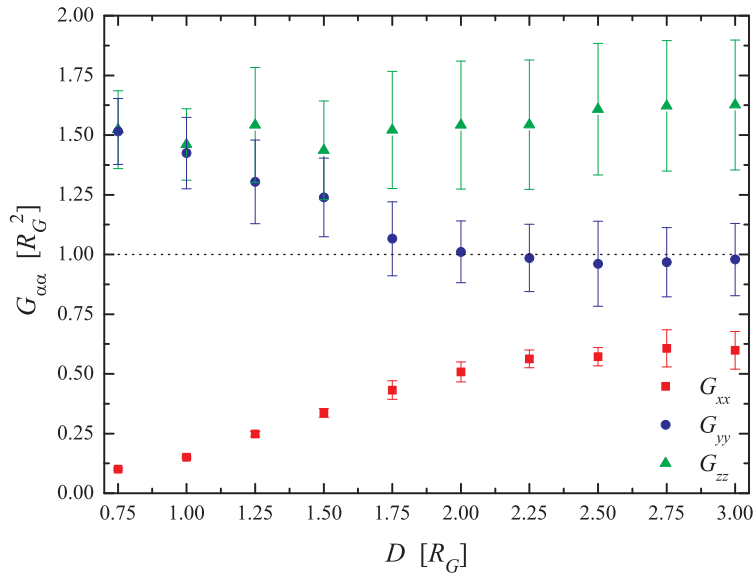


Figure 4.9.: Diagonal components  $G_{\alpha\alpha}$  of the average gyration tensor as a function of the channel width  $D$  for a G4-dendrimer with  $N = 62$  beads. The simulation has been carried out at  $g = 0.05$  for a channel of length  $L = 80.0$ .

flow profile of the solvent, and as a first approximation, the solvent flow can be considered as a superposition of two opposite shear flows, which act on the polymer. In such systems, deformation has been observed both for dendrimers [44] and other soft macromolecules [42, 136]. For linear polymers, such an analysis is less interesting, since they are stretched rather easily along the flow direction and almost reach their maximum extension.

Consistently with the above discussion, we have observed in our simulations that the polymer flows equidistant to both channel walls, where it is also exposed to the strongest fluid current. This centering is due to the hydrodynamic interactions mediated by the solvent and has been already observed in previous simulations [137]. By adding an attractive part to the wall potential, *i.e.* turning into the case  $\lambda_w = 1.0$ , one could expect that it is possible to “drag” the polymers towards the channel walls and thereby slow down their motion (translocation) inside the channel, since the fluid velocity is much smaller in the vicinity of the channel walls. In Figure 4.10, we show the translocation time  $\tau^*$  of a polymer chain in the case of purely repulsive, and partly attractive walls. Although a small retardation is measurable, the impact is far from being significant in the case of linear polymers and almost nonexistent for dendrimers. Details of the wall-monomer interactions seem to be immaterial, at least as long as the walls are smooth.

Real walls on the other hand are rarely smooth and at the nanoscale atomic details become relevant. Of particular interest in this work is the possibility to decorate the walls with

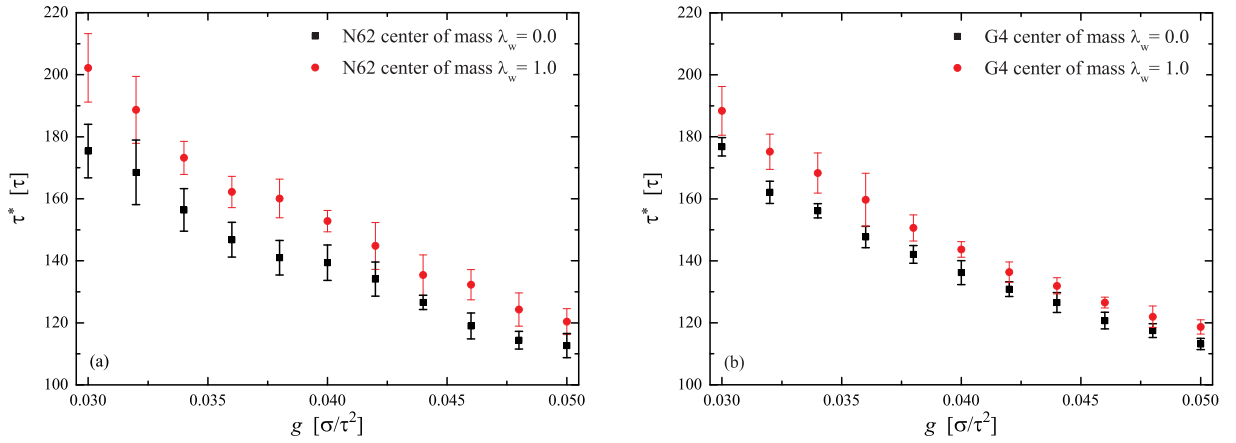


Figure 4.10.: Translocation time of a linear polymer (a), and a G4-dendrimer (b) with each  $N = 62$  beads as a function of  $g$ . The simulation has been carried out for a channel of width  $D = 4.0$  and length  $L = 30.0$ .

attractive patches. This can be achieved either with chemical patterning of the walls or, more importantly, through insertions of suitable entities, such as peptides intruding rigid bilayer membranes, as demonstrated in the recent work of Smith *et al.* [138]. Accordingly, instead of a homogeneous attraction, we cover the channel walls with  $N_p$  line-like, highly attractive patches. In Figure 4.11 we show the color-coded potential landscape both in the simple, purely repulsive case, and in the case of repulsive walls covered with the line shaped patches. The patches could model “docking sites” at which a dendrimer should temporarily reside, with the purpose of delivering an encapsulated cargo at the appropriate place, whereas the solvent (blood) flow should carry away the remaining molecule at longer times.

Due to the discontinuous shape of the potential, its gradient leads to a non-zero contribution in the flow-direction, which results in a severe sticking of the polymers. This is especially evident in the case of linear polymers, where the polymer almost completely aligns against one channel wall and thus only experiences a very weak solvent flow, see Figure 4.12. Dendrimers on the other hand cannot flatten entirely against one channel wall; instead, the extremities gravitate towards the patches, while the core of the polymer remains in the channel center. Eventually one arm detaches from its patch, hence releasing the whole polymer. Then the whole macromolecule moves a bit further inside the channel, until it approaches the next patch and the whole process repeats itself. This procedure is well-visible on the basis of the plateaus in Figure 4.12, where the position of the dendrimer’s center of mass is plotted against the time. These findings are remarkable, since now, in contrast to the case of homogeneously attractive walls, the retardation is highly dependent on the shape of the polymers. Hence, such a setup can be used to separate dilute linear/dendritic polymer

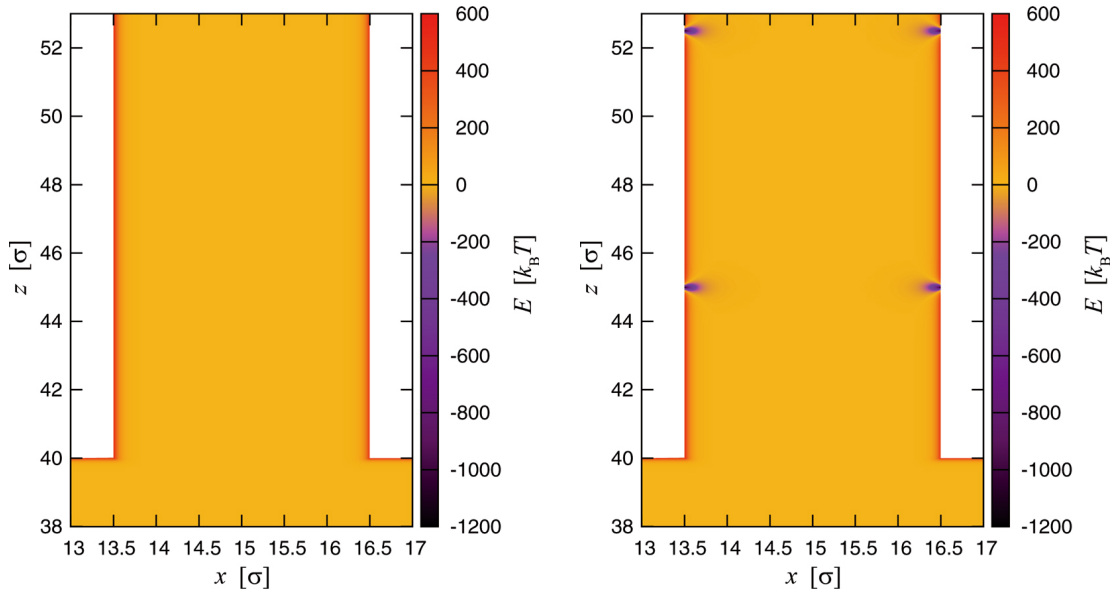


Figure 4.11.: Color-coded potential landscape in the flow-gradient plane close by the channel entrance. Purely repulsive walls (a), and repulsive walls covered with highly attractive patches (b). The extension of the line shaped patches is along the  $y$ -axis.

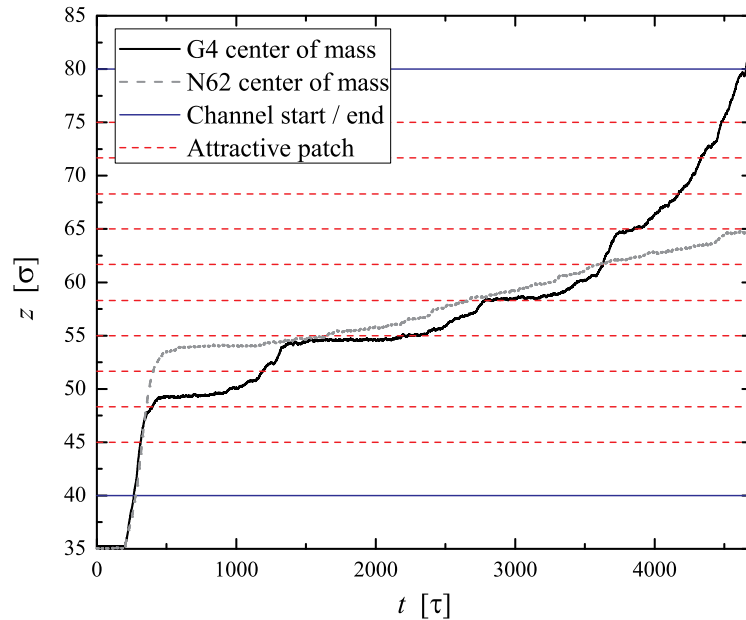


Figure 4.12.: Spatiotemporal evolution of a N62-linear polymer's (grey, dotted line), and a G4-dendrimer's (black, solid line) center of mass in a channel with  $L = 40.0$  and  $D = 6.0$  with  $N_p = 10$  attractive patches at  $g = 0.015$ .

mixtures. We also note that, although the results presented here pertain to both walls being decorated with the same patches that face each other, they remain essentially unchanged also in the case of a single patterned wall.

Finally, to quantify this retardation effect more thoroughly, we measured the translocation time  $\tau_p$  in the presence of patches for two channels of different widths ( $D = 4.0 < 2R_G$  and  $D = 6.0 > 2R_G$ ), and derived the slowdown in the translocation of the polymers compared to the case of purely repulsive walls. The results are plotted as a function of  $N_p$  and are shown in Figure 4.13. A quite remarkable slowdown is evident in both cases, where in the more narrow channel a retardation by two orders of magnitude can be achieved for the case of  $N_p = 20$  patches. The relevance of the channel width  $D$  is due to the rather short-ranged nature of the patch potential, therefore the broader the channel, the less important the presence of patches on the channel walls. Concerning the interpatch spacing, we have shown that the impact of the sticky patches vanishes for the both extreme cases  $L/N_p \rightarrow 0$  (smooth walls) and  $L/N_p \rightarrow \infty$  (no patches). We therefore expect that the translocation time is maximal when the interpatch spacing is of the order of the dendrimer size, since this configuration allows the dendrimer to dock on one patch, while at the same time a few monomer can dock on neighboring patches.

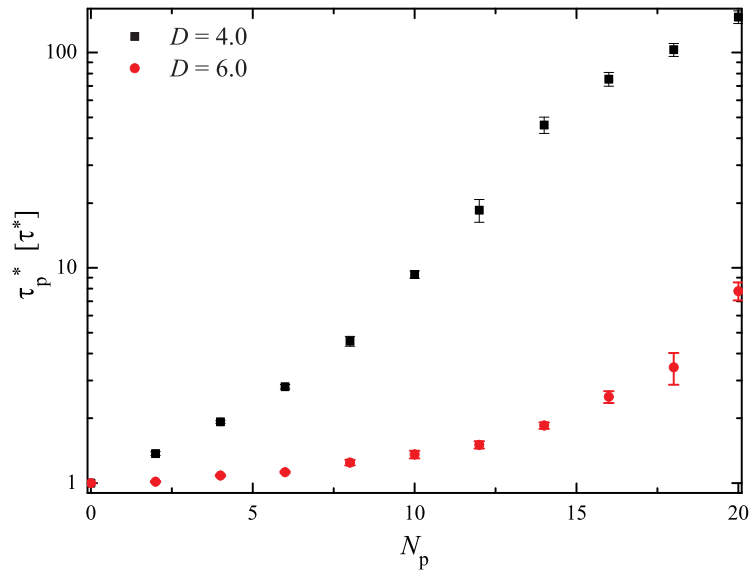


Figure 4.13.: Slowdown factor of a G4-dendrimer in a channel of length  $L = 40.0$  at  $g = 0.05$ , plotted against the number of attractive patches  $N_p$ .



# 5. Flow Properties of Cluster Crystals

Complex, non-Newtonian fluids demonstrate an enormously rich rheological behavior under shear and pressure driven flow, which leads to a variety of non-equilibrium structures. This non-linearity makes complex fluids extremely challenging to understand from the fundamental point of view. They show shear-banding [12], thixotropy [13], shear-thinning [14, 15] as well as, in many cases, shear-thickening [14]. In addition, these materials bear high importance for a wide variety of applications in, *e.g.*, nanotechnology and micropatterning [17], microfluidics [18], or shock absorption [19].

Shear often acts in a way that suppresses spatial order: shearing a crystal can gradually reduce the three-dimensional periodicity of the same, bringing about a *shear-induced disorder* (SID) transition to a uniform phase. The topic has attracted a great deal of attention also in the context of atomic systems [139], aiming at understanding the sequence of states that lead from an equilibrium crystal at zero shear, to a shear-molten state at high shear. The hitherto explored scenarios on the succession of steady-states at increasing shear are dependent on the type of inter-particle interactions, on crystal orientation in the cell, on concentration and, for the case of charge-stabilized colloids, on salinity. Ackerson *et al.* [140–142] have performed a combination of shear and SANS measurements on charge-stabilized colloids both for body centered cubic (bcc) and for face centered cubic (fcc) lattices. The generic scheme under which the SID comes about is a succession, with increasing shear-rate, proceeding from the equilibrium crystal to a strained solid in which either twin bcc or zig-zag motions of successive close packed planes are observed, to a sliding layer structure with two-dimensional order, and finally to a fluid [143]. Subsequent experiments have confirmed the salient features of this scenario, both for charged colloids [144–148] and for hard spheres [149–151]. A particularly intriguing finding of the experimental investigations on charged colloids is the emergence of short stringlike correlations between the colloids close to the SID-transitions without spatial ordering of the same [140, 145]. Butler and Harowell [152] found in their simulations of Yukawa crystals that, although these strings had no particular correlation in the flow-vorticity plane, they showed hexagonal order in the gradient-vorticity plane.

On the other hand, steady shear can have the opposite effects on thermodynamically metastable fluids. The latter are uniform phases that are separated by their equilibrium, crystalline phase by a sufficiently high nucleation barrier, so that they either remain super-cooled for macroscopically long times or get trapped into a glassy state. A characteristic example is the dynamical arrest of soft colloids, such as star polymers or star-like micelles

[153–157], which takes place in regions of the phase diagram that correspond to an equilibrium fcc crystal. Shear can induce three-dimensional periodicity to such a supercooled or arrested solution, accelerating thereby the nucleation rates in metastable liquids after the cessation of shear. This shear-induced crystallization has been demonstrated convincingly for soft colloids, and in particular for block copolymer micelles, in the seminal work of Mortensen, Brown, and Nordén [158].

In addition to shear, another prominent prototype of non-equilibrium processes is transport flow along channels, driven by a pressure gradient. Here, complex fluids are of particular technological importance because the control of their flow properties has numerous applications. Characteristic examples are the directed assembly of mesoscale periodic structures [159–162], the controlled synthesis and manipulation of monodisperse, soft colloidal particles [163–167], the measurement of the elastic properties of the same [168], as well as the manufacturing of specific nanofluidic devices such as nanopumps [169] or moving-wall channels [170]. On the more fundamental side, recent research activity has focused on the transport flow of colloidal gels [171–173] and of concentrated colloidal dispersions close to their jamming point [174–179], as well as on the related issue of flow and filtration of Brownian colloidal or non-Brownian, wet granular matter [180–183].

In this Chapter, we study the behavior of ultrasoft colloids under shear and transport flow. The interaction potential of these particles is *bounded*, thus allowing full and multiple particle overlap (see Section 3.3). First, we applied steady shear along the crystallographic [100] and [111] direction, and analyzed the phase behavior as a function of the shear-rate for various solute densities. Then in the second part of our analysis, we have studied the impact of Poiseuille flow by conducting a series of simulations for different occupation numbers  $N_C$ , crystallographic orientations and flow strengths.

## 5.1. Cluster Crystals under Shear

### 5.1.1. Shear-Induced String Formation

We considered an fcc cluster crystal, formed by clusters of overlapping particles which interact *via* the GEM-8 potential (see Section 3.3). This crystal is exposed to shear forces through parallel shearing walls that are parallel to the  $z$  (flow) direction, the  $x$ -axis being the gradient and the  $y$ -axis the vorticity directions. We carried out the simulations in a cubic simulation box, where the walls were separated by a distance of  $L_x = 11\sigma$  in the gradient direction. In addition, we applied periodic boundary conditions in the  $y$ - and  $z$ -direction, resulting in a slit-like channel geometry (see Chapter 2 for details of the simulation). The system was



sheared along the crystallographic [100] or along the [111] plane at temperature  $k_B T/\epsilon = 0.2$ . Thereby, the (100) surface is obtained by cutting the crystal parallel to the front surface of the fcc cubic unit cell, leading to an arrangement of four-fold symmetry; the (111) surface is obtained by slicing the crystal in such a way that the surface plane intersects the  $x$ -,  $y$ - and  $z$ -axes at the same value, resulting in a particle arrangement of six-fold symmetry (see Figure 5.1).

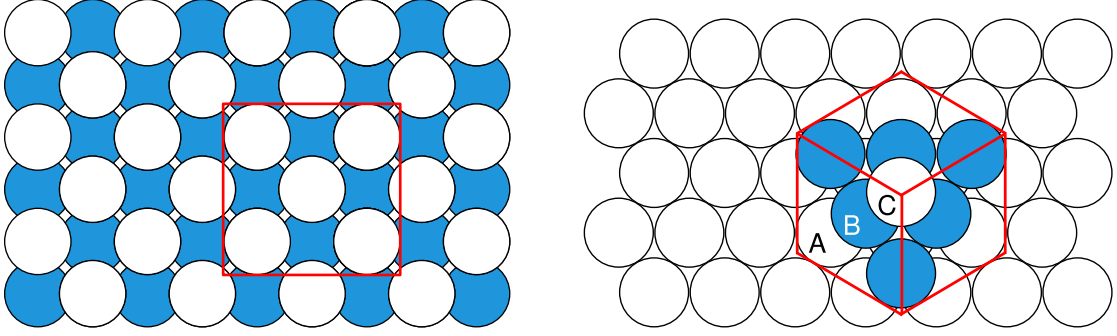


Figure 5.1.: Schematic representation of an face-centered cubic crystal's (100) (left panel), and (111) surface (right panel).

The system was investigated at three different state points with densities  $\rho = 2.6, 3.9,$  and  $5.9$  (corresponding to average cluster occupation numbers  $N_C = 4, 6,$  and  $9,$  respectively), while we kept the solvent density fixed at  $\rho_s = 30$  for all runs. Furthermore, the size of the MPCD collision cells was set to the particle diameter  $a = \sigma$  throughout. As shown in Figure 5.2, the system forms stable fcc cluster crystals in the (constrained) bulk phase at these state points [184].

As we exposed the system to the shearing forces, we found the following striking form of self-organization: within a certain range of shear-rate  $\dot{\gamma} \in [\dot{\gamma}_{\min}, \dot{\gamma}_c]$  (to be specified below), the cluster crystal transformed into an arrangement of parallel strings, which aligned in the flow direction and formed a two-dimensional hexagonal lattice in the gradient-vorticity plane. Along the strings, the particles displayed a disordered, liquid-like structure (see Figure 5.3). In Brownian dynamics simulations in which hydrodynamics were not taken into account, this string formation occurred for arbitrarily small  $\dot{\gamma}$ , whereas in the MPCD simulations, we obtained a nonlinear velocity profile and wall-slip (shear banding) for  $\dot{\gamma} < \dot{\gamma}_{\min} \cong 0.05$ , since the shear flow was shielded by the outer layers of the crystals.

Within the above specified range of shear-rates, the formation of strings was independent of the initial conditions, since it occurred both for ordered and for disordered starting configurations. More details about the transformation process were revealed by shearing with fixed  $\dot{\gamma}$  at the two different orientations of the crystal specified above: for shear along the [100]

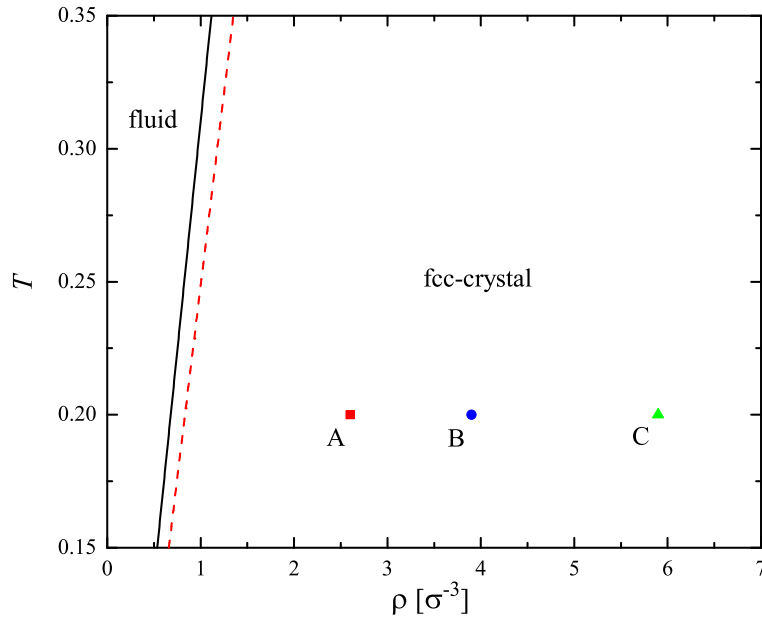


Figure 5.2.: The (constrained) bulk phase diagram for the GEM-8 particles in the  $(\rho, T)$ -plane [184]. Lines show the phase boundaries for the liquid (solid black) and the fcc phase (dashed red). The gap in-between denotes the coexistence region. Symbols show the investigated state points.

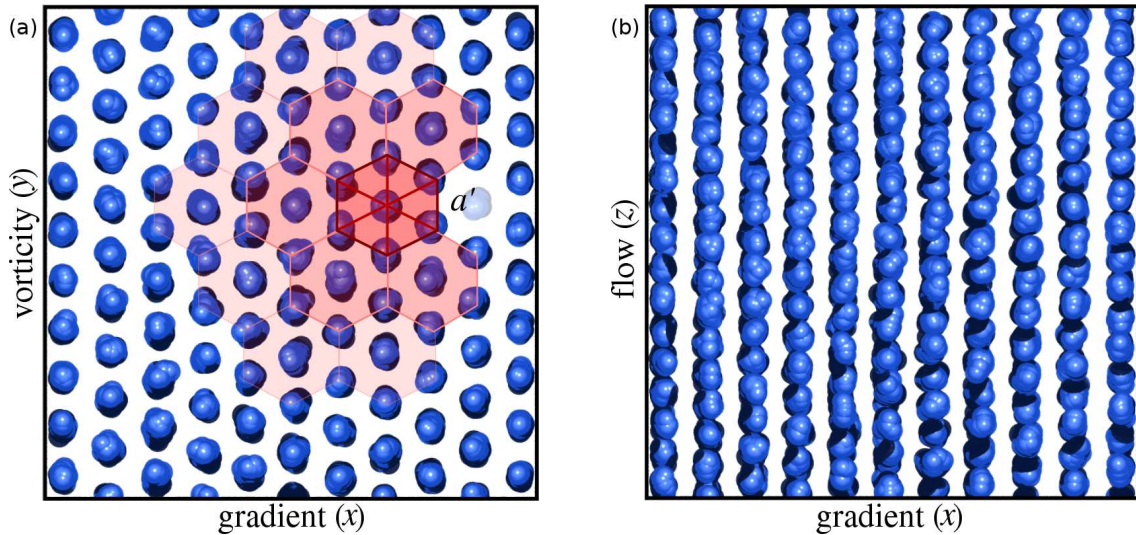


Figure 5.3.: (a) Vorticity-gradient and (b) flow-gradient views of the strings formed in a cluster crystal under shear with a shear-rate  $\dot{\gamma} \in [\dot{\gamma}_{\min}, \dot{\gamma}_c]$  (see text). Blue spheres (not drawn to scale) represent GEM particles. In (a), a few centers of mass of the strings are connected by straight lines, the red shading of the resulting hexagonal tiles reflects the distance from the arbitrarily chosen central string;  $a'$  is the lattice constant of the triangular lattice formed by the strings.

direction, the cluster crystal completely melted shortly after shear was applied. The melting process started from the center of the crystal and then expanded gradually towards the outer layers. Eventually, the strings formed out of this transient melt. When shearing along the [111] direction, the system took advantage of the fact that the ABC-stacking encountered in the cluster crystal is very similar to the final ordering of the strings, *c.f.* Figure 5.3(a). Thus, the crystal melted only along the (111) planes which, themselves, remained well-separated from each other during the entire process. The fact that the transformation process was “easier” in the latter case is reflected by the fact that the yield stress  $\sigma_0$  (see Table 5.1) is lower when shearing in the [111] direction.

$N_C$	$\sigma_0$ [ $\epsilon/\sigma^3$ ]	$\eta_1$ [ $\tau\epsilon/\sigma^3$ ]	$\eta_2$ [ $\tau\epsilon/\sigma^3$ ]	$\dot{\gamma}_{c,1}$ [ $\tau^{-1}$ ]	$\dot{\gamma}_{c,2}$ [ $\tau^{-1}$ ]
4 [100]	$7.60 \pm 0.13$	$32.12 \pm 0.41$	$39.81 \pm 0.44$	0.33	0.34
4 [111]	$7.51 \pm 0.12$	$30.94 \pm 0.42$	$40.32 \pm 0.34$	0.30	0.35
6 [100]	$10.81 \pm 0.27$	$40.32 \pm 0.68$	$50.97 \pm 0.56$	0.36	0.42
6 [111]	$8.49 \pm 0.31$	$39.86 \pm 0.53$	$50.67 \pm 0.51$	0.35	0.42
9 [100]	$16.30 \pm 0.26$	$50.13 \pm 0.68$	$69.70 \pm 0.77$	0.40	0.47
9 [111]	$11.04 \pm 0.14$	$49.60 \pm 0.73$	$66.98 \pm 0.93$	0.42	0.47

Table 5.1.: Simulation results from shearing of GEM-8 cluster crystals at  $T = 0.2$  for different cluster occupation numbers  $N_C$  and crystal orientations in the shear cell, indicated in the first column. Listed are the Bingham yield stress  $\sigma_0$ , and the shear viscosities  $\eta_1$  (of the string phase) and  $\eta_2$  (of the molten phase at high shear). The value  $\dot{\gamma}_{c,1}$  is an estimate for string-melting according to the Bingham plastic model, while  $\dot{\gamma}_{c,2}$  is obtained by identifying the minimum of  $d\Phi/d\dot{\gamma}$  (see text).

The formation of the strings, *i.e.* the loss of ordering *parallel* to the flow direction and the subsequent triangular ordering *perpendicular* to the flow direction can be understood as follows. The physical mechanism that stabilizes the GEM-particles in a three-dimensional crystal is self-sustaining: the restoring force for any particle towards a lattice site is provided by the neighboring clusters [82]. An applied shear distorts the clusters in the flow direction, reducing thereby the magnitude of the restoring force. Since this process is self-amplifying, a higher shear-rate distorts the clusters even more and reduces the restoring force concomitantly, leading to melting along the flow direction and clusters start to flow. This process is unique to penetrable colloids, since the presence of a hard core prohibits particle overlap. In the string phase, each particle separated from a string of line density  $\Lambda$  by a distance  $R$  experiences a repulsive potential:

$$U_{2d}(R) = \Lambda \int_{-\infty}^{\infty} U(r) dz. \quad (5.1)$$

The string-string interaction potential *per unit length* is then given by  $\Lambda U_{2d}(R)$ , which is a bounded repulsion in two dimensions. Applying the analysis of Ref. [82], we find that under their mutual repulsion, these strings now form a triangular crystal. For the case of the GEM-8 potential at hand, the inter-string potential has a Fourier transform with a negative minimum located at  $K_{\min}/k_{\min} \cong 1.28$ , where  $k_{\min}$  and  $K_{\min}$  are the locations of the minima of the Fourier transforms of  $U(r)$  and  $U_{2d}(R)$ , respectively. This implies that the lattice constant of the ensuing triangular crystal is smaller than that of the original fcc-crystal, a fact confirmed in our simulations by the emergence of additional layers of strings for shear in the [100]-direction.

If the shear-rate then exceeds the density-dependent critical value of  $\dot{\gamma}_c$ , the system melts and its shear viscosity  $\eta$  increases significantly (shear-thickening). Again, melting starts in the center of the simulation box. The underlying mechanism that is responsible for this melting process becomes evident from the MPCD simulations: for sufficiently high  $\dot{\gamma}$ -values, particles are able to overtake each other as they move along the strings, a phenomenon that is strongly supported by hydrodynamic interactions since a tagged particle can move in the wake of its preceding particle. Indeed, we have performed additional Brownian dynamics simulations, in which hydrodynamics were ignored (see Section 2.2), and we were not able to observe this shear-induced disorder transition for the range of shear-rates simulated. However, we expect it to take place at some higher shear-rate, since thermal fluctuations will eventually lead to a sufficiently large perturbation. In conjunction with the two-dimensional particle-string interaction  $U_{2d}(R) \propto \Lambda$ , we are able to estimate the critical shear-rate  $\dot{\gamma}_c$  as follows. The typical time scale  $t_{\perp}$  for any particle to deviate from the string in the *perpendicular* direction by a distance  $a$ , is:

$$t_{\perp} \cong 2\pi/\omega, \quad (5.2)$$

where  $\omega$  is the oscillation frequency due to the superposition of the potentials:

$$\sum_i U_{2d}(|\mathbf{R} - \mathbf{R}_i|), \quad (5.3)$$

$\{\mathbf{R}_i\}$  being the vectors of the (nearest) neighbors in the hexagonal lattice and  $a$  being the amplitude of the oscillations [82]. The corresponding time  $t_{\parallel}$  for a particle to move along the same distance *parallel* to the string, once it has been displaced from the string laterally by  $a$ , is thus given by:

$$t_{\parallel} \cong a/(a\dot{\gamma}) = \dot{\gamma}^{-1}. \quad (5.4)$$

As long as the shear-rate is sufficiently small and  $t_{\parallel} \gg t_{\perp}$  holds, shear does not destroy the strings. However, when  $t_{\parallel} \cong t_{\perp}$ , particles start overtaking and string correlations are

destroyed. Taking the above expressions for  $t_{\perp}$  and  $t_{\parallel}$ , we obtain the estimate  $\dot{\gamma}_c = \omega/(2\pi)$ . Furthermore, since  $\omega^2 \propto \Lambda \propto N_C$  holds [82], we finally get:

$$\dot{\gamma}_c = b\sqrt{N_C}, \quad (5.5)$$

where  $b$  is a numerical coefficient that depends on the detailed nature of  $U(r)$ . For the system at hand, this coefficient can be fitted to  $b = 0.18 \pm 0.04$ .

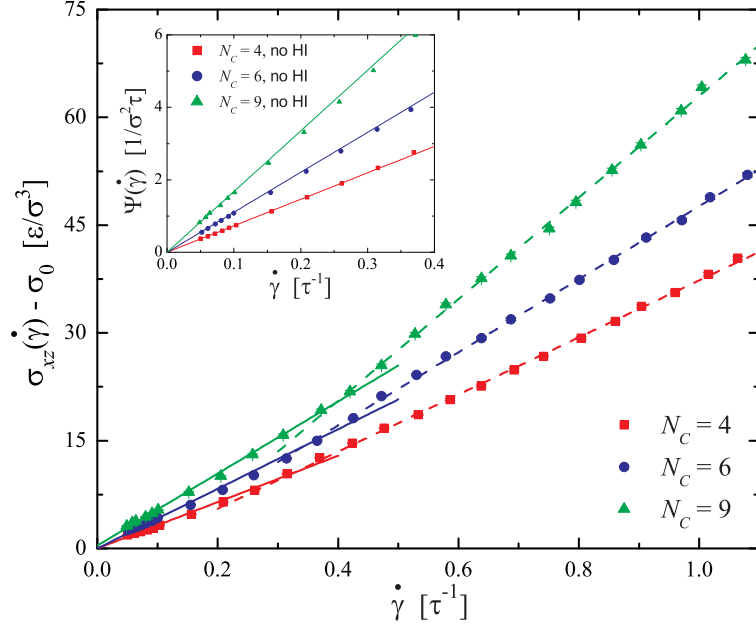


Figure 5.4.: Shear stress  $\sigma_{xz}(\dot{\gamma})$ , reduced by the yield stress  $\sigma_0$ , as obtained from the MPCD simulations, for shear at the [100]-orientation (symbols). The full lines (string state) and the dashed lines (molten state) are fits according to the Bingham plastic. The inset shows the flux  $\Psi(\dot{\gamma})$  of particles across the simulation box, as obtained from full MPCD (lines) and from BD without hydrodynamics (symbols).

From the simulations, the value of  $\dot{\gamma}_c$  can be estimated via two different routes: first, we employ a macroscopic Bingham plastic model describing a viscoplastic material that behaves as a rigid body at low stress but flows as a viscous fluid at high stress. Here, the shear stress  $\sigma_{xz}$  is given by :

$$\sigma_{xz}(\dot{\gamma}) = \eta\dot{\gamma} + \sigma_0, \quad (5.6)$$

$\eta$  being the shear viscosity and  $\sigma_0$  being the yield stress. Fitting our results to this model leads to the values for  $\sigma_0$  and  $\eta$  summarized in Table 5.1. Furthermore, from the intersection of the fitted curves in the two different regimes (see Figure 5.5), we obtain results for  $\dot{\gamma}_c$ . The approximate character of the model is reflected in the fact that the identified values for

$\dot{\gamma}_c$  differ markedly for different crystal orientations at the same  $N_C$ . Nevertheless, the model serves as a good indicator.

Second, we consider the free volume fraction  $\Phi(\dot{\gamma})$ , which decreases as the system melts out of the strings. During this transition, more particles are suddenly exposed to the flow, leading to a dramatic increase in the fluid resistance. This is a unique property of this cluster crystal, since usually the shear viscosity *drops* at shear melting. Here, we considered each GEM-particle as a sphere of diameter  $\sigma$  and calculated the free volume  $\Phi$  in each state by straightforward counting. Results are shown in Figure 5.5, which shows  $\Phi$  as a function of  $\dot{\gamma}$ . By identifying the minimum of  $d\Phi/d\dot{\gamma}$ , we obtain an additional estimate for  $\dot{\gamma}_c$  (see Table 5.1). We find remarkable agreement with the theoretical estimate of Eq. (5.5) above, *e.g.*, for  $N_C = 4$  we obtain  $\dot{\gamma}_c = 0.36$  (0.34) from theory (simulations), and the latter are consistent with the  $\dot{\gamma}_c \sim \sqrt{N_C}$ -scaling for the remaining  $N_C$  values. In the string-phase, the  $\Phi(\dot{\gamma})$ -curves exhibit almost no  $N_C$ -dependence, similarly to the equilibrium case, where the free volume is also density-independent (at a given temperature) due to the fixed lattice-constant [82]. As  $\dot{\gamma}$  exceeds  $\dot{\gamma}_c$ , the strings fluidize, which manifests itself in the rapid,  $N_C$ -dependent decrease of  $\Phi(\dot{\gamma})$ . The curves decay faster for higher  $N_C$  and the inflection points shift, as predicted by the theory, to higher shear-rates.

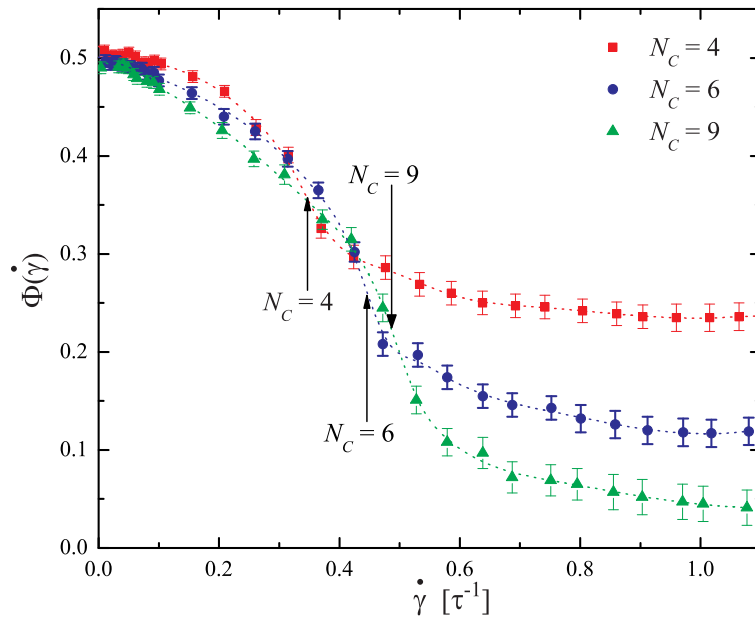


Figure 5.5.: Free volume fraction of the GEM particles,  $\Phi(\dot{\gamma})$ , for the three systems investigated (as labeled). Results are shown for cluster crystals oriented in  $[100]$  direction. Minima in  $d\Phi/d\dot{\gamma}$  are indicated by vertical arrows.



### 5.1.2. Shear-Induced Crystallization

We then studied the possibility of accelerating the nucleation rates in undercooled liquids through shear. The question of whether steady shear facilitates [158] or suppresses [185] the nucleation of a crystal from the metastable melt is a longstanding debate, and it seems that the answer is not universal, but instead strongly system dependent. For soft colloids, such as copolymer micelles, experimental evidence supports the acceleration of nucleation due to shear. Since the above mentioned strings formed out of *both* crystals *and* supercooled fluids, shear provides a way to reduce the spatial symmetry, bringing thus the system closer to full, three-dimensional broken translational invariance. This property opens up a unique pathway to possible nucleation, since it offers the system the possibility to augment its departure from full translational symmetry in a stepwise fashion, a possibility that is not present for hard colloids.

To investigate these questions, we thus applied the following shear-protocol: We considered supercooled fluids at the state points A, B, C (see Figure 5.2), and sheared them for a period of  $\tau_{\text{shear}} = 500$ . The shear computer experiments are conducted with  $\dot{\gamma} = 0.2$ , resulting in spontaneous string formation. Systems that have been prepared in this way are henceforward referred to as *presheared*. After the strings have emerged, we turned off the shear-flow and left the system to rest (total simulation time  $\tau_{\text{sim}} = 10000$ ). Then we analyzed the equilibrated structures, and compared them with those of *unsheared*, confined fluids of equal density and temperature, by calculating the free volume fraction  $\Phi$ , the one-particle density distributions  $\rho(\mathbf{r})$ , and the averaged bond order parameters  $\bar{Q}_4$  and  $\bar{Q}_6$  [188, 190] of the equilibrated final structures.

Here, we first identified the clusters along the lines of Ref. [186], and then determined the bond order parameters for the ideal fcc structure ( $\bar{Q}_4^{\text{fcc}} = 0.135 \pm 0.003$  and  $\bar{Q}_6^{\text{fcc}} = 0.264 \pm 0.004$ ) and for the uniform liquid state ( $\bar{Q}_4^{\text{liq}} = 0.110 \pm 0.003$  and  $\bar{Q}_6^{\text{liq}} = 0.125 \pm 0.003$ ). Finally we calculated the values of  $\bar{Q}_4$  and  $\bar{Q}_6$  for the presheared and unsheared systems and compared them with our reference values. In what follows, all results are shown for the [100]-orientation (unless explicitly stated otherwise), since the orientational dependence turned out to be very weak.

The results for the free volume fraction and for the bond-order parameters are shown in Table 5.2, and at a first glance, *no* effect of the different treatment is observable. However, we have to keep in mind that the bond order parameters are a measure for the averaged *local* crystalline order, and give only limited information about the *global* ordering of the system. Evidently, a more appropriate measure of long-range order is called for, and this is offered by the averaged one-particle density  $\rho(\mathbf{r})$  of the system. Indeed, and following also the terminology of Ref. [184], we term a system as fluid for which the one-particle density has the

$N_C$	$\Phi$	$\bar{Q}_4$	$\bar{Q}_6$
4 (presheared)	0.496	0.098	0.267
4 (unsheared)	0.494	0.101	0.268
6 (presheared)	0.506	0.094	0.252
6 (unsheared)	0.508	0.098	0.260
9 (presheared)	0.511	0.109	0.262
9 (unsheared)	0.512	0.110	0.254

Table 5.2.: Free volume fraction  $\Phi$  and bond order parameters  $\bar{Q}_4$  and  $\bar{Q}_6$  for the presheared and unsheared system.

same symmetry as the underlying Hamiltonian, and as crystalline one in which translational symmetry is broken in a periodic fashion. Accordingly, systems for which  $\rho(\mathbf{r}) = \rho(x)$  only, are supercooled confined fluids, whereas if a density profile depending on all three spatial coordinates,  $\rho(x, y, z)$ , results, we talk about a solid. Naturally, in the latter case, spatial periodicity in the  $y$ - and  $z$ -directions compatible with the fcc-crystal must also be present, whereas in the  $x$ -direction only a finite number of fcc elementary cells can be present.

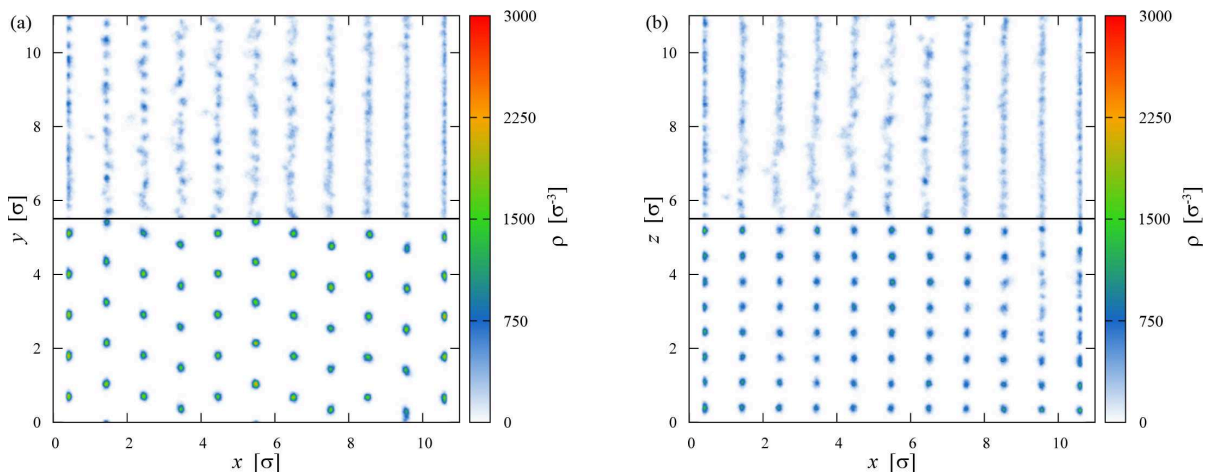


Figure 5.6.: Two-dimensional color coded density profiles for  $\rho = 3.9$ . The left panel shows the distribution in the gradient-vorticity plane, while the right panel shows the data in the gradient-flow plane. The top half of each image shows the unsheared system, while the lower half shows the presheared system (after cessation of shear).

Employing this criterion, a remarkable difference between the presheared and the unsheared systems emerges, as can be seen in Figures 5.6 and 5.7: while the unsheared systems show spatial modulation only in the  $x$ -direction, the lattice sites in the presheared systems are very well separated from each other, and the latter easily find their way to crystallization after



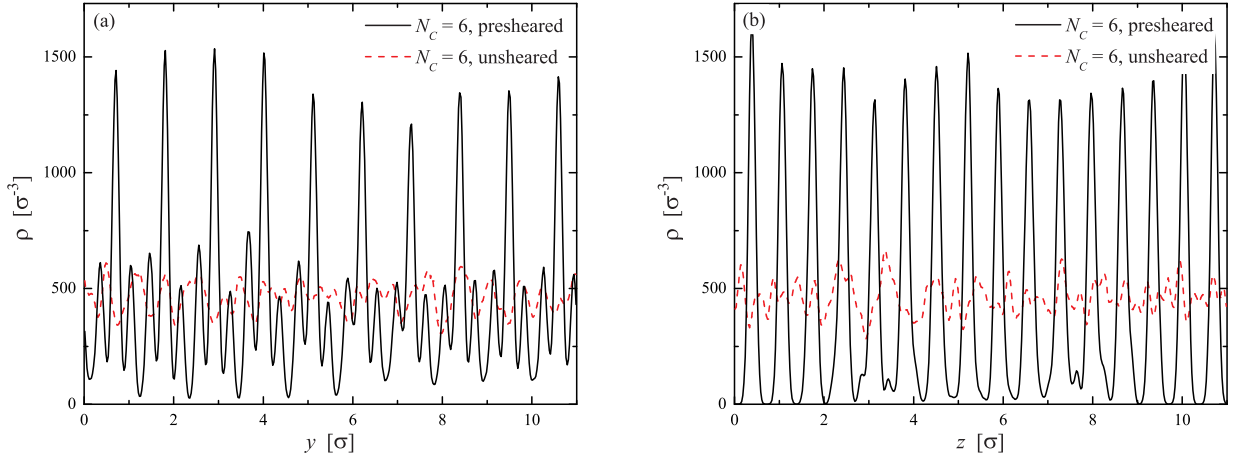


Figure 5.7.: Density profiles for  $\rho = 3.9$  along the vorticity ( $y$ ) and flow ( $z$ ) direction. Continuous lines show results for the presheared setup, while dashed lines represent the unsheared systems.

shear. This distinction is most pronounced for the system with the lowest density ( $\rho = 2.6$ ), but disappears completely for the densest one ( $\rho = 5.9$ ), since the nucleation barrier decreases as  $\rho$  grows, and thus preshearing is not necessary to accelerate crystallization anymore.

It can hence be argued that, for the  $Q^\pm$ -systems, shear has a profound effect in bringing about an effective lowering of the nucleation barrier, thereby accelerating the crystallization rates. This happens through a particular dynamical pathway that involves first the breaking of the symmetry in the gradient- and vorticity-directions through the formation of a two-dimensional triangular lattice of strings, which then proceeds to relaxing towards a crystal after the cessation of shear. The physical reason behind this pathway rests, again, on the particular property of these systems to have an hidden propensity to an instability towards spatial modulation with wavenumber  $k_{\min}$  (see Section 3.3).

Whereas in the unsheared system this instability was not sufficient to induce immediate crystallization, and the fluid thus remained trapped in a metastable phase for long times, once shear had been applied, spatial modulation in two dimensions took place as the result of the external drive. Along the flow direction, the strings had liquid-like ordering, which was, however, only sustainable as long as shear was on. Once the latter ceased, the liquid-like strings were not stable anymore, and the existing two-dimensional order offered an effective “substrate” on which the particles along the string performed an essentially one-dimensional nucleation, clumping into clusters and building up the thermodynamically stable crystal. Naturally, the deeper we went into the region of stability of the solid, the less the effect of shear was, since nucleation barriers decreased as the distance from the crystallization point grew.

## 5.2. Cluster Crystals under Poiseuille Flow

### 5.2.1. Flow Profiles and Crystal Transport

Before proceeding to a detailed description of the results of our numerical experiment, it is worth anticipating on a *qualitative level* the behavior of the cluster crystal and of the solvent under pressure flow conditions, on the basis of previously-known results and physical argumentation. Suppose first that the external pressure gradient is strong enough, so that the inserted cluster crystal (which is hydrodynamically coupled to the fluid) can be treated as a perturbation, *i.e.*, let us assume that the solvent velocity profile given by Eq. (2.18) remains essentially unaffected by the solute. This implies that the latter is locally exposed to shear rates given by:

$$\dot{\gamma}^{(0)}(x) = \frac{\partial v_z^{(0)}(x)}{\partial x} = \frac{\rho_s g}{2\eta}(L_x - 2x). \quad (5.7)$$

Based on previous findings (see Section 5.1.1), we know that cluster crystals under shear react by forming strings that are aligned along the flow direction and they self-assemble on a triangular lattice on the gradient-vorticity plane. Accordingly, one could argue that such strings also form under Poiseuille flow conditions. However, as can be seen from Eq. (5.7), the shear-rate at the center of the channel vanishes. Given the fact that a small but finite shear-rate is necessary for the formation of strings, this local analysis would imply that there are a few (and, at any rate, at least one) crystalline layer(s) in the middle of the channel, lying perpendicular to the gradient direction (*i.e.* on the flow-vorticity plane), which do not melt. Instead, they remain intact in their crystallinity, and they are simply driven along by the fluid flow. However, this scenario of simultaneous presence of two-dimensional crystalline layers drifting on the  $(y, z)$ -plane and of parallel strings oriented along the  $z$ -axis is untenable. Indeed, in such a case, the crystalline layers would act on the neighboring strings, located immediately close to them along the gradient direction, as external potentials. Since the relative velocities  $v_{\text{rel}}$  of particles displaced along the gradient direction are non-vanishing, these external potentials would feature periodic, spatiotemporal modulation along the flow-direction. The potential acting on the strings would thus have the form of some function  $f(z - v_{\text{rel}}t)$ , whose explicit expression depends on the interparticle interaction, spacing, and cluster occupancy  $N_C$  but it is otherwise irrelevant for the rest of the argument. However, under the action of such an external potential, the strings would no longer be able to maintain their spatial uniformity along the  $z$ -direction, and they would break up into clumps (see the discussion on the acceleration of the nucleation rates in the preceding Section). Such a breakup would then act as an additional external potential to the next neighboring strings, with the result that they would also break up and so on.

The above considerations bring forward a property of the string phase that has already been briefly addressed in the previous Section, namely that it is *global*: its stability rests on the fact that the whole, macroscopically large domain of the system forms strings but the latter cannot coexist with some other phase of different spatial symmetry in the sense of a microphase separation between the two. Thus, a different scenario emerges, in which the intact crystallinity of the central layers under Poiseuille flow causes a macroscopically thick crystalline slab to be stable within the channel. This possibility is supported by the fact that the solute acts back on the solvent, modifying its own velocity profile. Consequently, if such a thick chunk of crystal would flow along the fluid in the channel, then the modified solvent velocity,  $v_z(x)$ , would be forced, by symmetry arguments, to be flat (*i.e.* essentially  $x$ -independent) far away from the walls. In such a case, the resulting local shear rate  $\dot{\gamma}(x) = \partial v_z(x)/\partial x$  would be vanishingly small in that flat region, preserving the intactness of the crystalline structure. This scenario, though by no means proven on the basis of the present physical argumentation *alone*, is at least free of internal contradictions, as the preservation of the crystalline symmetry and the flatness of the solvent velocity profile are in principle consistent with one another. And though the starting point of the argument was formulated under the assumption of undistorted solvent velocity profiles, the whole *Ansatz* evidently maintains its validity in the opposite case of weak external flow.

The results of our simulations fully confirm that indeed the above scenario materializes in practice. They offer a prime example of the ways in which the properties of the suspended particles bring about a dramatic modification of the flow properties of the pure solvent. In contrast to shear experiments, transport flow does *not* necessarily destroy the crystallographic order, but rather leads to a (slight) deformation and displacement of the crystal as a whole.

For further insight into the system's flow behavior, it is worthwhile to have a look at the velocity profile of the liquid. Figure 5.8 shows  $v_z(x)$ , that is the flow velocity in gradient direction at  $g = 0.05$ . First of all, it is well visible that the velocity profile deviates strongly from the parabolic shape it would have in the absence of the crystal; in fact, the fluid develops a profile that is very akin to *plug flow*, and which has been experimentally observed for pressure-driven flow of both intermediate-density colloidal gels [171, 172] and concentrated colloidal suspensions [176–178], including the transport through channels with spatial constrictions [173, 175, 179]. Moreover, the flat plateau broadens and its maximum drops with increasing particle density  $\rho$ , reflecting the resistance exerted by the crystal on the fluid. We can decompose this flow profile into three parts, namely two outer regions in which we find an almost linear velocity gradient, and one inner regime in which the velocity is constant. This in turn means that while an ordered slab of solute particles in the central area stream with a steady velocity, the particles closer to the walls experience considerable shear forces

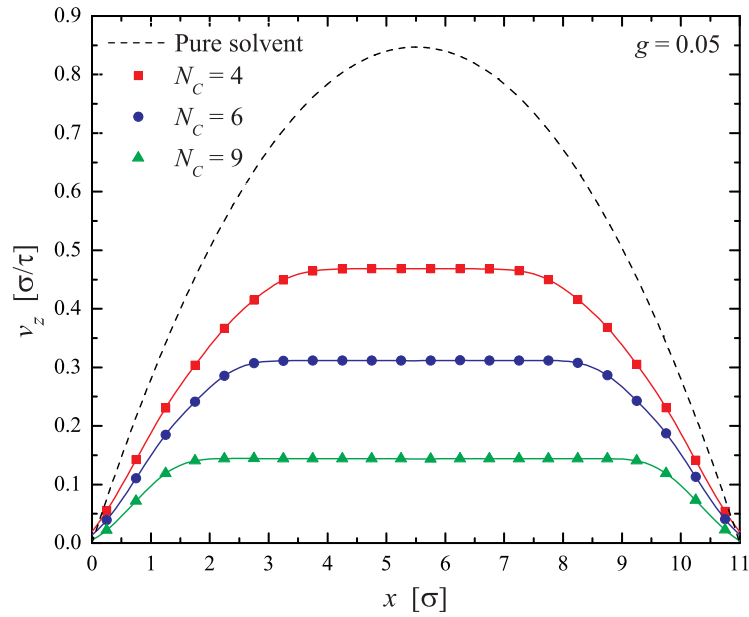


Figure 5.8.: Velocity profile of the liquid in the presence of the GEM-crystal for the [100]-orientation at  $g = 0.05$  and for different values of  $N_C$ , as labeled. The points are results from the simulation, whereas the solid lines are fits according to Eq. (5.9). The dashed line shows the profile for the pure solvent under the same value of the external drive. The presence of the GEM particles results in a (weak) wall-slip, which decreases with  $N_C$ .

and hence lose their crystalline ordering.

The dependence of the velocity profiles on  $g$  will be analyzed in more detail in the following Subsection. Here, we present further quantitative results for the behavior of the solute particles under flow. We first look at the dependence of the free volume fraction  $\Phi$  on  $g$  (results are shown in Figure 5.9). In the equilibrium state with zero flow ( $g = 0$ ), the free volume fraction of the denser crystals is slightly lower than that of their more dilute counterparts, due to thermal fluctuations. Upon increasing  $g$ , the corresponding  $\Phi$  values remain then constant, until they drop at a layer-melting transition, when the outermost GEM-particles are released from their initial clusters. We can readily observe that these transition points (indicated by the arrows) shift to higher  $g$ -values as  $N_C$  is increased. Also the fact that the fluid resistance is more pronounced for higher  $N_C$  and less layers are liquefied is reflected in the weaker decline of the respective curves.

In order to study the crystal structure in a more quantitative fashion, we have calculated the averaged local bond order parameters,  $\bar{Q}_4$  and  $\bar{Q}_6$ , for each density and plotted the results as a function of  $g$ ; the results are shown in Figure 5.10. The inspection of  $\bar{Q}_4$  and  $\bar{Q}_6$  reveals that, although the crystal is slightly deformed as a whole, its *local* structural integrity is still

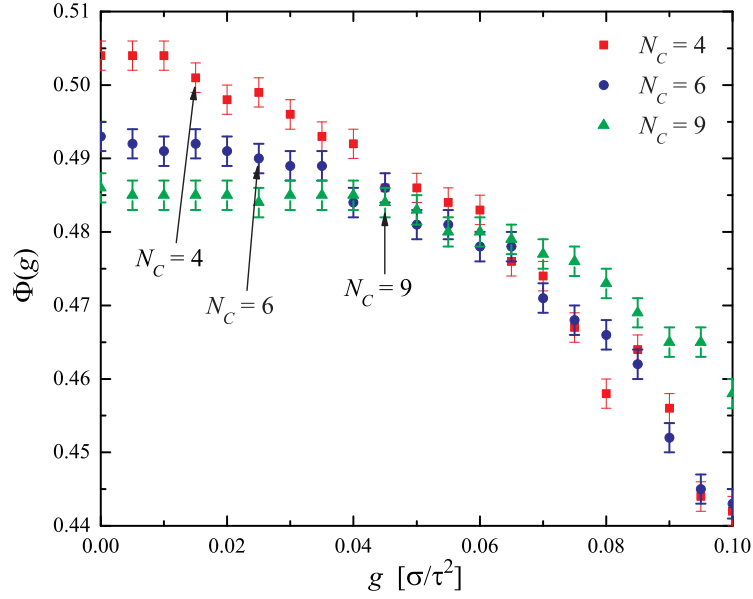


Figure 5.9.: Free volume fraction of the GEM particles,  $\Phi(g)$  for the [100]-orientation and for different values of  $N_C$ , as labeled. The arrows indicate the  $g$ -value, at which the outermost layers melt for the first time.

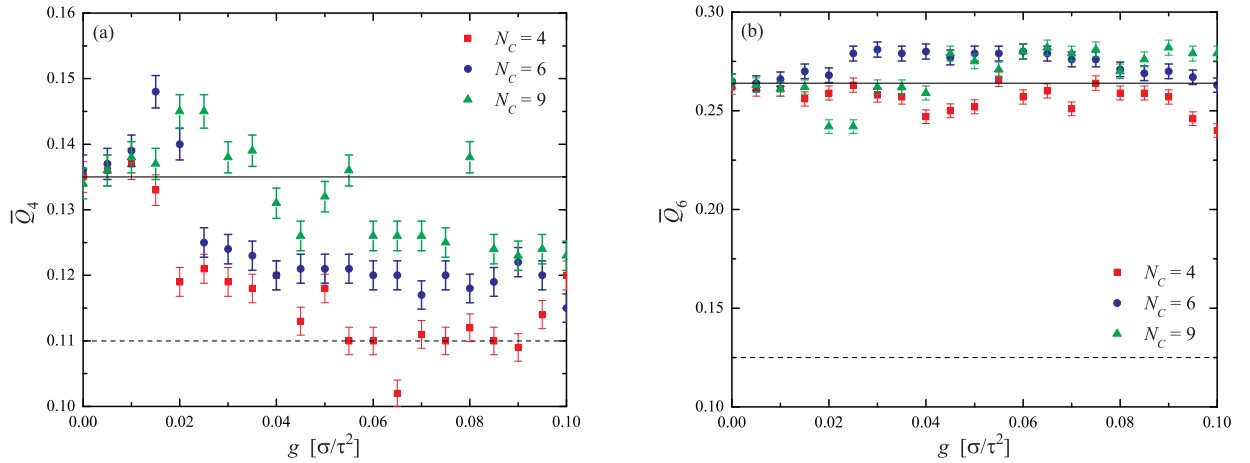


Figure 5.10.: Bond order parameters  $\bar{Q}_4$  (left panel) and  $\bar{Q}_6$  (right panel) as functions of the gravitational force parameter  $g$  and for different values of  $N_C$ , as labeled. The symbols show the data at indicated occupancy number  $N_C$ , while the lines represent the reference bond order parameters for the fcc arrangement (solid line) and the disordered arrangement (dashed line).

preserved to a high extent. Moreover, the progression of  $\bar{Q}_4$  supports our finding that the less dense systems liquefy more easily, since the respective values show a distinct trend towards  $\bar{Q}_4^{\text{liq}}$ . This statement, however, has to be treated with caution, since the difference between the values of the parameters of the ordered and uniform system is rather small.

### 5.2.2. Flow Quantization

A more detailed analysis of the velocity profiles and their dependence on  $g$  reveals a number of striking features that are unique to the cluster crystals. The plug-flow dependence of the velocity on  $x$  is, of course, not a feature unique to the latter: indeed, previous experiments with both intermediate-density colloidal gels [171–173] and with concentrated colloidal suspensions [176, 177, 179] have resulted into flows that have very similar shapes to the representative results shown in Figure 5.8. In fact, a phenomenological approach exists, which yields such plug-flows in conjunction with the Navier-Stokes equations, namely the Herschel-Bulkley model [187], which is based on the following postulated dependence of the shear stress  $\sigma_{xz}$  on the shear rate  $\dot{\gamma}$ :

$$\sigma_{xz} = \eta \dot{\gamma}^n + \sigma_0, \quad (5.8)$$

with the yield stress  $\sigma_0$ , the viscosity  $\eta$  of the complex fluid and the shear-thinning exponent  $n$ . The Herschel-Bulkley model has been applied to describe the plug-flow profiles in colloidal disordered gels [171]. In our case, the underlying physics is different, so that an attempt to describe the flux data with this model does not seem particularly advantageous. We resort instead to an *ad hoc* fit of the velocity profiles with a function of the form:

$$v_z(x) = A \tanh(Bx) + A \tanh(B(L_x - x)) + C, \quad (5.9)$$

involving the fit parameters  $A$ ,  $B$  and  $C$ . We emphasize that there is no underlying model behind Eq. (5.9) above; we rather employ it as a straightforward tool to extract quantitative information on three key characteristics of the plug flow, namely the height  $h$  of the velocity profile, the width  $w$  of its flat part and the wall-slip velocity  $s$ . These are readily obtainable from the fit parameters as:

$$h = 2A \tanh(BL_x/2) + C, \quad (5.10)$$

$$w = L_x - 2/B, \quad (5.11)$$

and

$$s = A \tanh(BL_x) + C. \quad (5.12)$$

The typical quality of the fit can be seen in Figure 5.8. The results for the height, width and wall-slip of the velocity profiles are summarized in Figure 5.11.

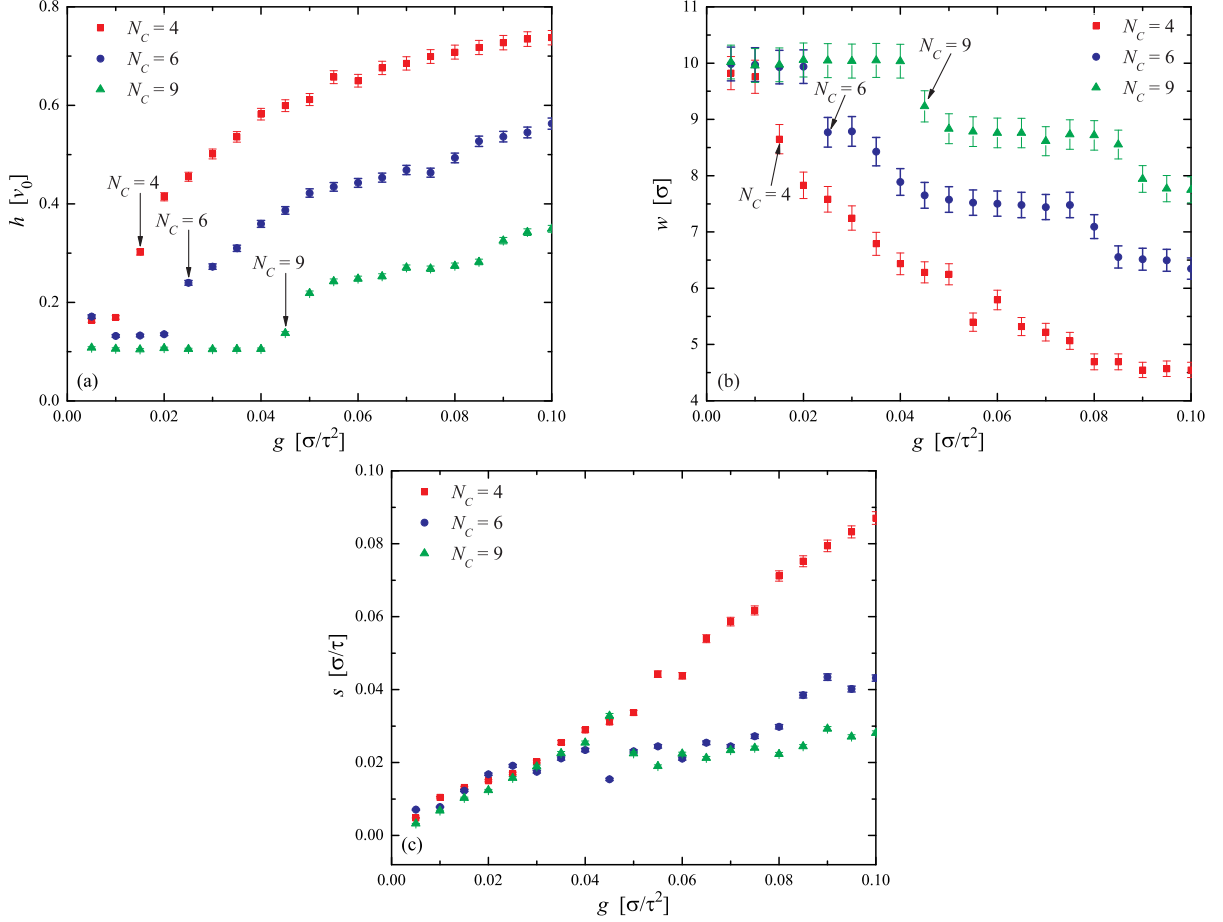


Figure 5.11.: (a) The plateau height  $h$  (maximum of the velocity profile) of the plug flow pattern of GEM-8 crystals driven by pressure, for crystals of different occupancy  $N_C$ , as a function of the magnitude of the driving force  $g$ . The height is expressed in units of the maximum,  $v_0$ , of the parabolic velocity profile in the absence of the GEM-8 particles, see Eq. (2.19); (b) The width  $w$  of the flat part of the velocity profile, for the same parameters as in (a); (c) the corresponding wall-slip velocity  $s$ . All results refer to a slit of width  $L_x = 11\sigma$ , and the positions of the arrows correspond to the ones in Figure 5.9.

The dependence of the plateau height on  $N_C$  and  $g$ , Figure 5.11(a), reveals some remarkable novel features. First, we notice that the presence of the crystal slows down the flow, at fixed  $g$ , as compared to the pure solvent; this slowdown is more severe as the cluster occupancy grows, since the presence of more GEM-8-particles increases the number of collisions with

the solvent. Second, and focusing for now on the less dense crystal,  $N_C = 4$ , we find the existence of a two-stage process in the flow: for sufficiently small values of  $g$ , the flow profile is independent of the strength of the external pressure drop, a feature akin to granular, non-Brownian matter [175, 178], whereas at higher values of  $g$  the flux increases with it. Recently, Campbell and Haw [178] established a similar behavior for the flow of concentrated colloidal dispersions, in which, however, the crossover from colloidal to granular flow took place by increasing the volume fraction of the suspension. Here, the transition occurs instead at fixed concentration of the solute, and it takes the form of a dynamical “phase transition” with the strength of the external field  $g$  as a control parameter. Even more remarkable is the evolution of these phenomena when looked upon as functions of the occupancy  $N_C$ . By increasing the latter, the critical value  $g_c$  denoting the transition between colloidal and granular-like flow increases (see Figure 5.11(a) for  $N_C = 6$ ). Moreover, by going now to the most dense system,  $N_C = 9$ , a transition from the first to a second plateau is observed, and possibly even to a third. Increasing the pressure drop induced *via*  $g$  leads to discrete values of the flux, separated by well-defined jumps, which are caused by a successive melting of layers close to the walls. The number of melted layers can be estimated from the corresponding value of  $w$ . Whereas for low-occupancy crystals the melting of a layer leads to colloidal-flow behavior, for high-occupancy numbers the scenario is self-repeating after successive melting of additional layers, producing thereby a new plateau in which the flow of the system is granular-matter-like. We call this remarkable behavior *flow quantization*, and we trace its appearance in the particular nature of the cluster crystals. To the best of our knowledge, it has not yet been seen for other, common colloidal systems.

The width of the plateau, see Figure 5.11(b), shows the signature of flow quantization even more strongly than the plateau height. There, it can be seen that with each successive pair of molten, lubricating layers at the edges of the system, the plug-like, flat part of the profile becomes narrower, and that the width remains roughly constant until the next border layers melt. This feature, allows us to gain control not only on the strength  $h$  of the flowing beam but also on its focus  $w$ . Finally, the wall-slip velocity  $s$ , Figure 5.11(c), shows a constant growth with  $g$  for the less dense system but it carries the signature of the discrete plateaus for the denser ones,  $N_C = 6$  and  $N_C = 9$ . It should be kept in mind, however, that  $s$  is a small number and thus prone to errors in the fitting procedure.

Figure 5.12 shows the flux of solute particles  $\Psi(g)$  across the simulation box, *i.e.* the number of particles passing through the gradient-vorticity plane in unit time, and a significant dependency on  $N_C$  is clearly visible. While for very small  $g \lesssim 0.01$  the curves collapse onto each other, their progression differs distinctively with increasing  $g$ . For  $N_C = 4$ ,  $\Psi(g)$  is almost completely linear, whereas for  $N_C = 6$  subtle kinks, and for  $N_C = 9$  very pronounced



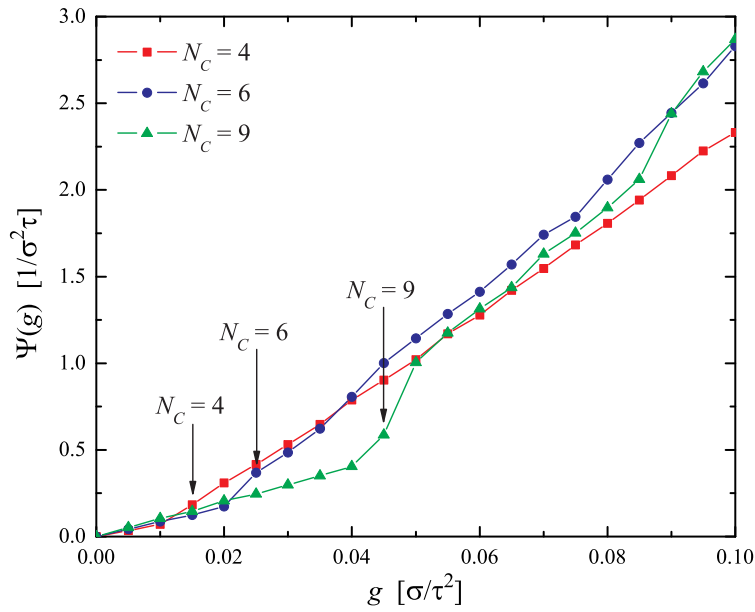


Figure 5.12.: Particle flux  $\Psi(g)$  as a function of the gravitational force  $g$  for the [100]-orientation. The positions of the arrows are the same as in Figure 5.9.

jumps are noticeable. These non-linearities stem from the fact that with an increasing pressure gradient the crystalline layers close to the walls melt and thus reduce the drag forces on the remaining intact lattice. Since the potential energy of the cluster crystal is proportional to the number of particles at each lattice site, the critical flow, at which the outermost layer melts for the first time, increases with  $N_C$ . Hence for small and intermediate  $g$ , the flux of the thinner systems is higher, since the liquefied layers act as a lubricant. However as  $g$  is increased further, the outer layers melt in the denser systems as well, and the respective fluxes catch up and eventually overtake. Finally it is noteworthy, that the plateaus in Figure 5.11(a) translate here into linear curves due to the linear dependency of  $v_0$  on  $g$ .

Both the existence of a transition from granular to colloidal flow and the presence of discrete plateaus are unique characteristics of the transport properties of cluster crystals. It is reasonable to assume that the number of plateaus will increase and the constancy of their values will become sharper for higher values of  $N_C$  and also for higher widths  $L_x$  of the confining channel (not studied here).



## 6. Conclusions

In this work we have studied the non-equilibrium behavior of various soft matter systems by extensive computer simulations and theoretical analysis. We have found that these systems exhibit unique transport properties under confinement and that they react in a very peculiar way to external forces, such as shear or pressure driven flow.

First, we systematically investigated the effect of confinement on the diffusion of rigid tracer particles by FCS experiments and complementary Brownian dynamics simulations. For this purpose, periodic porous nanostructures are excellent platforms, since the three relevant scales – tracer radius  $a$ , pore diameter  $L$ , and cavity radius  $R$  (see Figure 3.1) – along with particle-wall interactions can be tuned in well-defined ways. We examined the diffusion law and the slowing down of particle diffusion as a function of  $a/R$  at the confining environment of three i-opals characterized by the ratio  $L/R$  while keeping the particle-wall interaction potential fixed. Brownian dynamics simulations predicted a normal Fickian diffusion for all examined particles and i-opals with different geometrical confinements. The translational diffusion dropped almost exponentially with the “frustration ratio”  $a/R$  at a constant confinement environment. Relaxing the geometrical constraint (increase of  $L/R$ ), the slowdown was reduced due to the increasing particle escape rate from the cavity through the opening. At vanishing  $a/R \rightarrow 0$  there was a residual slowing down ( $\zeta_0 \sim 1.8$ ) as the particle remained confined. The predicted confined dynamics in i-opals was confirmed by the present experiment. Only for the strongest confining medium and highly frustrated particles an anomalous diffusion was observed. Under these severe conditions, the low but finite size polydispersity can impact the diffusion mechanism.

The theoretical modeling and simulation revealed that the long-time motion of the tracer particles in this highly ordered, porous nanostructure is strictly diffusive. In particular, the diffusion of the quantum dots can be visualized as a succession of “bounces” against the cavity walls, which delay the escape from the interior of the same, until a successful event takes place in the cavity and the particle translocates to the interior of the adjacent one. There, the process repeats itself and a random walk with a characteristic step length  $R$  and characteristic time  $\tau_{\text{esc}}$  results. Thus, the “bouncing-and-escape” succession within a cavity is the mechanism responsible for the overall, measured and calculated, delay factors.

Based on these findings, we expect new material and nanostructure designs to emerge, as well as a better understanding of existing devices to be gained. The slowdown factor paradigm is scalable and hence can be applied to a wide range of nanostructured materials. For

instance, an increase in interface and constrained diffusion can help to design compartments of intrinsically long reaction/detection times. Emerging filters and membranes [88] increasingly push for high surface areas to interact more effectively with any type of analytes. The large interface model system studied here adds towards targeting of these needs. Variation of the particle asphericity (from spheres to rods) and tuning of the interactions (charged particles, soft interfacing of the walls) are two examples in the rich parameter space that is left to be explored.

In the second part of this thesis, we employed a theoretical scaling analysis to establish the independence of the current injection threshold into narrow channels for low-generation dendrimers, which has been confirmed by hybrid computer simulations. We established that the translocation times of dendrimers and linear polymers of the same molecular weight along such channels were quite similar to one another as long as the channel walls were smooth. However, wall granularity had dramatic effects both on the translocation times as such and on the relative duration of transport between dendrimers and polymers. In particular, localized, attractive linear patches brought forward for the dendrimers a kind of motion akin to “walking along the wall”, with long plateaus of residence times on the attractive patches, whereas linear polymers did not escape the patchy channel within simulation times.

Our findings establish that dendritic molecules are peculiar in their transport properties along narrow channels and they express, also under flow, their unusual character as hybrids between compact colloids and flexible polymeric objects, already known from their equilibrium behavior [73, 130, 132]. The long residence times of the dendrimers on the wall traps open up the interesting possibility that, when the former are loaded with some chemical cargo (*e.g.*, a drug molecule), the latter could be delivered on the patch and be absorbed there during the carrier’s residence time, while the blood flow “washes away” the empty dendrimer afterwards. This topic, along with investigations on the effects of more complex channel geometries and charge can be the subject of future investigations.

In the final part of this thesis, we studied the rheological properties of ultrasoft colloidal cluster crystals. First we investigated their response to shear flow, and we discovered that these systems respond to shear through a novel scenario: shear-banding occurs at low shear-rates, followed by string formation, in which the flow-aligned strings formed by the interpenetrating particles order in a hexagonal lattice on the gradient-vorticity plane. Beyond a critical shear-rate, the string phase melted into a disordered fluid with a concomitant increase of the viscosity. This form of self-organization arises from penetrability: in contrast to hard colloids [143], no zig-zag or sliding planes are necessary to relax the stresses, since particles can go *over one another*. Cluster crystals emerge thereby as novel materials that show unique and universal characteristics not only in equilibrium but also under external

---

drive. The formation of ordered strings on a triangular lattice bears striking similarities to the Abrikosov lattice of superconductors. Further, the emergence of long, connected “wires” under shear can be seen as a type of a transition from an isolating (clusters) to a shear-induced conducting material (strings). Additionally, we found that the existence of this string phase offers the system an easy pathway towards crystallization, due to the existence of partially broken spatial symmetry under shear. Once shear ceases, the next step towards full, three-dimensional symmetry breaking happens instantaneously. In this way, an effective extinction of the nucleation barrier is brought about, and an efficient way for crystallizing these soft particles opens up.

Subsequently we analyzed the flow behavior of these cluster crystals under Poiseuille flow. We found that the presence of the crystal drastically affects the flow pattern of the dispersion, *i.e.* resulting into a pronounced flattening of the usually parabolic shape, and thus bringing about what is known in literature as *plug flow*. In those regions of the channel where the velocity profile was essentially flat, the solvent flowed with almost constant velocity and the structural integrity of the whole lattice was preserved (aside from a weak distortion). Close to the walls however, where the velocity profile was almost linear, the crystal liquefied. Moreover, we discovered that the flow became *quantized* as the pressure drop along the channel was increased. The flow-profile *vs.* pressure curves displayed broad plateaus with sudden jumps between them, each corresponding to the melting of two additional layers of the remaining cluster crystal slab which flowed with constant velocity in the center of the channel. The width of the flat part of the velocity profile showed a similar discretized evolution. This behavior bears on one hand some similarities to the flow of concentrated colloidal suspensions or gels but on the other hand has also significant differences, which render the cluster crystals unique among complex fluids in their transport flow behavior.

All these characteristics have their origin in the ultrasoft, penetrable and cluster-forming nature of the  $Q^\pm$ -class of systems. Our findings underline their highly unusual properties not only in equilibrium but also under the influence of external fields. Future work should now focus on the attempts to assemble these crystals on a microscopic basis and on appropriate treatment of the dynamics of the same.



# Appendix





# A. Parameters

---



---

$a$	lattice constant	Section 2.3
$a$	radius of tracer particle within inverse opal	Eq. (3.1)
$\mathbf{a}$	acceleration of solute particle	Eq. (2.3)
$d$	wall thickness of inverse opal	Table 3.1
$D$	diffusion coefficient	Section 2.3
$D$	channel diameter	Section 4.2.1
$D_s$	short time diffusion coefficient	Eq. (4.1)
$E$	total internal energy	Section 2.1
$E_{\text{kin}}$	kinetic energy	Section 2.1
$E_{\text{pot}}$	potential energy	Section 2.1
$\mathbf{F}$	force on solute particle	Eq. (2.2)
$\mathcal{F}$	force per unit volume	Eq. (2.3.1)
$\mathcal{F}$	total free energy	Eq. (4.12)
$\mathcal{F}_{\text{conf}}$	configurational contribution to $\mathcal{F}$	Eq. (4.12)
$\mathcal{F}_{\text{hyd}}$	hydrodynamic contribution to $\mathcal{F}$	Eq. (4.12)
$g$	gravitational constant	Eq. (2.18)
$G(t)$	autocorrelation function	Section 4.1
$\mathbf{G}_{\alpha\beta}$	gyration tensor	Eq. (3.6)
$\mathbf{H}_{ij}$	hydrodynamic tensor	Eq. (2.6)
$\mathcal{H}$	Hamiltonian	Eq. (2.1)
$i$	particle index	Eq. (2.1)
$I$	moment of inertia of solute particle	Eq. (2.33)
$j$	particle index	Eq. (2.2)
$k$	wave number	Section 3.3
$k_B$	Boltzmann's constant	Eq. (2.9)
$L$	pore diameter of inverse opal	Table 3.1
$L$	channel length	Section 4.2.2
$L_x, L_y, L_z$	box lengths	Chapter 2
$\mathbf{L}$	angular momentum of solute particle	Eq. (2.33)
$m$	mass of solute particle	Eq. (2.1)
$m'$	mass of solvent particle	Section 2.3

$N$	number of solute particles	Eq. (2.1)
$N_C$	cluster occupancy	Section 3.3
$N_s$	number of solvent particles	Eq. (2.24)
$p(\dots)$	probability distribution	Eq. (2.29)
$\bar{Q}$	averaged bond order parameter	Section 5.1.2
$r$	distance	Eq. (3.2)
$\mathbf{r}$	position of solute particle	Eq. (2.1)
$\mathbf{r}'$	position of solvent particle	Eq. (2.11)
$R$	cavity radius of inverse opal	Table 3.1
$R_G$	radius of gyration	Eq. (3.5)
Re	Reynolds number	Eq. (2.17)
$t$	time	Eq. (2.3)
$T$	temperature	Section 2.1
$\Delta t$	timestep	Eq. (2.3)
$\mathbf{u}$	average velocity of MPCD cell	Eq. (2.12)
$U$	(pair) potential	Eq. (2.1)
$\mathbf{v}$	velocity of solute particle	Eq. (2.1)
$\mathbf{v}'$	velocity of solvent particle	Eq. (2.11)
$V$	volume	Section 2.3
$x$	gradient direction	Section 2.3.1
$y$	vorticity direction	Section 2.3.1
$z$	flow direction	Section 2.3.1
$\alpha$	MPCD rotation angle	Eq. (2.12)
$\alpha$	Cartesian component $(x, y, z)$	Eq. (3.6)
$\beta$	inverse temperature	Eq. (2.29)
$\beta$	Cartesian component $(x, y, z)$	Eq. (3.6)
$\dot{\gamma}$	shear-rate	Section 2.3.2
$\epsilon$	energy parameter in pair potentials	Eq. (3.1)
$\zeta$	slowdown factor	Section 4.1
$\eta$	dynamic viscosity	Section 2.3
$\kappa$	inverse of decay length	Eq. (3.1)
$\lambda$	mean free path of solvent particle	Section 2.3
$\nu$	kinematic viscosity	Section 2.3
$\xi$	friction coefficient	Eq. (2.6)

---

$\rho$	solute number density	Section 3.3
$\rho_s$	solvent number density	Eq. (2.15)
$\rho(\dots)$	density distribution	Section 5.1.2
$\varrho_s$	solvent density	Section 2.3
$\sigma$	particle diameter	Eq. (2.25)
$\sigma_0$	yield stress	Table 5.1
$\sigma$	stress tensor	Section 2.3.2
$\Phi$	free volume fraction	Section 5.1.1
$\Psi$	particle flux	Section 5.1.1
$\Omega$	MPCD rotation Matrix	Eq. (2.12)
$\nabla$	gradient with respect to positions	Eq. (2.2)
$d/dt$	total derivative with respect to time	Eq. (2.2)
$\partial/\partial x$	partial derivative with respect to space	Eq. (5.7)
$\langle \dots \rangle$	average	Section 2.2

Table A.1.: List of selected symbols.



# B. Data Analysis

## B.1. Local Bond Order Parameters

When studying crystallization from undercooled liquids, it is crucial to be able to distinguish particles that are part of the crystal from those that belong to the disordered phase. In fact, two distinct broken symmetries distinguish crystalline solids from isotropic liquids: broken translational invariance is measured by the phase of the periodic density modulations in a solid, and a broken rotational symmetry is defined by the singled-out crystallographic axes. These two symmetries are *not* independent, since rotating one fragment of a perfect crystal disrupts not only orientational correlations, but translational correlations as well.

Steinhardt *et al.* have devised a method, that relies on the *local* environment of the particles only, and that is independent of the specific crystal structure [188]. First, a set of spherical harmonics is associated with every “bond” joining a particle to its near neighbors:

$$Q_{lm}(\mathbf{r}) = \mathbf{Y}_{lm}(\theta(\mathbf{r}), \phi(\mathbf{r})), \quad (\text{B.1})$$

where  $\mathbf{r}$  denotes the midpoint of the bond,  $\mathbf{Y}_{lm}$  are the spherical harmonics, and  $\theta$  and  $\phi$  the polar angles of the bond measured with respect to an arbitrary reference coordinate system. Then, the order parameters are averaged over a suitable set of bonds in the sample:

$$\bar{Q}_{lm} = \langle Q_{lm}(\mathbf{r}) \rangle. \quad (\text{B.2})$$

The first non-zero averages occur for  $l = 4$  in samples with cubic four-fold symmetry and for  $l = 6$  in systems with icosahedral six-fold symmetry. Because the  $Q_{lm}$  can be scrambled drastically by changing to a rotated coordinated system, it is important to only consider rotationally invariant combinations, such as:

$$Q_l = \sqrt{\frac{4\pi}{2l+1} \sum_{m=-l}^l |\bar{Q}_{lm}|^2}, \quad (\text{B.3})$$

and:

$$W_l = \frac{\sum_{m_1+m_2+m_3=0} \begin{pmatrix} l & l & l \\ m_1 & m_2 & m_3 \end{pmatrix}}{\left(\sum_{l=-m}^m |\bar{Q}_{lm}|^2\right)^{3/2}}, \quad (\text{B.4})$$

where the term in the parentheses is the Wigner 3- $j$  symbol [189].

Using this approach, we can determine the type of crystal surrounding each individual particle. However, thermal fluctuations can smear out these order parameters so that it may be difficult to distinguish local crystalline structures. Lechner *et al.* refined this recipe in Ref. [190] by additionally taking into account the second shell around each particle. This increase in the accuracy of the distinction of different structures is gained however at the price of a coarsening of the spatial resolution. Nonetheless, we have decided to employ this variant of averaged local bond order parameters, since the different crystal structures can be distinguished considerably more accurately.

## B.2. Cluster Analysis

Investigating the dynamics of a cluster crystal requires a thorough analysis of the individual cluster objects. Therefore, we must decide on a reliable criterion to distinguish between different clusters and to identify the affiliation of a particular particle to a cluster in an unambiguous way at every step of the simulation. On this account, the inspection of the radial pair distribution function  $g(r)$  provides a first indication. From Figure B.1 we can see that  $g(r)$  exhibits a characteristic rise for small distances, and then decays rapidly until  $r_{\min}$  is reached.

The position of this minimum may serve as a measure of a cluster's spatial extent and allows us to determine the average cluster size,  $\langle N_C \rangle$ , by [191]:

$$\langle N_C \rangle = 1 + 4\pi\rho \int_0^{r_{\min}} g(r)r^2 dr. \quad (\text{B.5})$$

This criterion can undoubtedly be used to obtain a first, rough estimate for identifying those particles that belong to a particular cluster. However, clusters do *not* have well-defined boundaries, and thus  $g(r)$  does not vanish completely at  $r_{\min}$  (see the inset of Figure B.1). Particles migrating between two neighboring cluster sites of the cluster crystals are to be made responsible for this effect.

In what follows, we present a refined version [186] of the cluster identification algorithm originally presented in Ref. [83], which consists of the following four steps:

1. We start our procedure with the first particle and identify all surrounding particles within a given cut-off radius  $r_c$  as neighboring particles. This procedure is then repeated for all remaining particles. As a first guess, we employ  $r_c = r_{\min}$ , a value which will be corrected iteratively during the algorithm.

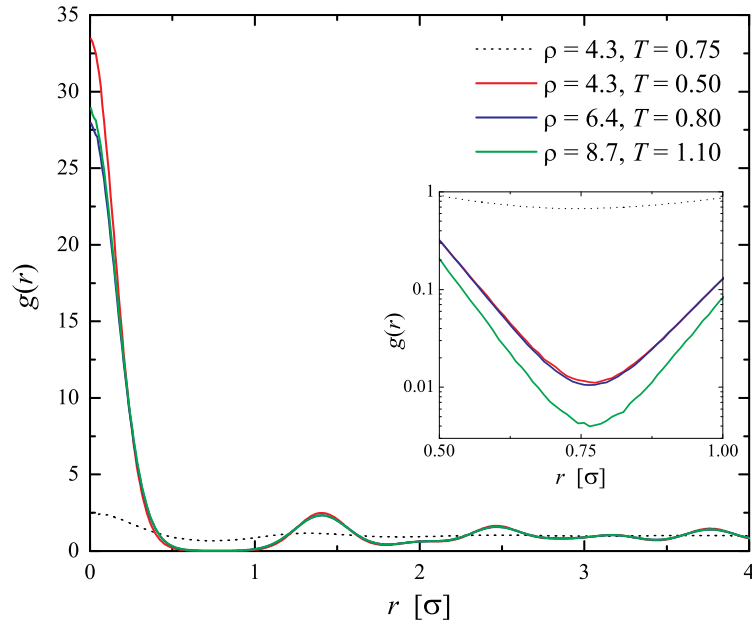


Figure B.1.: Radial pair distribution function  $g(r)$  of a GEM-4 cluster crystal as a function of distance  $r$ . From the inset we see that  $g(r)$  does not vanish completely at its first minimum  $r_{\min}$ .

2. With this information at hand, we head for the composition of the clusters. Therefore we start again with the first particle and label all its neighbors, their respective neighbors, and so on. Then we proceed to the next particle that has not been labeled yet and finally arrive at a state, where all particles have been assigned to a cluster.
3. At this stage, the algorithm reproduces exactly the same results obtained in Ref. [83]. However, this procedure might provide misleading data: as particles move from one cluster to another, the particles of these two clusters might now be counted to belong to the set of neighbors of the hopping particle, merging thereby the two clusters.

At first glance it seems that these problems can be overcome by simply reducing  $r_c$ , but this choice does not solve the problem: on the one hand, at high densities, situations can occur in which two or three particles are simultaneously hopping between clusters. Thus, taking a smaller cut-off radius does not address the issue of particles merging clusters. On the other hand, decreasing  $r_c$  bears the risk of leaving particles without any neighbors.

Therefore, we have employed a more sophisticated procedure, which does not solely rely on the mere reduction of  $r_c$ . To this end, we first introduce three check parameters  $N_C^{\min}$  and  $N_C^{\max}$ , the expected minimum and maximum cluster sizes present in our system

(roughly estimated from the cluster size distribution calculated after Step 1 and 2), and  $N_l$ , the number of lattice sites in the system. Then all clusters that have been identified in Step 2 will be reconsidered. If the size of one of them exceeds  $N_C^{\max}$ , the corresponding collection of particles is isolated from the rest of the system, and the search for neighbors is repeated with the remaining ensemble of particles. Particles with less than  $N_C^{\min}$  neighbors will be treated in a similar manner, since these particles are responsible for merging neighboring clusters.

4. Subsequently we ignore the excluded particles and identify the neighbors once again as described in Step 2, giving disjoint clusters. Then we reintegrate the isolated particles into the set and assign them to the closest clusters. Finally, the following checks are made: (a) does the size of all newly established clusters lie within the range of  $N_C^{\min}$  and  $N_C^{\max}$ , and (b) is the number of identified clusters equal to  $N_l$ ? If either condition is violated, the procedure is iterated with a reduced cut-off radius  $r_c$ .

The success of the improved cluster analysis algorithm becomes apparent from the ensuing cluster population distribution shown in Figure B.2. Peaks due to single particles and merged clusters have vanished, reflecting the correct analysis of the cluster sizes distribution of the system.

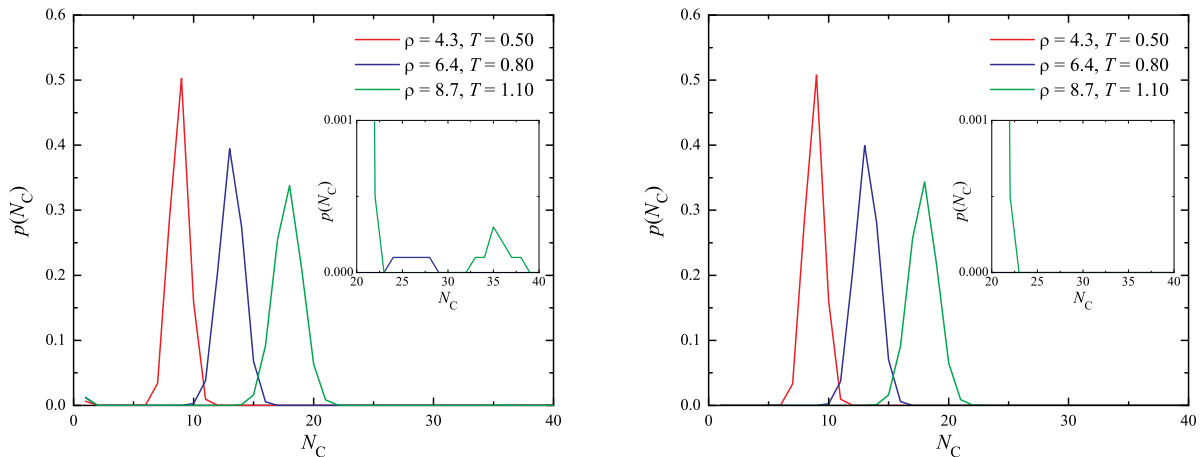


Figure B.2.: Cluster size distribution  $N_C$  for various state points. Left panel: distribution calculated after Step 2 of the cluster analysis algorithm. The inset shows an enlargement of the large- $N_C$  region, revealing the occurrence of merged clusters. Right panel: distribution calculated after Step 4 of the cluster analysis algorithm. The inset reveals the absence of merged clusters.



# C. Experimental Methods

## C.1. Tracer Particles

One molecular dye (Alexa647) and three quantum dots (QD-X) with spherical shape and different sizes were purchased from Invitrogen. Their hydrodynamic radii were measured by fluorescence correlation spectroscopy in ultra dilute (nM) aqueous solutions at ambient temperature. The structural characteristics of the molecular (T1.3) and particle-like (T8.8, T9.2 and T9.8) probes are listed in Table C.1.

Tracers	Alexa647	QD525	QD545	QD585
Code	T1.3	T8.8	T9.2	T9.8
$R_h$ (nm)	1.3	8.8	9.2	9.8
Core	Molecular Dye	CdSe	CdSe	CdSe
Shell	N/A	ZnS	ZnS	ZnS
Coating	N/A	Amphiphilic Polymer (unspecified)	Amphiphilic Polymer (unspecified)	Amphiphilic Polymer (unspecified)
Surface Modification	N/A	Carboxylic groups (c/a 100)	Carboxylic groups (c/a 100)	Carboxylic groups (c/a 100)

Table C.1.: Size and surface characteristics of the fluorescent particles.

## C.2. Preparation of the Inverse Opals

HEPES (Sigma-Aldrich, pH 7.4, concentration 0.01 M) filled inverse colloidal crystals were prepared by codeposition of monodisperse colloidal polystyrene (PS) and silica ( $\text{SiO}_2$ ) nanoparticles (LUDOX SM, Sigma Aldrich) on plasma treated glass slides ( $150 \mu\text{m}$  thickness) [192]. PS particles with a diameter of 180 nm and 130 nm were used in aqueous suspension at a concentration of 1 wt%, the concentration of the silica nanoparticles (radius 7 nm) was adjusted to be 0.3 wt%. Vertical lifting deposition (VLD) was conducted at  $20^\circ\text{C}$ , 50% RH at a lifting speed of 400 nm/s. The samples were deposited on plasma treated glass slides ( $150 \mu\text{m}$  thickness). After VLD, the PS particles were removed by calcination for a few hours in a tube oven at  $450^\circ\text{C}$  in air (heating rate  $\sim 10 \text{ K/min}$ ). Three different i-opals were fabricated

(Table 3.1) for the purpose of the present study: one (iO130-9/11) with nominal cavity diameter 130 nm and two with 180 nm using different methods (codeposition and SolGel) for SiO<sub>2</sub> nanoparticle infiltration into the PS colloidal crystals (iO180-12/15 and iO180-10/15 respectively). Intentionally, the systems iO180-12/15 and iO130-9/11 were designed to provide periodic structures for diffusion through comparable holes but different cavity sizes. Conversely, the samples iO180-12/15 and iO180-10/15 i-opals allow for the study of diffusion in confining periodic structures with the same voids but different hole sizes; the latter sample was prepared by filling the interstitial spaces between the PS particles with SolGel prior to calcination. The SolGel filling led to a reduction of the pore diameter in the iO180-10/15 sample. The i-opal structures were characterized by SEM on a LEO Gemini 1530 microscope (Carl Zeiss AG, Oberkochen, Germany) with acceleration voltage of 1 kV in secondary electrons InLens detection mode. The actual cavity radius  $R$  and the hole diameter  $L$  were obtained from the SEM images as seen in Figure C.1(a) for the iO130-9/11 system. As seen in this Figure, cracks exist between blocks of ordered structure. These can be categorized in large cracks between monoliths of i-opals and smaller internal cracks including point- and line-defects. Whereas the micron sized cracks between monoliths can be assessed by SEM, smaller cracks in the interior of an i-opal cannot be characterized directly.

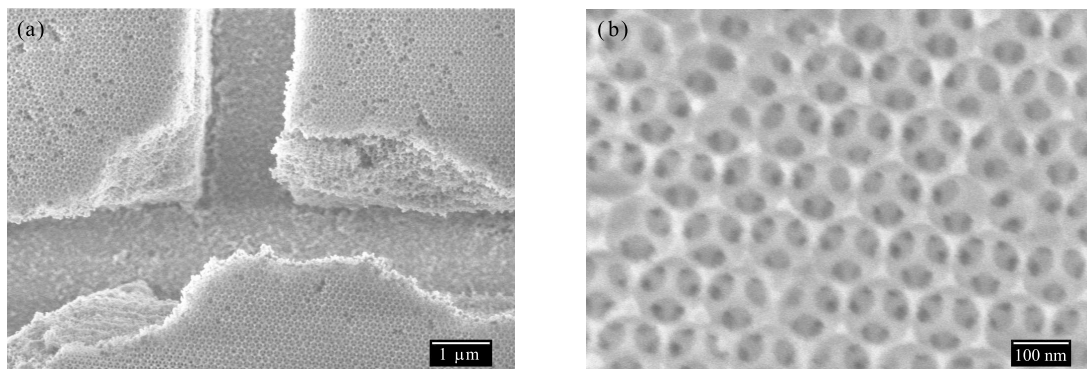


Figure C.1.: Overview (a) and high magnification (b) SEM images for SEM of iO130-9/11.

### C.3. Fluorescence Correlation Spectroscopy

All measurements were performed on a commercial FCS setup [193] (Carl Zeiss, Jena, Germany) consisting of the module, ConfoCor 2, and an inverted microscope, Axiovert 200 model. A 40x Plan Neofluar objective (numerical aperture 1.2; working distance 0.29 mm) and ultrapure water (filtered through a MilliQ purification system, resistivity 18.2 MΩ × cm) as immersion liquid were used. The FCS experiment was concurrently performed with two

tracers using excitation at 488 nm and 633 nm. The emission was collected after splitting the signal by means of a NFT635 dichroic mirror, and filtering with a long-pass LP655 filter for the fluorescence light from the  $\lambda = 633$  nm excitation (channel 1) and with a band pass filter (BP560-615) for the fluorescence light at  $\lambda = 488$  nm excitation (channel 2). Avalanche photodiodes capable of single-photon counting were used for detection. Reusable Attofluor chambers were employed for the measurements. All experiments were conducted at  $21 \pm 1$  °C. In the experiment, the objective's immersion medium was water with refractive index  $n \approx 1.33$ . For the water filled i-opal with a silica ( $n \approx 1.45$ ) filling volume fraction of about 25%, the effective refractive index was  $n \approx 1.36$ . Due to this small  $n$ -mismatch, the estimated error of the diffusion times in the i-opals was less than 10% [194, 195].

Prior to observation, the samples were rinsed with ethanol, dried at room temperature, and mounted in the Attofluor chambers. Then, 600  $\mu$ L of HEPES buffer was added, followed by 150  $\mu$ L of T1.3 and 150  $\mu$ L of the QD, both at 120 nM, in order to achieve comparable concentration for both tracers. It took about 30 min to reach constant fluorescence signal from a homogeneous system. The time-dependent fluctuations of the fluorescent intensity  $\delta I(t)$  were recorded and analyzed by an autocorrelation function  $G(t) = 1 + \langle \delta I(t') \delta I(t' + t) \rangle / \langle I(t') \rangle^2$ . The accumulation time was varied from about 3 min, for diffusion in free solutions, and up to about 10 min, for diffusion in the i-opals. The necessary total accumulation duration was subdivided in 30-seconds intervals in order to enable removal of occasionally spurious signals due to aggregates.

In the FCS experiment, the fluorescent probes were excited by two different lasers,  $\lambda = 633$  nm for T1.3 and  $\lambda = 488$  nm for QDs, leading to slightly different probed volumes as illustrated in Figure C.2. As it has been shown theoretically for an ensemble of identical, freely diffusing fluorescent species, the FCS auto correlation function  $G(t)$  has the following analytical form [101, 102]:

$$G(t) = 1 + \frac{1}{N} \frac{1}{\left(1 + \frac{t}{\tau}\right) \sqrt{1 + \frac{t}{\tau S^2}}}. \quad (\text{C.1})$$

Here,  $N = 1/[G(t = 0) - 1]$  is the average number of species in the observation volume,  $S = z_0/r_0$  is the ratio between longitudinal and transversal dimensions of the observation volume and  $\tau$  is the diffusion time of the species, which is related to their diffusion coefficient,  $D$ , through  $\tau = r_0^2/4D$ . Eq. (C.1) is derived assuming that the fluorescence properties of the diffusing species do not change while they pass through the observation volume. However, this assumption is often not true because various photophysical effects may lead to additional fluctuations in the fluorescence intensity. Two types of photophysical effects applied in this study. For the molecular probe T1.3 (see Table C.1), the dominating effect was the transition

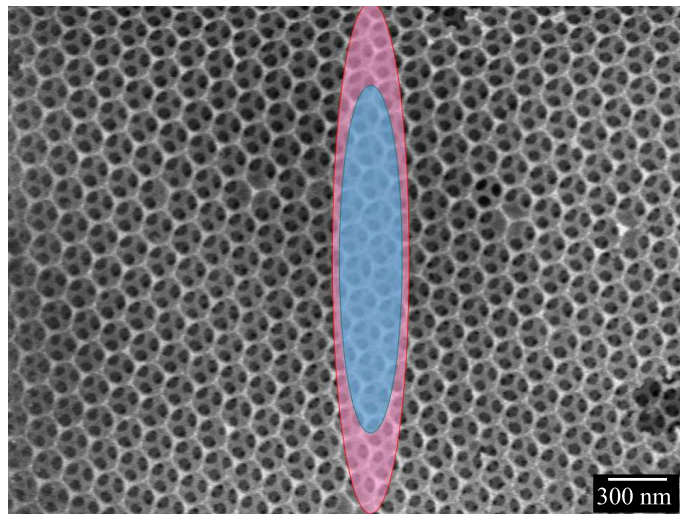


Figure C.2.: Scanning electron microscopy image of the inverse opal (iO180-12/15) (see Table 3.1) along with the observation volumes in the FCS experiment for excitation at the wavelength  $\lambda = 488$  nm (azure) and  $\lambda = 633$  nm (pink) respectively for QD and T1.3.

of the molecule to the first excited triplet state. While staying at this rather long-living state, the molecule appeared dark, an effect that led to fluctuations of the fluorescent intensity, typically at the microsecond time scale. This resulted in an additional exponential decay in the autocorrelation function  $G(t)$ , which modifies to [101, 102]:

$$G(t) = 1 + \left[ 1 + \frac{f_T}{1 - f_T} \exp(-t/\tau_T) \right] \frac{1}{N} \frac{1}{\left(1 + \frac{t}{\tau}\right) \sqrt{1 + \frac{t}{\tau S^2}}}, \quad (\text{C.2})$$

where  $f_T$  and  $\tau_T$  are the fraction and the decay time of the triplet state. Typically  $\tau_T$  is in the order of few  $\mu\text{s}$ . Eq. (C.2) leads to an excellent representation of the experimental  $G(t)$  for T1.3 diffusing either in free aqueous solution or in the i-opals, as seen in Figure C.3 (solid lines).

In the case of QDs, the photophysical effects were different. Instead of triplet kinetics, they exhibited an on-off emission (blinking) with dark times ranging from nanoseconds to seconds [196]. The blinking fluctuations are represented by a power-law time dependence and Eq. (C.1) is now written as [196, 197]:

$$G(t) = 1 + A \left(1 - Bt^{2-m}\right) \frac{1}{N} \frac{1}{\left(1 + \frac{t}{\tau}\right) \sqrt{1 + \frac{t}{\tau S^2}}}, \quad (\text{C.3})$$

where  $A$  describes the overall amplitude of the blinking effect and  $B$  the strength of the power

law dependence with the characteristic exponent  $m$ . Since  $N = A/[G(0) - 1]$  should be invariant of the intrinsic contribution,  $A = 1$  holds. Additionally, since the blinking parameters depend on the QD's structure [196], environment, excitation intensity, and observation time, both  $B > 0$  and  $m$  have to be treated as floating parameters in the fitting procedure of Eq. (C.3) to the experimental  $G(t)$ . As seen in Figure C.3, the latter is very well described by Eq. (C.3) yielding  $m \approx 1.8$ , which is in good agreement with previously reported values [196, 197].

The restricted environment exerted a clear slowdown effect on the center of mass motion for both T1.3 and QDs as shown by the experimental autocorrelation function  $G(t)$  in the iO180-12/15 i-opal (with  $L/R = 12/15$ ) and in the free solution in Figure C.3.

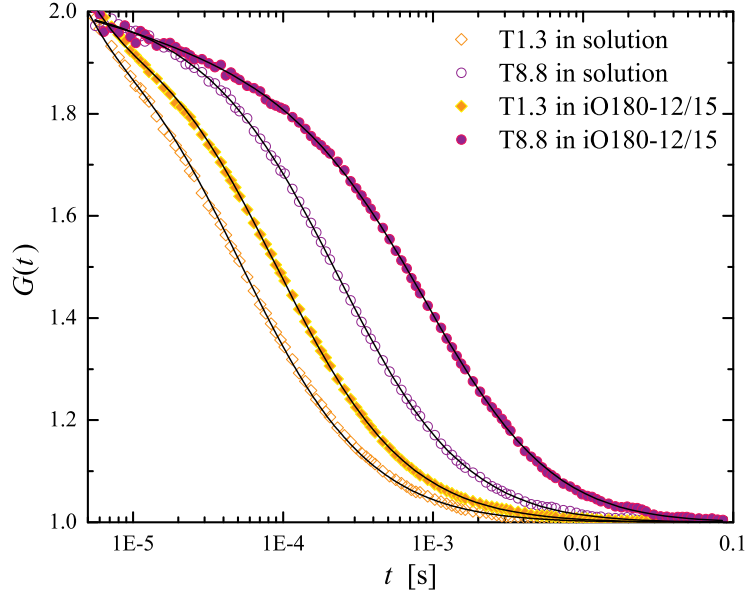


Figure C.3.: Experimental autocorrelation functions  $G(t)$  for the diffusion of the molecular T1.3 and QD T8.8 tracer in the (iO180-12/15) i-opal and in the free aqueous solution. Continuous lines denote the representation of  $G(t)$  by either Eq. (C.2) (for the molecular tracer) or Eq. (C.3) (for the QD), as indicated by the shift of the corresponding  $G(t)$  and the description in the plot.

In the case of the iO130-9/11 i-opal (with  $L/R = 9/11$ ), for which an anomalous diffusion was observed,  $G(t)$  for the QDs can be best fitted by a single non-Fickian process [118] taking into account the blinking effect:

$$G(t) = 1 + (1 - Bt^{2-m}) \frac{1}{N} \frac{1}{\left[1 + \left(\frac{t}{\tau}\right)^\chi\right] \sqrt{1 + \left(\frac{t}{\tau}\right)^\chi \frac{1}{S^2}}}. \quad (\text{C.4})$$

The exponent  $\chi < 1$  denotes a sub-diffusional behavior for the mean-square displacement,

$\langle \Delta \mathbf{r}^2(t) \rangle \sim t^\chi$ . This situation is illustrated in Figure C.4 for the translational motion of T9.8 in free solution and in two i-opals. The shape of  $G(t)$  is clearly broader for the motion of T9.8 in the stronger confining environment of iO130-9/11 with  $a/R \approx 0.18$  than in iO180-10/15 and is well described by Eq. (C.4) with  $\chi < 1$ .

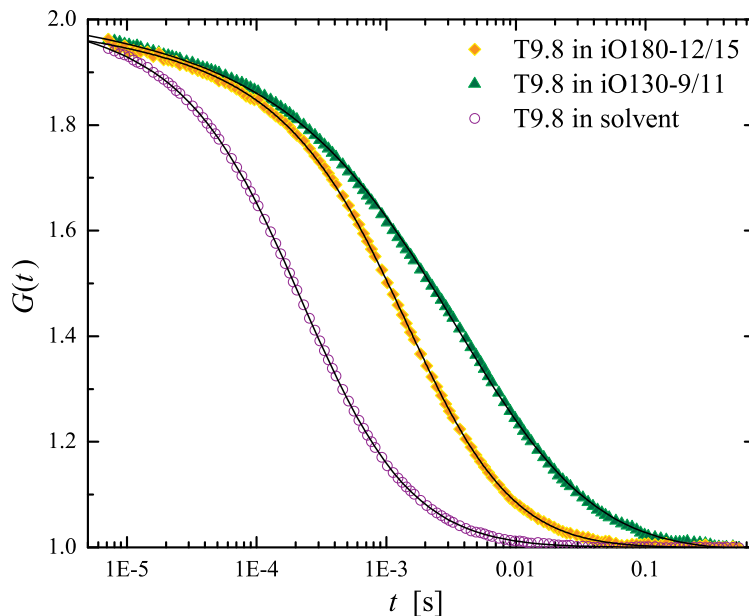


Figure C.4.: Experimental  $G(t)$  for T9.8 in two confining i-opals as opposed to its diffusion in free solution. The solid lines denote the representation of  $G(t)$  by Eq. (C.3) (in free solution and in iO180-12/15) and Eq. (C.4) (in iO130-9/11).

The big cracks mentioned in the previous section regarding the SEM images of Figure C.1, had no effect on the FCS experiment since they were much larger than the focal volume and could be easily recognized and hence avoided. The small internal cracks with typical size ranging from a cavity length scale (completely open cage) up to the observation volume would have caused detectable signal disturbances and would have been detected by scanning different regions in the films. All recorded autocorrelation functions which had been systematically verified, represent structurally coherent regions at least over the lateral dimension ( $\sim 300$  nm) of the observation volume. Furthermore, autocorrelation functions from various spots within the monolithic i-opal regions featured identical decay-curves, which exemplifies the homogeneity of the internal i-opal structure.



# Bibliography

- [1] Hunter, R. *Foundations of colloid science* (Clarendon Press, Oxford, 1986).
- [2] Russel, W. B., Saville, D. A. & Schowalter, W. R. *Colloidal Dispersions* (Cambridge University Press, Cambridge, 1992).
- [3] Higgins, J. S. & Benoît, H. *Polymers and neutron scattering* (Oxford University Press, Oxford, 1997).
- [4] Murray, C. A. & Grier, D. G. Video microscopy of monodisperse colloidal systems. *Annu. Rev. Phys. Chem.* **47**, 421–462 (1996).
- [5] Habdas, P. & Weeks, E. R. Video microscopy of colloidal suspensions and colloidal crystals. *Curr. Opin. Colloid Interface Sci.* **7**, 196203 (2002).
- [6] Crocker, J. C. & Grier, D. G. Methods of digital video microscopy for colloidal studies. *J. Colloid Interface Sci.* **179**, 298–310 (1996).
- [7] Ashkin, A. Acceleration and trapping of particles by radiation pressure. *Phys. Rev. Lett.* **24**, 156–159 (1970).
- [8] Osterman, N., Babic, D., Poberaj, I., Dobnikar, J. & Zihlerl, P. Observation of condensed phases of quasiplanar core-softened colloids. *Phys. Rev. Lett.* **99**, 248301 (2007).
- [9] Grier, D. G. A revolution in optical manipulation. *Nature* **424**, 810–816 (2003).
- [10] Whitesides, G. M. & Stroock, A. Flexible methods for microfluidics. *Phys. Today* **54**, 42–48 (2001).
- [11] Squires, T. M. & Quake, S. R. Microfluidics: Fluid physics at the nanoliter scale. *Rev. Mod. Phys.* **77**, 977–1026 (2005).
- [12] Vermant, J. Large-scale structures in sheared colloidal suspensions. *Curr. Opin. Colloid Interface Sci.* **6**, 489 – 495 (2001).
- [13] Woodcock, L. V. Origins of thixotropy. *Phys. Rev. Lett.* **54**, 1513 – 1516 (1985).
- [14] Wagner, N. J. & Brady, J. F. Shear thickening in colloidal dispersions. *Physics Today* **62** (10), 27 – 32 (2009).
- [15] Erwin, B. M., Vlassopoulos, D. & Cloître, M. Rheological fingerprinting of an aging soft colloidal glass. *J. Rheol.* **54**, 915 – 939 (2010).
- [16] Osuji, C. O. & Weitz, D. A. Highly anisotropic vorticity aligned structures in a shear thickening attractive colloidal system. *Soft Matter* **4**, 1388 (2008).

- [17] Chremos, A., Margaritis, K. & Panagiotopoulos, A. Z. Ultra thin films of diblock copolymers under shear. *Soft Matter* **6**, 3588 – 3595 (2010).
- [18] Davies, T. S., Ketner, A. M. & Raghavan, S. R. Self-assembly of surfactant vesicles that transform into viscoelastic wormlike micelles upon heating. *J. Am. Chem. Soc.* **128**, 6669 – 6675 (2006).
- [19] Laun, H. M., Bung, R. & Schmidt, F. Rheology of extremely shear thickening polymer dispersions (passively viscosity switching fluids). *J. Rheol.* **35**, 999 – 1034 (1991).
- [20] Lee, Y. S., Wetzal, E. D. & Wagner, N. J. The ballistic impact characteristics of kevlar (r) woven fabrics impregnated with a colloidal shear thickening fluid. *J. Mater. Sci.* **38**, 2825 – 2833 (2003).
- [21] Pan, W., Fedosov, D. A., Caswell, B. & Karniadakis, G. E. Predicting dynamics and rheology of blood flow: A comparative study of multiscale and low-dimensional models of red blood cells. *Microvasc. Res.* **82**, 163–170 (2011).
- [22] McMillan, W. G. & Mayer, J. E. The statistical thermodynamics of multicomponent systems. *J. Chem. Phys.* **13**, 276–305 (1945).
- [23] Kirkwood, J. G. & Buff, F. P. The statistical mechanical theory of solutions. i. *J. Chem. Phys.* **19**, 774–777 (1951).
- [24] Likos, C. N. Effective interactions in soft condensed matter physics. *Phys. Rep.* **348**, 267 – 439 (2001).
- [25] Likos, C. N. *et al.* Star polymers viewed as ultrasoft colloidal particles. *Phys. Rev. Lett.* **80**, 4450–4453 (1998).
- [26] Denton, A. R. Counterion penetration and effective electrostatic interactions in solutions of polyelectrolyte stars and microgels. *Phys. Rev. E* **67**, 011804 (2003).
- [27] Denton, A. R. Erratum: Counterion penetration and effective electrostatic interactions in solutions of polyelectrolyte stars and microgels. *Phys. Rev. E* **67**, 049904 (2003).
- [28] Mladek, B. M., Kahl, G. & Likos, C. N. Computer assembly of cluster-forming amphiphilic dendrimers. *Phys. Rev. Lett.* **100**, 028301 (2008).
- [29] Lenz, D. A., Mladek, B. M., Likos, C. N., Kahl, G. & Blaak, R. Monomer-resolved simulations of cluster-forming dendrimers. *J. Phys. Chem. B* **115**, 7218–7226 (2011).
- [30] Doi, M. & Edwards, S. F. *The Theory of Polymer Dynamics* (Clarendon Press, 1999).
- [31] Ermak, D. L. Brownian dynamics techniques and their application to dilute solutions. *Rapport d'activité scientifique du CECAM* **1**, 66–81 (1976).
- [32] Ermak, D. L. & McCammon, J. A. Brownian dynamics with hydrodynamic interactions. *J. Chem. Phys.* **69**, 1352–1360 (1978).



- 
- [33] Ermak, D. & Buckholtz, H. Numerical integration of the langevin equation: Monte carlo simulation. *Journal of Computational Physics* **35**, 169–182 (1980).
- [34] Elber, R. *Recent Developments In Theoretical Studies Of Proteins* (World Scientific, London, 1996).
- [35] Hecht, M., Harting, J., Ihle, T. & Herrmann, H. J. Simulation of claylike colloids. *Phys. Rev. E* **72**, 011408 (2005).
- [36] Hecht, M., Harting, J., Bier, M., Reinshagen, J. & Herrmann, H. J. Shear viscosity of claylike colloids in computer simulations and experiments. *Phys. Rev. E* **74**, 021403 (2006).
- [37] Wysocki, A. *et al.* Multi-particle collision dynamics simulations of sedimenting colloidal dispersions in confinement. *Faraday Discuss.* **144**, 245252 (2010).
- [38] Malevanets, A. & Yeomans, J. M. Dynamics of short polymer chains in solution. *Europhys. Lett.* **52**, 231–237 (2000).
- [39] Mussawisade, K., Ripoll, M., Winkler, R. G. & Gompper, G. Dynamics of polymers in a particle-based mesoscopic solvent. *J. Chem. Phys.* **123**, 144905 (2005).
- [40] Padding, J. T., Wysocki, A., Lowen, H. & Louis, A. A. Stick boundary conditions and rotational velocity auto-correlation functions for colloidal particles in a coarse-grained representation of the solvent. *J. Phys.: Condens. Matter* **17**, S3393–S3399 (2005).
- [41] Padding, J. T. & Louis, A. A. Hydrodynamic interactions and brownian forces in colloidal suspensions: Coarse-graining over time and length scales. *Phys. Rev. E* **74**, 031402 (2006).
- [42] Ripoll, M., Winkler, R. G. & Gompper, G. Star polymers in shear flow. *Phys. Rev. Lett.* **96**, 188302 (2006).
- [43] Ripoll, M., Winkler, R. G. & Gompper, G. Hydrodynamic screening of star polymers in shear flow. *Eur. Phys. J. E* **23**, 349–354 (2007).
- [44] Nikoubashman, A. & Likos, C. N. Branched polymers under shear. *Macromolecules* **43**, 1610–1620 (2010).
- [45] Hoogerbrugge, P. J. & Koelman, J. M. V. A. Simulating microscopic hydrodynamic phenomena with dissipative particle dynamics. *Europhys. Lett.* **19**, 155–160 (1992).
- [46] Español, P. Hydrodynamics from dissipative particle dynamics. *Phys. Rev. E* **52**, 1734–1742 (1995).
- [47] Español, P. & Warren, P. Statistical mechanics of dissipative particle dynamics. *Europhys. Lett.* **30**, 191–196 (1995).
- [48] McNamara, G. R. & Zanetti, G. Use of the boltzmann equation to simulate lattice-gas automata. *Phys. Rev. Lett.* **61**, 2332–2335 (1988).

- [49] Shan, X. & Chen, H. Lattice boltzmann model for simulating flows with multiple phases and components. *Phys. Rev. E* **47**, 1815–1819 (1993).
- [50] He, X. & Luo, L. S. Theory of the lattice boltzmann method: From the boltzmann equation to the lattice boltzmann equation. *Phys. Rev. E* **56**, 6811–6817 (1997).
- [51] Malevanets, A. & Kapral, R. Mesoscopic model for solvent dynamics. *J. Chem. Phys.* **110**, 8605–8613 (1999).
- [52] Malevanets, A. & Kapral, R. Solute molecular dynamics in a mesoscale solvent. *J. Chem. Phys.* **112**, 7260–7269 (2000).
- [53] Gompper, G., Ihle, T., Kroll, D. M. & Winkler, R. G. Multi-particle collision dynamics – a particle-based mesoscale simulation approach to the hydrodynamics of complex fluids. *Adv. Polym. Sci.* **221**, 1 (2009).
- [54] Ihle, T. & Kroll, D. M. Stochastic rotation dynamics. i. formalism, galilean invariance, and green-kubo relations. *Phys. Rev. E* **67**, 066705 (2003).
- [55] Marsaglia, G. Choosing a point from the surface of a sphere. *The Annals of Mathematical Statistics* **43**, 645–646 (1972).
- [56] Ihle, T. & Kroll, D. M. Stochastic rotation dynamics: A galilean-invariant mesoscopic model for fluid flow. *Phys. Rev. E* **63**, 020201 (2001).
- [57] Lamura, A., Gompper, G., Ihle, T. & Kroll, D. M. Multi-particle collision dynamics: Flow around a circular and a square cylinder. *Europhys. Lett.* **56**, 319–325 (2001).
- [58] Allahyarov, E. & Gompper, G. Mesoscopic solvent simulations: Multiparticle-collision dynamics of three-dimensional flows. *Phys. Rev. E* **66**, 036702 (2002).
- [59] Evans, D. J. & Morriss, G. *Statistical Mechanics of Nonequilibrium Liquids* (Cambridge University Press, 2008).
- [60] Lees, A. W. & Edwards, S. F. The computer study of transport processes under extreme conditions. *Journal of Physics C: Solid State Physics* **5**, 1921 (1972).
- [61] Nikoubashman, A., Kahl, G. & Likos, C. N. Cluster crystals under shear. *Phys. Rev. Lett.* **107**, 068302 (2011).
- [62] Tropea, C., Foss, J. F. & Yarin, A. (eds.) *Handbook of Experimental Fluid Dynamics* (Springer, 2005).
- [63] Inoue, Y., Chen, Y. & Ohashi, H. Development of a simulation model for solid objects suspended in a fluctuating fluid. *J. Stat. Phys.* **107**, 85–100 (2002).
- [64] H., S. Über polymerisation. *Ber. Deut. Chem. Ges.* **53**, 1073–1085 (1920).
- [65] Staudinger, H. Viscosity investigations for the examination of the constitution of natural products of high molecular weight and of rubber and cellulose. *Trans. Faraday Soc.* **29**, 18–32 (1933).

- 
- [66] Newkome, G. R., Moorefield, C. N. & Vögtle, F. *Dendritic Molecules: Concepts, Syntheses, Perspectives* (Wiley-VCH, 1996).
- [67] Buhleier, E., Wehner, W. & Vögtle, F. “cascade”- and “nonskid-chain-like” syntheses of molecular cavity topologies. *Synthesis* **2**, 155–158 (1978).
- [68] Tomalia, D. A., Naylor, A. M. & Goddard, W. A. Starburst dendrimers: Molecular-level control of size, shape, surface chemistry, topology, and flexibility from atoms to macroscopic matter. *Angewandte Chemie International Edition* **29**, 138–175 (1990).
- [69] W, C. A monte carlo study of model dendrimers. *J. Chem. Trans. Faraday Soc.* **92**, 4151–4154 (1996).
- [70] Boris, D. & Rubinstein, M. A self-consistent mean field model of a starburst dendrimer: dense core vs dense shell. *Macromolecules* **29**, 7251–7260 (1996).
- [71] Hammouda, B. The structure factor for starburst dendrimers. *J. Polym. Sci. Part B* **30**, 1387–1390 (1992).
- [72] de Gennes, P. & Hervet, H. Statistics of starburst polymers. *Journal de Physique Lettres* **44**, 351–360 (1983).
- [73] Ballauff, M. & Likos, C. N. Dendrimers in solution: Insight from theory and simulation. *Angewandte Chemie International Edition* **43**, 2998–3020 (2004).
- [74] Nisato, G., Ivkov, R. & Amis, E. J. Size invariance of polyelectrolyte dendrimers. *Macromolecules* **33**, 4172–4176 (2000).
- [75] Welch, P. & Muthukumar, M. Dendrimer-polyelectrolyte complexation: A model guest-host system. *Macromolecules* **33**, 6159–6167 (2000).
- [76] Blaak, R., Lehmann, S. & Likos, C. N. Charge-induced conformational changes of dendrimers. *Macromolecules* **41**, 4452–4458 (2008).
- [77] Lee, I., Athey, B. D., Wetzel, A. W., Meixner, W. & Baker, J. R. Structural molecular dynamics studies on polyamidoamine dendrimers for a therapeutic application: Effects of pH and generation. *Macromolecules* **35**, 4510–4520 (2002).
- [78] Nikoubashman, A. & Likos, C. N. Flow-induced polymer translocation through narrow and patterned channels. *J. Chem. Phys.* **133**, 074901 (2010).
- [79] Grest, G. S., Kremer, K. & Witten, T. A. Structure of many arm star polymers: a molecular dynamics simulation. *Macromolecules* **20**, 1376–1383 (1987).
- [80] Stillinger, F. H. Phase transition in the gaussian core system. *J. Chem. Phys.* **65**, 3968–3974 (1976).
- [81] Likos, C. N., Lang, A., Watzlawek, M. & Löwen, H. Criterion for determining clustering versus reentrant melting behavior for bounded interaction potentials. *Phys. Rev. E* **63**, 031206 (2001).

- [82] Likos, C. N., Mladek, B. M., Gottwald, D. & Kahl, G. Why do ultrasoft repulsive particles cluster and crystallize? analytical results from density-functional theory. *J. Chem. Phys.* **126**, 224502 (2007).
- [83] Mladek, B. M., Gottwald, D., Kahl, G., Neumann, M. & Likos, C. N. Clustering in the absence of attractions: density functional theory and computer simulations. *J. Phys. Chem. B* **111**, 12799 – 12808 (2007).
- [84] Rubinstein, M. & Colby, R. H. *Polymer Dynamics* (Oxford University Press, USA, 2003).
- [85] Lebold, T., Jung, C., Michaelis, J. & Bräuchle, C. Nanostructured silica materials as drug-delivery systems for doxorubicin: Single molecule and cellular studies. *Nanoletters* **9**, 2877 (2009).
- [86] Yang, S. Y. *et al.* Single-file diffusion of protein drugs through cylindrical nanochannels. *ACS Nano* **4**, 3817–3822 (2010).
- [87] Shao, Z. & Haile, S. A high-performance cathode for the next generation of solid oxide fuel cells. *Nature* **431**, 170–173 (2004).
- [88] Jackson, E. A. & Hillmyer, M. A. Nanoporous membranes derived from block copolymers: From drug delivery to water filtration. *ACS Nano* **4**, 3548–3553 (2010).
- [89] Volkmuth, W. D. & Austin, R. H. Dna electrophoresis in microlithographic arrays. *Nature* **358**, 600–602 (1992).
- [90] Han, J. & Craighead, H. G. Separation of long dna molecules in a microfabricated entropic trap array. *Science* **288**, 1026–1029 (2000).
- [91] Wei, Q., Bechinger, C. & Leiderer, P. Single-file diffusion of colloids in one-dimensional channels. *Science* **287**, 625–627 (2000).
- [92] Wang, B., Anthony, S. M., Bae, S. C. & Granick, S. Anomalous yet brownian. *Proc. Natl. Acad. Sci.* **106**, 15160–15164 (2009).
- [93] Fakhri, N., MacKintosh, F. C., Lounis, B., Cognet, L. & Pasquali, M. Brownian motion of stiff filaments in a crowded environment. *Science* **330**, 1804–1807 (2010).
- [94] Nykypanchuk, D., Strey, H. H. & Hoagland, D. A. Brownian motion of dna confined within a two-dimensional array. *Science* **297**, 987–990 (2002).
- [95] Park, S., Park, I., Chang, T. & Ryu, C. Y. Interaction-controlled hplc for block copolymer analysis and separation. *J. Am. Chem. Soc.* **126**, 8906–8907 (2004).
- [96] Striemer, C. C., Gaborski, T. R., McGrath, J. L. & Fauchet, P. Charge- and size-based separation of macromolecules using ultrathin silicon membranes. *Nature* **445**, 749–753 (2007).

- 
- [97] Retan, N. K., Juthajan, A., Lindmo, T. & de Lange Davies, C. Macromolecular diffusion in the extracellular matrix measured by fluorescence correlation spectroscopy. *J. Biomedical Optics* **13**, 054040 (2008).
- [98] Cherdhirankorn, T. *et al.* Fluorescence correlation spectroscopy study of molecular probe diffusion in polymer melts. *Macromolecules* **42**, 4858–4866 (2009).
- [99] Fu, Y., Ye, F., Sanders, W. G., Collinson, M. M. & Higgins, D. A. Single molecule spectroscopy studies of diffusion in mesoporous silica thin films. *J. Phys. Chem. B* **110**, 9164–9170 (2006).
- [100] Kirstein, J. *et al.* Exploration of nanostructured channel systems by single molecule probes. *Nat. Mater.* **6**, 303 (2007).
- [101] Rigler, R. & Elson, E. S. *Fluorescence Correlation Spectroscopy* (Springer, 2001).
- [102] Haustein, E. & Schwille, P. Ultrasensitive investigations of biological systems by fluorescence correlation. *Methods* **29**, 153–166 (2003).
- [103] Lumma, D., Keller, S., Vilgis, T. & Radler, J. O. Dynamics of large semiflexible chains probed by fluorescence correlation spectroscopy. *Phys. Rev. Lett.* **90**, 218301 (2003).
- [104] Zhao, J. & Granick, S. How polymer surface diffusion depends on surface coverage. *Macromolecules* **40**, 1243–1247 (2007).
- [105] Sia, S. K. & Whitesides, G. M. Microfluidic devices fabricated in poly(dimethylsiloxane) for biological studies. *Electrophoresis* **24**, 3563 (2003).
- [106] Branton, D. *et al.* The potential and challenges of nanopore sequencing. *Nat. Biotech.* **26**, 1146–1153 (2008).
- [107] Zwolak, M. & Di Ventra, M. Colloquium: Physical approaches to dna sequencing and detection. *Rev. Mod. Phys.* **80**, 141–165 (2008).
- [108] Kasianowicz, J. J., Brandin, E., Branton, D. & Deamer, D. W. Characterization of individual polynucleotide molecules using a membrane channel. *Proc. Natl. Acad. Sci. USA* **93**, 13770–13773 (1996).
- [109] Milchev, A., Binder, K. & Bhattacharya, A. Polymer translocation through a nanopore induced by adsorption: Monte carlo simulation of a coarse-grained model. *J. Chem. Phys.* **121**, 6042 (2004).
- [110] Sung, W. & Park, P. J. Polymer translocation through a pore in a membrane. *Phys. Rev. Lett.* **77**, 783–786 (1996).
- [111] Muthukumar, M. Polymer translocation through a hole. *J. Chem. Phys.* **111**, 10371–10374 (1999).
- [112] Muthukumar, M. Translocation of a confined polymer through a hole. *Phys. Rev. Lett.* **86**, 3188–3191 (2001).

- [113] Muthukumar, M. Polymer escape through a nanopore. *J. Chem. Phys.* **118**, 5174–5184 (2003).
- [114] Park, P. J. & Sung, W. Polymer translocation induced by adsorption. *J. Chem. Phys.* **108**, 3013–3018 (1998).
- [115] Hohlbein, J. *et al.* Confined diffusion in ordered nanoporous alumina membranes. *Small* **3**, 380–385 (2007).
- [116] Sato, A. *et al.* Tuning and switching the hypersonic phononic properties of elastic impedance contrast nanocomposites. *ACS Nano* **4**, 3471–3481 (2010).
- [117] Cherdhirankorn, T., Retsch, M., Jonas, U., Butt, H. J. & Koynov, K. Tracer diffusion in silica inverse opals. *Langmuir* **26**, 10141–10146 (2010).
- [118] Fatin-Rouge, N., Starchev, K. & Buffle, J. Size effects on diffusion processes within agarose gels. *Biophys. J.* **86**, 2710–2719 (2004).
- [119] Wong, I. Y. *et al.* Anomalous diffusion probes microstructure dynamics of entangled f-actin networks. *Phys. Rev. Lett.* **92**, 178101 (2004).
- [120] Saxton, M. J. A biological interpretation of transient anomalous subdiffusion. i. qualitative model. *Biophys. J.* **92**, 1178–1191 (2007).
- [121] Bouchaud, J.-P. & Georges, A. Anomalous diffusion in disordered media: Statistical mechanisms, models and physical applications. *Phys. Rep.* **195**, 127–293 (1990).
- [122] Paul, W. & Baschnagel, J. *Stochastic Processes. From Physics to Finance* (Springer, 1999).
- [123] Rutherford, S. E., Chadwick, J. & Ellis, C. *Radiations from Radioactive Substances* (Cambridge University Press, 1930).
- [124] Cannizzaro, F., Greco, G., Rizzo, S. & Sinagra, E. Results of the measurements carried out in order to verify the validity of the poisson-exponential distribution in radioactive decay events. *Int. J. Appl. Radiat. Is.* **29**, 649–652 (1978).
- [125] Di Marzio, E. A. & Mandell, A. J. Phase transition behavior of a linear macromolecule threading a membrane. *J. Chem. Phys.* **107**, 5510–5514 (1997).
- [126] Chuang, J., Kantor, Y. & Kardar, M. Anomalous dynamics of translocation. *Phys. Rev. E* **65**, 011802 (2001).
- [127] Klein Wolterink, J., Barkema, G. T. & Panja, D. Passage times for unbiased polymer translocation through a narrow pore. *Phys. Rev. Lett.* **96**, 208301 (2006).
- [128] Sakaue, T., Raphaël, E., de Gennes, P.-G. & Brochard-Wyart, F. Flow injection of branched polymers inside nanopores. *Europhys. Lett.* **72**, 83 (2005).
- [129] de Gennes, P. G. *Scaling Concepts in Polymer Physics* (Cornell University Press, 1979).



- 
- [130] Götze, I. O. & Likos, C. N. Conformations of flexible dendrimers: a simulation study. *Macromolecules* **36**, 8189–8197 (2003).
- [131] Likos, C. N. *et al.* Gaussian effective interaction between flexible dendrimers of fourth generation: a theoretical and experimental study. *J. Chem. Phys.* **117**, 1869–1877 (2002).
- [132] Harreis, H. M., Likos, C. N. & Ballauff, M. Can dendrimers be viewed as compact colloids? a simulation study of the fluctuations in a dendrimer of fourth generation. *J. Chem. Phys.* **118**, 1979–1988 (2003).
- [133] de Gennes, P. G. Flexible polymers in nanopores. *Adv. Polym. Sci.* **138**, 91–105 (1999).
- [134] Gay, C., de Gennes, P. G., Raphael, E. & Brochard-Wyart, F. Injection threshold for a statistically branched polymer inside a nanopore. *Macromolecules* **29**, 8379–8382 (1996).
- [135] Markesteijn, A. P., Usta, O. B., Ali, I., Balazs, A. C. & Yeomans, J. M. Flow injection of polymers into nanopores. *Soft Matter* **5**, 4575–4579 (2009).
- [136] Kraus, M., Wintz, W., Seifert, U. & Lipowsky, R. Fluid vesicles in shear flow. *Phys. Rev. Lett.* **77**, 3685–3688 (1996).
- [137] Chen, Y.-L., Ma, H., Graham, M. D. & de Pablo, J. J. Modeling dna in confinement: A comparison between the brownian dynamics and lattice boltzmann method. *Macromolecules* **40**, 5978 (2007).
- [138] Smith, M. B., McGillivray, D. J., Genzer, J., Lösche, M. & Kilpatrick, P. K. Neutron reflectometry of supported hybrid bilayers with inserted peptide. *Soft Matter* **6**, 862 (2010).
- [139] Wu, C. J., Söderlind, P., Glosli, J. N. & Klepeis, J. E. Shear-induced anisotropic plastic flow from body-centred-cubic tantalum before melting. *Nat. Mater.* **8**, 223 – 228 (2009).
- [140] Ackerson, B. J. & Clark, N. A. Shear-induced melting. *Phys. Rev. Lett.* **46**, 123 – 127 (1981).
- [141] Ackerson, B. J. & Clark, N. A. Shear-induced partial translation ordering of a colloidal solid. *Phys. Rev. A* **30**, 906 – 919 (1984).
- [142] Ackerson, B. J., Hayter, J. B., Clark, N. A. & Cotter, L. Neutron scattering from charge stabilized suspensions undergoing shear. *J. Chem. Phys.* **84**, 2344 – 2349 (1986).
- [143] Vermant, J. & Solomon, M. J. Flow-induced structure in colloidal suspensions. *J. Phys.: Condens. Matter* **17**, R187 – R216 (2005).
- [144] Chen, L. B. & Zukoski, C. F. Discontinuous shear thinning in ordered suspensions. *Phys. Rev. Lett.* **65**, 44 – 47 (1990).

- [145] Yan, Y. D. & Dhont, J. K. G. Shear-induced structure distortion in nonaqueous dispersions of charged colloidal spheres via light scattering. *Physica A* **198**, 78 – 107 (1993).
- [146] Chen, L. B., Chow, M. K., Ackerson, B. J. & Zukoski, C. F. Rheological and microstructural transitions in colloidal crystals. *Langmuir* **10**, 2817 – 2829 (1994).
- [147] Chen, L. B., Ackerson, B. J. & Zukoski, C. F. Rheological consequences of microstructural transitions in colloidal crystals. *J. Rheol.* **38**, 193 – 216 (1994).
- [148] Imhof, A., van Blaaderen, A. & Dhont, J. K. G. Shear melting of colloidal crystals of charged spheres studied with rheology and polarizing microscopy. *Langmuir* **10**, 3477 – 3484 (1994).
- [149] Derks, D., Wisman, H., van Blaaderen, A. & Imhof, A. Confocal microscopy of colloidal dispersions in shear flow using a counter-rotating coneplate shear cell. *J. Phys.: Condens. Matter* **16**, S3917 – S3927 (2004).
- [150] Derks, D., Wu, Y. L., van Blaaderen, A. & Imhof, A. Dynamics of colloidal crystals in shear flow. *Soft Matter* **5**, 1060 – 1065 (2009).
- [151] Wu, Y. L., Derks, D., van Blaaderen, A. & Imhof, A. Melting and crystallization of colloidal hard-sphere suspensions under shear. *Proc. Natl. Acad. Sci. USA* **106**, 10564 – 10569 (2009).
- [152] Butler, S. & Harrowell, P. The shear induced disordering transition in a colloidal crystal: Nonequilibrium brownian dynamic simulations. *J. Chem. Phys.* **103**, 4653 – 4671 (1995).
- [153] Willner, L. *et al.* Structural investigation of star polymers in solution by small angle neutron scattering. *Macromolecules* **27**, 3821 (1994).
- [154] Vlassopoulos, D., Fytas, G., Pakula, T. & Roovers, J. Multiarm star polymer dynamics. *J. Phys.: Condens. Matter* **13**, R855 (2001).
- [155] Foffi, G. *et al.* Structural arrest in dense star-polymer solutions. *Phys. Rev. Lett.* **90**, 238301 (2003).
- [156] Laurati, M. *et al.* Starlike micelles with starlike interactions: a quantitative evaluation of structure factors and phase diagram. *Phys. Rev. Lett.* **94**, 195504 (2005).
- [157] Stiakakis, E., Wilk, A., Kohlbrecher, J., Vlassopoulos, D. & Petekidis, G. Slow dynamics, aging, and crystallization in multiarm star glasses. *Phys. Rev. E* **81**, 020402(R) (2010).
- [158] Mortensen, K., Brown, W. & Nordén, B. Inverse melting transition and evidence of three-dimensional cubatic structure in a block-copolymer micellar system. *Phys. Rev. Lett.* **68**, 2340 (1992).



- 
- [159] Smay, J. E., Gratson, G. M., Shepherd, R. F., Cesarano III, J. & Lewis, J. A. Directed colloidal assembly of 3d periodic structures. *Adv. Mater.* **14**, 1279 (2002).
- [160] Smay, J. E., Cesarano III, J. & Lewis, J. A. Colloidal inks for directed assembly of 3-d periodic structures. *Langmuir* **18**, 5429 (2002).
- [161] Yi, G.-R. *et al.* Generation of uniform colloidal assemblies in soft microfluidic devices. *Adv. Mater.* **15**, 1300 (2003).
- [162] Rao, R. B., Krafcik, K. L., Morales, A. M. & Lewis, J. A. Microfabricated deposition nozzles for direct-write assembly of three-dimensional periodic structures. *Adv. Mater.* **17**, 289 (2005).
- [163] Shepherd, R. F. *et al.* Microfluidic assembly of homogeneous and janus colloid-filled hydrogel granules. *Langmuir* **22**, 8618 (2006).
- [164] Shah, R. K., Kim, J.-W., Argenti, J. J., Weitz, D. A. & Chu, L.-Y. Fabrication of monodisperse thermosensitive microgels and gel capsules in microfluidic devices. *Soft Matter* **4**, 2303 (2008).
- [165] Dendukuri, D. & Doyle, P. S. The synthesis and assembly of polymeric microparticles using microfluidics. *Adv. Mater.* **21**, 1 (2009).
- [166] Seiffert, S. & Weitz, D. A. Controlled fabrication of polymer microgels by polymer-analogous gelation in droplet microfluidics. *Soft Matter* **6**, 3184 (2010).
- [167] Chen, H., Li, J., Shum, H. C., Stone, H. A. & Weitz, D. A. Breakup of double emulsions in constrictions. *Soft Matter* **7**, 2345 (2011).
- [168] Wyss, H. M., Franke, T., Mele, E. & Weitz, D. A. Capillary micromechanics: measuring the elasticity of microscopic soft objects. *Soft Matter* **6**, 4550 (2010).
- [169] Terray, A., Oakey, J. & Marr, D. Microfluidic control using colloidal devices. *Science* **296**, 1841 (2002).
- [170] Karlsson, R. *et al.* Moving-wall driven flows in nanofluidic systems. *Langmuir* **18**, 4186 (2002).
- [171] Roberts, M. T., Mohraz, A., Christensen, K. T. & Lewis, J. A. Direct flow visualization of colloidal gels in microfluidic channels. *Langmuir* **23**, 8726 (2007).
- [172] Conrad, J. C. & Lewis, J. A. Structure of colloidal gels during microchannel flow. *Langmuir* **24**, 7628 (2008).
- [173] Conrad, J. C. & Lewis, J. A. Structural evolution of colloidal gels during constricted microchannel flow. *Langmuir* **26**, 6102 (2010).
- [174] Walls, H. J., Brett Caines, S., Sanchez, A. M. & Khan, S. A. Yield stress and wall slip phenomena in colloidal silica gels. *J. Rheol.* **47**, 847 (2003).

- [175] Haw, M. D. Jamming, two-fluid behavior and self-filtration in concentrated particulate suspensions. *Phys. Rev. Lett.* **92**, 185506 (2004).
- [176] Isa, L., Besseling, R. & Poon, W. Shear zones and wall slip in the capillary flow of concentrated colloidal suspensions. *Phys. Rev. Lett.* **98**, 198305 (2007).
- [177] Isa, L., Besseling, R., Morozov, A. N. & Poon, W. Velocity oscillations in microfluidic flows of concentrated colloidal suspensions. *Phys. Rev. Lett.* **102**, 058302 (2009).
- [178] Campbell, A. I. & Haw, M. D. Jamming and unjamming of concentrated colloidal dispersions in channel flows. *Soft Matter* **6**, 4688 (2010).
- [179] Genovese, D. & Sparkel, J. Crystallization and intermittent dynamics of constricted microfluidic flows of dense suspensions. *Soft Matter* **7**, 3889 (2011).
- [180] Bastea, S. Transport in a highly asymmetric binary mixture. *Phys. Rev. E* **75**, 031201 (2007).
- [181] Mankoc, C., Garcimartín, A., Zuriguel, I. & Maza, D. Role of vibrations in the jamming and unjamming of grains discharging in a silo. *Phys. Rev. E* **80**, 011309 (2009).
- [182] Kulkarni, S. D., Metzger, B. & Morris, J. F. Particle-pressure-induced self-filtration in concentrated suspensions. *Phys. Rev. E* **82**, 010402 (2010).
- [183] Cates, M. E., Wittmer, J. P., Bouchaud, J.-P. & Claudin, P. Jamming, force chains, and fragile matter. *Phys. Rev. Lett.* **81**, 1841 (1998).
- [184] van Teeffelen, S., Moreno, A. J. & Likos, C. N. Cluster crystals in confinement. *Soft Matter* **5**, 1024 – 1038 (2009).
- [185] Blaak, R., Auer, S., Frenkel, D. & Löwen, H. Crystal nucleation of colloidal suspensions under shear. *Phys. Rev. Lett.* **93**, 068303 (2004).
- [186] Coslovich, D., Strauss, L. & Kahl, G. Hopping and microscopic dynamics of ultrasoft particles in cluster crystals. *Soft Matter* **7**, 2127 – 2137 (2011).
- [187] Herschel, W. H. & Bulkley, R. Konsistenzmessungen von gummi-benzollösungen. *Kolloid-Z.* **39**, 291 (1926).
- [188] Steinhardt, P. J., Nelson, D. R. & Ronchetti, M. Bond-orientational order in liquids and glasses. *Phys. Rev. B* **28**, 784–805 (1983).
- [189] Landau, L. & Lifschitz, E. *Quantum Mechanics* (Pergamon, London, 1965).
- [190] Lechner, W. & Dellago, C. Accurate determination of crystal structures based on averaged local bond order parameters. *J. Chem. Phys.* **129**, 114707 (2008).
- [191] Mladek, B. *Exotic phenomena in the phase behaviour of soft matter systems*. Ph.D. thesis, Vienna University of Technology (2007).

- [192] Li, Q., Retsch, M., Wang, J. J., Knoll, W. G. & Jonas, U. Porous networks through colloidal templates. *Top. Curr. Chem.* **287**, 135–180 (2009).
- [193] Cherdhirankorn, T., Koynov, K., Peneva, K., Muellen, K. & Fytas, G. Fluorescence correlation spectroscopy studies of tracer diffusion in polystyrene solutions. *J. Phys. Chem. B* **113**, 3355–3359 (2009).
- [194] Enderlein, J., Gregor, I., Patra, D. & Fitter, J. Art and artefacts of fluorescence correlation spectroscopy. *Curr. Pharm. Biotechnol.* **5**, 155–161 (2004).
- [195] Wang, J., Li, Q., Knoll, W. & Jonas, U. Preparation of multilayered trimodal colloid crystals and binary inverse opals. *J. Am. Chem. Soc.* **128**, 15606–15607 (2006).
- [196] Stefani, F. D., Hoogenboom, J. P. & Barkai, E. Beyond quantum jumps: Blinking nanoscale light emitters. *Physics Today* **62**, 34–39 (2009).
- [197] Bachir, A. I., Kolin, D. L., Heinze, K. G., Hebert, B. & Wiseman, P. W. A guide to accurate measurement of diffusion using fluorescence correlation techniques with blinking quantum dot nanoparticle labels. *J. Chem. Phys.* **128**, 225105 (2008).



# Acknowledgments

I would like to express my gratitude to all those who gave me the possibility to complete this thesis. Especially I would like to thank:

**Christos Likos and Gerhard Kahl** for your constant support and encouragement. I consider myself very lucky to have such outstanding supervisors, and will always look up to you.

**My friends and former colleagues at the Heinrich-Heine-Universität Düsseldorf** Jörg Bewerunge, Sebastian Huissmann, Dominic Lenz, Mark Ludwig, Kathrin Müller, Philipp Naumann, Tim Neuhaus, Armin Sadat-Khonsari and Dana Wagner for all the good times we spent in and outside the university.

**My friends and colleagues at the Vienna University of Technology** Moritz Antlanger, Emanuela Bianchi, Günther Doppelbauer, Giannis Georgiou, Ismene Kolovos, Jan Kurzidim, Martina Lechner, Marta Montes Saralegui, Ulf Rørbæk Pedersen, Dieter Schwanzer and Andreas Tröster for your warm welcome and good company.

**My family** for steadily supporting my studies over the past eight years and making this thesis possible.

**Florence Antony** for your love and care.

This work was supported by the Deutsche Forschungsgemeinschaft (DFG) under the Project No. SFB-TR6 C3, by the Österreichische Forschungsfond (FWF) under Project No. P19890-N16, by the Marie Curie ITN-COMPLOIDS (Grant Agreement No. 234810), and by the Studienstiftung des Deutschen Volkes. Computer time on the Vienna Scientific Cluster (VSC) is gratefully acknowledged.



# Curriculum vitae

## Personal data:

	<b>Arash Nikoubashman</b> Institute for Theoretical Physics Vienna University of Technology Wiedner Hauptstraße 8-10 1040 Vienna, Austria Email: arash.nikoubashman@tuwien.ac.at
Citizenship: German	
Date of Birth: 1985, June the 11 <sup>th</sup>	
Place of Birth: Tehran, Iran	

## Education and university studies:

---

- 09/2010 – present    **PhD studies in Physics** at the *Vienna University of Technology* (Austria) with a thesis on “*Non-Equilibrium Computer Experiments of Soft Matter Systems*”, under the supervision of Prof. Gerhard Kahl
- 10/2009 – 09/2010    **PhD studies in Physics** at the *Heinrich Heine University of Düsseldorf* (Germany) with a thesis on “*Non-Equilibrium Computer Experiments of Soft Matter Systems*”, under the supervision of Prof. Christos N. Likos
- 10/2007 – 02/2010    **B. Sc. in Computer Science**, final mark 1.8 (very good), at the *Heinrich Heine University of Düsseldorf* (Germany) with a thesis on “*Genetic Algorithms for Anisotropic Interaction Potentials*”, under the supervision of Prof. Christos N. Likos
- 10/2007 – 09/2009    **M. Sc. in Physics**, final mark 1.1 (excellent), at the *Heinrich Heine University of Düsseldorf* (Germany) with a thesis on “*Branched Polymers under Shear*”, under the supervision of Prof. Christos N. Likos
- 10/2004 – 09/2007    **B. Sc. in Physics**, final mark 1.5 (excellent), at the *Heinrich Heine University of Düsseldorf* (Germany) with a thesis on “*Computer Simulations of Polymers in Solvents of Varying Quality*”, under the supervision of Prof. Christos N. Likos
- 06/2004                **High School Diploma** (Abitur), final mark 1.5, at *Ernst-Moritz-Arndt-Gymnasium Krefeld* (Germany)

## Work experience:

---

- 03/2010                Lecturer for the course of “*Introduction to Programming in C++*” at the *Heinrich Heine University of Düsseldorf* (Germany)
- 10/2009 – 05/2010    Teaching assistant for the course of “*Electrodynamics*” at the *Heinrich Heine University of Düsseldorf* (Germany), Prof. Christos N. Likos
- 10/2007 – 08/2009    Teaching assistant for the course of “*Physics for Non-Physicists*” at the *Heinrich Heine University of Düsseldorf* (Germany), Prof. Dieter Schumacher

## Scholarships and awards:

---

- 01/2011 – present    PhD fellowship of the “*Studienstiftung des Deutschen Volkes*”
- 09/2010 – present    PhD fellowship of the Marie Curie-Initial Training Network “*Physics of Complex Colloids: Equilibrium and Driven (ITN-COMPLOIDS)*”
- 10/2009 – 09/2010    PhD fellowship of the “*Interdisciplinary Graduate and Research Academy Düsseldorf*”
- 06/2006 – 09/2009    Undergraduate fellowship of the “*Studienstiftung des Deutschen Volkes*”